

UC Berkeley

UC Berkeley Electronic Theses and Dissertations

Title

Anisotropic Turbulence and Protostellar Feedback in Molecular Clouds

Permalink

<https://escholarship.org/uc/item/69j9z9rg>

Author

Hansen, Charles Edward

Publication Date

2011

Peer reviewed|Thesis/dissertation

Anisotropic Turbulence and Protostellar Feedback in Molecular Clouds

by

Charles Edward Hansen

A dissertation submitted in partial satisfaction of the
requirements for the degree of
Doctor of Philosophy

in

Astrophysics

in the

Graduate Division
of the
University of California, Berkeley

Committee in charge:
Professor Christopher McKee, Chair
Professor Richard Klein
Professor Eliot Quataert
Professor Steven Boggs

Fall 2011

Anisotropic Turbulence and Protostellar Feedback in Molecular Clouds

Copyright 2011
by
Charles Edward Hansen

Abstract

Anisotropic Turbulence and Protostellar Feedback in Molecular Clouds

by

Charles Edward Hansen

Doctor of Philosophy in Astrophysics

University of California, Berkeley

Professor Christopher McKee, Chair

I investigate the decay and regeneration of turbulence in molecular clouds and the resulting star formation in those clouds in the presence of protostellar feedback. Studies of turbulence generally only consider isotropic turbulence, while the turbulence in molecular clouds may be anisotropic. I perform a series of simulations of anisotropic turbulence and measure its decay rate. I find that anisotropic turbulence decays slower than isotropic turbulence. When I break the velocity dispersion into isotropic and anisotropic components, I find the decay time is the crossing time of the isotropic component, which can be much slower than the total velocity dispersion. As part of this study, I present a measure of anisotropy that can be calculated in observations of molecular clouds. I also investigate the effects of compression on turbulence. This is motivated by the need to replenish turbulent energy. Using a series of simulations of contracting turbulence, I find that turbulence behaves as a monatomic ideal gas under isotropic compression. I also find that compression in a single direction imparts energy to that direction, but does not transfer that energy to the other two directions.

Finally, I perform a series of high resolution star formation simulations with adaptive mesh refinement (AMR) including hydrodynamics, gravity, radiation, protostellar outflows and protostellar luminosity. The simulations provide a self-consistent story of star formation, all while matching observations. The matched observations include the masses of both stars and prestellar cores, the clustering of cores and the luminosity function of protostars. In this story of star formation, cores form on the Jeans length of the host cloud. Each core forms a central star or binary, but also fragments repeatedly down $0.05 M_{\odot}$ stars. The stellar radiation prevents fragmentation below this mass scale, but is not important on larger scales. The protostellar outflows eject $2/3$ of the incoming mass, leaving $1/3$ of the core mass for stars.

To my wife and to my parents

Contents

List of Figures	iv
List of Tables	viii
Acknowledgments	ix
1 Introduction	1
2 Anisotropy Lengthens the Decay Time of Turbulence in Molecular Clouds	4
2.1 Introduction	4
2.2 Anisotropic Turbulence	7
2.3 Simulations	8
2.4 Results	9
2.5 Observed Anisotropies	15
2.6 Conclusions	22
3 Turbulence Under Compression	23
3.1 Introduction	23
3.2 Turbulence Equation of State	25
3.2.1 Averaging	25
3.2.2 Derivation	25
3.3 Numerical Methods	28
3.4 Results	30
3.4.1 Isotropic Compression	30
3.4.2 Anisotropic Compression	30
3.5 Conclusions	35
4 Feedback Effects on Low Mass Star Formation	36
4.1 Introduction	37
4.2 Simulations	39
4.2.1 Initial Conditions	39
4.2.2 Evolution Equations	40
4.3 Results	43

4.3.1	Large Scale Evolution	43
4.3.2	Evolution of the Protostellar Population	47
4.3.3	Thermal Evolution	52
4.4	Discussion	54
4.4.1	Supporting a Cloud with Outflows	54
4.4.2	Comparison to the IMF	59
4.4.3	Comparison to Protostellar Luminosities	60
4.4.4	Preventing Fragmentation with Radiative Feedback	61
4.4.5	Fragmentation in Rho Ophiuchus	64
4.4.6	Observed Core Mass Functions	66
4.4.7	CMF to IMF relation	68
4.4.8	Turbulent Core and Competitive Accretion	71
4.4.9	The Role of Stellar Mergers	72
4.5	Conclusions	73
	Bibliography	76

List of Figures

2.1	The evolution of kinetic energy over time for quasi-isotropic (left panel) and anisotropic (right panel) simulations of decaying turbulence. The kinetic energy is normalized by the kinetic energy at time zero. The quasi-isotropic simulations all demonstrate the same general behavior. Anisotropic simulations each decay at their own pace, though always slower than the quasi-isotropic simulations. The anisotropic simulations have initial $\sigma_{\text{iso}}/\sigma$ values of 0.25, 0.40, 0.50 and 0.55 from top (slower decay) to bottom (faster decay)	11
2.2	The evolution of relative anisotropic velocity dispersion, relative isotropic velocity dispersion, and decay coefficient for a simulation in which $\sigma_{\text{ani}}/\sigma_v$ was initially 0.93. This is a highly anisotropic case. The left plot shows the evolution over decay time and the right plot shows evolution over total velocity dispersion. Note the ratio of the anisotropic component of the velocity dispersion to the isotropic component is relatively constant until the mach number drops below 3. At this point, pressure forces can convert anisotropic kinetic energy into isotropic energy.	13
2.3	Compensated power spectra for σ_1 and σ_3 for strongly anisotropic turbulence after it has been allowed to decay to Mach 6. The normalization of the power is different for the different velocities, but the slopes are the same.	14
2.4	Decay coefficient vs isotropy, data from all simulations binned together. Horizontal error bars represent bin width and vertical error bars represent uncertainty of the mean of data within the bin. There is more data at the highest anisotropy, which reduces the error bars compared to the higher isotropy points. The simulations divide into anisotropic and quasi-isotropic, with the dividing line at $\sigma_{\text{iso}}/\sigma_v = 0.7$. For the anisotropic simulations, the decay coefficient is proportional to $\sigma_{\text{iso}}/\sigma_v$. For quasi-isotropic simulations, the decay coefficient is constant.	16
2.5	Ratio of solenoidal to compressive velocities squared versus velocity dispersion isotropy. The ratio remains near the isotropic value of 2 for quasi-isotropic simulations, but starts to increase when $\sigma_{\text{iso}}/\sigma_v < 0.7$	17
2.6	Decay Rate and Anisotropy for the same anisotropic driving pattern at different resolutions. The anisotropy is constant across resolutions, but the decay rate is not converged at 256^3 until one crossing time.	18

2.7	Second PCA eigenimages for strong, intermediate, and weak anisotropy from left to right. The turbulent energy and driving scale in all three simulations are the same. The x and y axes are position in the plane of the sky and cover the entire width of the simulation. The units of the image are column density, the actual values of which are not significant.	19
2.8	δv_x and δv_y vs ξ for strong, intermediate, and weak anisotropy from left to right. The blue triangles represent the direction with the largest velocity dispersion in the plane of the sky and the green circles represent the perpendicular direction. In each case, the direction is chosen to maximize the difference between δv_x and δv_y	20
2.9	Observed anisotropy, ψ vs σ_3/σ and $\sigma_3/\sigma_{\text{los}}$ for a variety of simulations, in three different lines of sight for each simulation. The piecewise linear fit to the data in the right panel is plotted as the solid line.	21
3.1	Specific turbulent energy vs mean density for rapidly compressed turbulence. The solid line represents the simulation data and the dashed line represents $\rho\sigma^2 \propto \rho^{5/3}$	31
3.2	Turbulent velocity dispersion vs time for turbulence compressed with a compression time similar to the decay time	32
3.3	Specific turbulent energy vs mean density for turbulence rapidly compressed in the x direction. The solid line is the x energy, and the points represent the energy in the other two directions. The dashed line is $\rho\sigma_x^2 = \rho^3$ [need to run this longer]	33
3.4	Turbulent velocity dispersion vs time for turbulence mildly compressed in the x direction. The solid line is the x energy, and the points represent the energy in the other two directions.	34
4.1	Column density of the entire simulation domain for BW (left) and B (right) at times 0, 0.2, 0.4, 0.6, 0.8 and 1.0 t_{ff} from top to bottom. Star particles are marked with white circles. There is very little difference on the domain scale with and without winds for the barotropic simulations.	44
4.2	Column density (left) and density weighted Temperature (right) for simulation R at times 0, 0.2, 0.4, 0.6, and 0.8 t_{ff} from top to bottom. Particles are marked with white circles.	45
4.3	Same as Figure 4.2, but for simulation RW. The high temperature regions are the paths of outflows. It only takes a small amount of gas at 10^4 K to move the average temperature above 30 K through that line of sight.	46
4.4	Time evolution of global rms Mach number for simulations with and without winds and with and without radiation. The turbulent energy in all simulations decays for half a global free fall time, at which point gravitational potential energy from stars is converted into kinetic energy, which raises the rms velocity. When winds are included, they contribute over twice as much energy as gravity itself. .	48

4.5	Total momentum that has been injected by wind over time for the barotropic simulations. For comparison, the total mass of the simulation multiplied by the velocity dispersion is also plotted. The total wind momentum integrates all injected momentum over time, even from winds that have decayed. This way the amount of injected momentum is eventually higher than the actual momentum of the cloud.	49
4.6	Total mass in stars as a function of time for the four main simulations. The mass of the entire simulation domain is $180 M_{\odot}$	50
4.7	Number of stars as a function of time for the four main simulations. In the barotropic case, the number of stars is unaffected by winds. In the radiative case, radiation suppresses the number of stars unless wind is present.	51
4.8	Median mass of stars as a function of time for the four main simulations. The two cases with winds maintain low medians throughout the simulations. The case with radiation without winds (case R) is able to suppress fragmentation and star formation largely stops as the original stars accrete mass.	52
4.9	Total stellar luminosity versus time for simulations with radiation both with and without winds. Winds dramatically lower the radiation.	53
4.10	Mean and median stellar luminosity versus time for simulations with radiation. The top panel is the simulation without winds and the bottom panel is the simulation with winds.	54
4.11	Total gas mass heated above 12 K versus time, compared to the background value of 10 K. The total mass in stars is also plotted for reference.	55
4.12	Phase plot showing total gas mass as a function of temperature (y-axis) and density (x-axis) for radiative simulations with (left) and without (right) winds. Phase plots are taken at times of 0.25, 0.5 and 0.75 t_{ff} from top to bottom. The high-temperature low-density gas on the left part of the wind phase plots is outflow gas. Warm, high-density gas is near gas near a luminous star.	56
4.13	Ratio of solenoidal to compressive energy versus time with and without winds for the radiative simulations. For pure hydrodynamic, isotropic turbulence, this ratio should be around 2. This ratio stays near 2 when winds are excluded. When winds are included, the turbulence is much more anisotropic, leading to higher solenoidal fractions.	57
4.14	Time evolution of rms Mach number of dense gas and all gas with and without winds. Winds significantly raise the Mach number of the light gas, but do not strongly influence the dense gas turbulence.	58
4.15	The mass function of all stars in each simulation are shown in blue histograms. The mass function of the first 30 stars to form are overplotted in red hatched histograms. The stellar IMF is plotted as the green line. Top left: RW at $t = 0.83t_{\text{ff}}$. Top right: R at $t = 0.83t_{\text{ff}}$. Bottom left: BW at $t = 1.09t_{\text{ff}}$. Bottom right: B at $t = 1.03t_{\text{ff}}$	59

4.16	Mass function for all stars with mass $> 0.05M_{\odot}$ for simulations RW (top) and BW (bottom) with the Chabrier IMF also plotted. The two mass functions are similar. The main difference comes from the largest star in RW fragmenting more in BW, lowering the largest mass and adding more stars around $0.5M_{\odot}$	63
4.17	Two point correlation function, w , for clumps in simulation RW convolved with a 1600 AU Gaussian beam. The correlation function is calculated at an early time, $t \sim 0.4t_{\text{ff}}$ and a late time, $t \sim 0.75t_{\text{ff}}$. The correlation is similar at early and late times, except for the smallest scales, where fragmentation increases over time. For comparison, the fit to $r < 3 \times 10^4$ AU measurements from ρ Ophiuchus is also included.	65
4.18	Median mass of the CMF found in a cloud as a function of resolution of the observation. The CMFs from synthetic observations of RW are green triangles. For comparison, CMFs tabulated in Reid & Wilson (2006) are included as well as 3 CMFs from Enoch et al. (2008). The two lowest points from Reid & Wilson (2006) are ρ Ophiuchus at different wavelengths.	67
4.19	Mass functions for both the initial cores found using clumpfind and the final masses in stars. The y axis represents total counts and is not normalized. Top panel: cores found using a 1600 AU beam size. Bottom panel: cores found using an 800 AU beam size.	68
4.20	Histogram of masses of bound childless sub-cores at $t = 0.4t_{\text{ff}}$	70

List of Tables

4.1	Table of simulations	39
4.2	Accretion rate dependencies on instantaneous and final protostellar mass . .	61
4.3	Turbulent Core Properties. The last two cores eventually merge with the largest core, making it impossible to measure the final gas and total stellar properties. The final properties of the largest core are necessarily a sum over the last two cores in addition to the largest core.	71

Acknowledgments

This dissertation has been produced through collaboration with Christopher McKee, Richard Klein, Philip Chang and Robert Fisher. The work in this manuscript also benefited from helpful discussions with Stella Offner, Andrew Cunningham, Mark Krumholz, Andrew Myers, Pak Shing Li, and anonymous referees. I would like to thank my fellow students in the UC astronomy department for countless helpful discussions and general moral support.

Funding for my work was provided by Lawrence Livermore National Laboratory under the auspices of the UC Department of Energy and the National Science Foundation. Computing time was provided by the San Diego Supercomputer Center, the National Energy Research Scientific Computer Center, the Texas Advanced Computing Center, the National Center for Supercomputing Applications, the National Institute for Computational Science, and NASA Advanced Supercomputing.

Chapter 1

Introduction

Stars are the basic building block of the universe. A complete theory of star formation is essential to the understanding of everything in astrophysics from the formation of the Earth to the formation and evolution of entire galaxies. Forming such a theory is one of the most challenging goals of astrophysics. The difficulty lies in the extremely large dynamic range of star formation and the multitude of physical processes involved. Star formation begins in giant molecular clouds (GMCs) on scales of 100 pc and continues down to the radius of the sun, which is over 1 billion times smaller. The fundamental physical processes governing this transition to smaller sizes are gravity and turbulence. Radiation, magnetic fields, thermodynamics, and molecular chemistry also play important roles in forming each star.

Star formation in our galaxy takes place in molecular clouds ranging from a few pc to 100 pc with observed masses of up to a few $10^6 M_{\odot}$ (Williams & McKee 1997). These molecular clouds are being pulled inwards by their own gravity, but pushed outwards by supersonic turbulence (McKee & Ostriker 2007). These two effects nearly cancel each other out, leaving only a few percent of cloud gas able to form stars in a dynamical time (Krumholz & Tan 2007). The rate of this formation depends sensitively on the nature of the supersonic turbulence, but many aspects of turbulence in molecular clouds are poorly understood.

One of the more important questions in turbulence is how long it lives. Observations show that turbulence is ubiquitous in molecular clouds (Larson 1981; Solomon et al. 1987). Molecular clouds themselves are thought to live for 20-30 million years (Blitz & Shu 1980; Williams & McKee 1997; Blitz et al. 2007; Kawamura et al. 2009), suggesting turbulence should live for at least that long. Simulations of turbulence, however, show that it should decay in under ~ 10 million years (Mac Low et al. 1998; Stone et al. 1998). If these decay rates are correct, turbulence needs to be regenerated somehow. There are many candidates for this, including protostellar outflows (Li & Nakamura 2006; Banerjee et al. 2007; Nakamura & Li 2007; Wang et al. 2010), ionization from high-mass stars (Matzner 2002; Krumholz & Matzner 2009), supernovae (Mac Low & Klessen 2004), and external accretion (Klessen & Hennebelle 2010; Goldbaum et al. 2011). None of these mechanisms can work in all clouds, leaving the overall picture of turbulence regeneration quite complicated.

When turbulence does allow parts of the molecular cloud to collapse, that gas will accumulate behind shocks and gather mass into prestellar cores. Once those cores reach enough mass, they become gravitationally unstable and collapse into one or more protostars (Shu 1977; McKee & Tan 2003). Gas from the cores will fall onto an accretion disk around each protostar that will funnel the gas inwards. Magnetic fields in these accretion disks will become twisted and power bipolar outflows. These outflows will eject or entrain over half of the incoming mass (Matzner & McKee 2000). This means that typical observed cores will be more massive than typical observed stars (Alves et al. 2007; Enoch et al. 2008).

The mass of the cores, and therefore the stars, should naively be set by the densities and temperatures of the host molecular clouds. However, observations show that stars have a universal mass function over a range of cloud Jeans masses (Kroupa 2002; Chabrier 2003; Bastian et al. 2010). This suggests that something must set a universal mass scale. Possibilities include dust self-opacity (Low & Lynden-Bell 1976), gas-dust coupling (Larson 2005; Elmegreen et al. 2008), and protostellar radiation (Offner et al. 2009b; Krumholz et al. 2011).

These effects are all very complicated and require powerful simulations (Klein et al. 2007). These simulations must both incorporate a variety of physical effects and simulate a wide dynamic range. Traditional fixed-grid codes have been developed for almost any set of physics one would care to simulate, but they suffer from poor dynamic range and cannot model the collapse of clouds into cores or cores into stars. Particle methods such as smoothed-particle hydrodynamics (SPH) are great for capturing collapse, but are inaccurate in simulating shocks and instabilities, which are essential for turbulence and for star formation (Agertz et al. 2007). My method of choice is adaptive mesh refinement (AMR), which can simulate shocks like a fixed-grid code, but can refine grids around areas of collapse, like a particle code (Truelove et al. 1998; Klein 1999).

In this dissertation, I investigate the means of maintaining turbulence in star forming clouds and then the effects of protostellar feedback on star formation. This is done with a series of simulations and detailed analysis of these simulations, including comparisons to observations and analytic theories.

Turbulence simulations generally only consider isotropic turbulence, while molecular clouds themselves have clear anisotropies. In Chapter 2, I use the ORION code to simulate anisotropic turbulence and measure its decay rate. I find that anisotropic turbulence decays slower than isotropic turbulence. When I break the velocity dispersion into isotropic and anisotropic components, I find the decay time is the crossing time of the isotropic component, which can be much slower than the total velocity dispersion. I also present a measure of anisotropy that can be calculated in observations of molecular clouds. This chapter represents a paper published in *The Astrophysical Journal*.

In Chapter 3, I investigate the effects of compression on turbulence. This is motivated by the need to replenish turbulent energy. Using a series of simulations in ORION with homologous contraction, I find that turbulence behaves as a monatomic ideal gas under isotropic compression. I also find that compression in a single direction imparts energy to that direction, but does not transfer that energy to the other two directions. This chapter

is an outgrowth of Chapter 2 and is not submitted to any journal.

In Chapter 4, I perform a series of high resolution star formation simulations with ORION AMR including hydrodynamics, gravity, radiation, protostellar outflows and protostellar luminosity. The simulations provide a self-consistent story of star formation, all while matching observations. The matched observations include the IMF, the mass function of observed cores, the clustering of cores and the luminosity function of protostars. In this story of star formation, cores form on the Jeans length of the host cloud. Each core forms a central star or binary, but also fragments repeatedly down $0.05 M_{\odot}$ stars. The stellar radiation prevents fragmentation below this mass scale, but is not important on larger scales. The protostellar outflows eject $2/3$ of the incoming mass, leaving $1/3$ of the core mass for stars. This chapter represents a paper in preparation to be submitted to The Astrophysical Journal.

Chapter 2

Anisotropy Lengthens the Decay Time of Turbulence in Molecular Clouds

Abstract

The decay of isothermal turbulence with velocity anisotropy is investigated using computational simulations and synthetic observations. We decompose the turbulence into isotropic and anisotropic components with total velocity dispersions σ_{iso} and σ_{ani} , respectively. We find the decay rate of the turbulence depends on the crossing time of only the isotropic component. A cloud of size L with significant anisotropy in its turbulence has a dissipation time, $t_{\text{diss}} = L/(2\sigma_{\text{iso}})$. This translates into turbulent energy decay rates on the cloud scale that can be much lower for anisotropic turbulence than for isotropic turbulence. To help future observations determine whether observed molecular clouds have the level of anisotropy required to maintain the observed level of turbulence over their lifetimes, we performed principal component analysis on our simulated clouds. Even with projection effects washing out the anisotropic signal, there is a measurable difference in axis-constrained principal component analysis performed in directions parallel and perpendicular to the direction of maximum velocity dispersion. When this relative difference, ψ , is 0.1, there is enough anisotropy for the dissipation time to triple the expected isotropic value. We provide a fit for converting ψ into an estimate for the dissipation time, t_{diss} .

2.1 Introduction

Observations show that supersonic velocity dispersions are ubiquitous in molecular clouds (Larson 1981; Solomon et al. 1987). These velocity dispersions are commonly believed to be supersonic turbulence (Elmegreen & Scalo 2004). Supersonic turbulence is an

important determinant in the density and velocity statistics of molecular clouds. The probability distribution function of the density in particular is essential for analytical models of star formation (Padoan & Nordlund 2002; Krumholz & McKee 2005; Hennebelle & Chabrier 2008, 2009; Krumholz et al. 2009). As important as turbulence is for star formation, there are few observational constraints on the evolution of turbulence over time. The difficulty in estimating ages of clouds combined with the small cloud-to-cloud variation of measurable turbulence statistics (Heyer & Brunt 2004) make it hard to construct an evolutionary sequence of turbulence. In principle, one could measure the decay rate of a cloud by measuring the luminosity of dissipation structures, but the uncertainties are too high due to energy sources other than turbulent decay. Another approach is to measure abundances of molecules that are theoretically formed in turbulent dissipation structures due to reliance on endothermic reactions. The dissipation rate should influence the amount of high temperature gas available in the dissipation structures and that should in turn influence the rate of the endothermic reactions. Attempts to explain the observed abundances of such molecules (Falgarone et al. 1995, 2006; Godard et al. 2009) find they are dependent on many parameters and cannot be used to extract a dissipation rate. Given the lack of observable constraints on turbulent evolution, we must rely on theoretical arguments.

In the standard theory for isotropic incompressible turbulence (Kolmogorov 1941), energy from the largest scales cascades into smaller scales in a self-similar fashion until the energy reaches a viscous scale and dissipates. In this scenario, turbulence should decay at a rate

$$\frac{1}{2} \frac{d\sigma_v^2}{dt} = -\epsilon \frac{\sigma_v^3}{L}, \quad (2.1)$$

where ϵ is a dimensionless constant, L is the injection scale of the turbulent energy and σ_v^2 is the mass-weighted mean-square velocity,

$$\sigma_v^2 \equiv \frac{\langle \rho v^2 \rangle}{\langle \rho \rangle}. \quad (2.2)$$

Brackets indicate spatial averages, ρ is the mass density and v is the fluid velocity. Numerical simulations of incompressible hydrodynamic turbulence find $\epsilon = 0.6$ (Kaneda et al. 2003). Compressible turbulence can also dissipate energy in radiative shocks, but the overall dissipation rate remains approximately unchanged. Numerical simulations (Mac Low et al. 1998; Stone et al. 1998; Mac Low 1999; Ostriker et al. 1999; Padoan & Nordlund 1999; Lemaster & Stone 2009) have found $\epsilon = 0.6 - 0.8$. Turbulence in these simulations decays in a single crossing time. Alternatively, note that the Kolmogorov energy scaling relation from incompressible turbulence can be recreated in the compressive regime by replacing instances of v with $\rho^{1/3}v$ (Lighthill 1955; Fleck 1996; Kritsuk et al. 2007). This suggests an alternate decay equation, $\frac{1}{2}d/dt\langle\rho v^2\rangle = -\epsilon_{\text{alt}}\langle\rho v^3\rangle/L$, where ϵ_{alt} is a dimensionless constant similar to ϵ , but not identical. For comparison with past studies, we shall use ϵ and not ϵ_{alt} .

The short timescale decaying turbulence is a problem when compared to cloud lifetimes, which are thought to be 20-30 Myr (Blitz & Shu 1980; Williams & McKee 1997; Blitz et al. 2007; Kawamura et al. 2009) while the typical crossing time of these clouds is ~ 10 Myr.

Opposing theories hold that molecular clouds are transient objects formed in converging flows of atomic gas and only live for a single dynamical time (Ballesteros-Paredes et al. 1999; Vázquez-Semadeni et al. 2007; Banerjee et al. 2009; Vázquez-Semadeni et al. 2010). Theories that rely on short-lived clouds can explain the turbulence observed in molecular clouds, but they significantly over-predict the star-formation rate. If the turbulence dissipates in a crossing time and the molecular cloud can collapse into stars, clouds will convert 100% of their mass into stars in a free fall time, as opposed to the observed rates of a few percent. If clouds do live for several dynamical times, either something is replenishing the lost turbulent energy or some mechanism prevents the decay in the first place by storing energy in a slowly decaying mode. Recent investigations have concentrated on replenishing the energy through stellar feedback such as protostellar outflows (Li & Nakamura 2006; Banerjee et al. 2007; Nakamura & Li 2007; Wang et al. 2010), HII regions (Matzner 2002; Krumholz & Matzner 2009), or supernovae (Mac Low & Klessen 2004). Driving turbulence primarily with stellar feedback is difficult because clouds with high star formation rates, such as the Rosette Nebula, and clouds with extremely low star formation rates, such as Maddalena’s cloud, have indistinguishable turbulent properties (Heyer et al. 2006). In addition, most internal driving sources deposit their energy on scales less than the cloud size, while observations find the driving scale must be at least as large as the molecular clouds themselves (Ossenkopf & Mac Low 2002; Brunt et al. 2009). The most promising driving mechanism to date is external accretion. Many molecular clouds accrete gas from their HI envelopes (Fukui et al. 2009). Gas in the envelope has a higher specific energy than the cloud itself and can transmit that energy into the cloud upon accretion. How much energy can be transferred this way is uncertain, but specific transfer rates should be able to reproduce both the observed turbulence and the observed star formation rates (Klessen & Hennebelle 2010; Vázquez-Semadeni et al. 2010; Goldbaum et al. 2011). For clouds without enough accretion power, there is no clear mechanism for driving turbulence while also reproducing the observations.

The alternative to driving turbulence is storing turbulent energy in a slowly decaying mode. Arons & Max (1975) postulated that magnetic fields could prolong turbulence by storing energy in long-lived Alfvén waves. Numerical simulations of MHD turbulence (Mac Low et al. 1998; Stone et al. 1998; Mac Low 1999; Ostriker et al. 1999; Padoan & Nordlund 1999) however, found that magnetic fields did not significantly change the decay rate as the Alfvén waves coupled with quickly decaying modes.

Here we demonstrate that large scale anisotropy in the turbulent velocity field leads to slow decay and thus may be an alternative to steadily driven turbulence. Our simulations do not include magnetic fields and so are only a proof of principle. Detailed observations show large velocity gradients on the scale of the clouds (Brunt et al. 2009; Kirk et al. 2010). These gradients indicate a preferred axis for the turbulence on large scales. Previous isotropic simulations cannot address this effect. Small scale anisotropy is predicted in the presence of strong magnetic fields from an imbalanced cascade (Maron & Goldreich 2001; Cho et al. 2002), and may be an explanation for the inferred velocity anisotropy in Taurus below 0.4 pc (Heyer et al. 2008). However, this turbulence does not decay more slowly than isotropic hydrodynamic turbulence in simulations. It explains only anisotropy on scales much less

than the driving scale, not the observed cloud scale velocity gradients. Velocity anisotropy needs to be present on the turbulent injection scale to truly slow down decay.

Given the uncertainty in the source of turbulent energy, it is difficult to predict the anisotropy resulting from turbulent driving. Nevertheless, all methods of driving have inherent anisotropy. In accretion driven turbulence (Klessen & Hennebelle 2010; Goldbaum et al. 2011), the angular distribution of mass in the accretion reservoir should determine the anisotropy. If the accreted gas preferentially comes from one direction, the velocity dispersion will be larger in that direction. In a similar manner, turbulence powered by HII regions will be anisotropic if the driving HII regions are primarily on one side of the cloud. Turbulence powered by colliding flows will naturally have anisotropy in the direction of the collision. This has been measured in Vázquez-Semadeni et al. (2007), where the velocity dispersion in the collision direction is twice the dispersion in other directions at early times. At late times, the effect is reversed and the dispersion in the collision direction is less than half the dispersion in the other directions. Regardless of the driving source, any turbulence with power on the cloud scale should be anisotropic. Only a handful of turbulent modes can fit in the cloud on the cloud scale, so one direction should dominate due to cloud-to-cloud variance (the interstellar analog of cosmic variance).

We introduce a framework for decay of anisotropic turbulence in §2. In §3, we describe our simulations. We quantify the relationship between anisotropy and decay rate in §4. In §5 we introduce a method for measuring anisotropy in molecular clouds, and we summarize our conclusions in §6.

2.2 Anisotropic Turbulence

The isotropic model of turbulence in equation (2.1) is a function only of length and a single rms velocity, but a turbulent cloud could have up to three independent rms velocities. Three rotationally invariant velocities can be derived from the Reynold's stress tensor, τ ,

$$\tau_{ij} = \langle \rho v_i v_j \rangle. \quad (2.3)$$

Because τ is real and symmetric, there exists a cartesian coordinate system where it is diagonal

$$\tau = \begin{pmatrix} \langle \rho v_i^2 \rangle & 0 & 0 \\ 0 & \langle \rho v_j^2 \rangle & 0 \\ 0 & 0 & \langle \rho v_k^2 \rangle \end{pmatrix}. \quad (2.4)$$

The eigenvalues, λ_i , of τ therefore represent twice the non-thermal kinetic energy along the three axes of this diagonalizing coordinate system. If the cloud is isotropic, the off-diagonal terms will be zero in any cartesian coordinate system and the eigenvalues are all equal to two thirds of the total kinetic energy. Even if the three cardinal directions in a simulation have equal energies, anisotropy can be present. Any correlation between velocities in the cardinal directions will create anisotropy, which will be detected with the off-diagonal

terms in τ . Velocity dispersion, σ_i can be recovered from λ_i by

$$\sigma_i = \sqrt{\lambda_i / \langle \rho \rangle}. \quad (2.5)$$

As a convention, the velocities can always be ordered such that $\sigma_1 \geq \sigma_2 \geq \sigma_3$.

With three velocities, clouds now have three specific energies, $\frac{1}{2}\sigma_i^2$, and three time scales, L/σ_i . Even if we assume no coupling between the time scales, equation (2.1) expands into three equations

$$\frac{1}{2} \frac{d\sigma_1^2}{dt} = -C_{11} \frac{\sigma_1^3}{L} - C_{12} \frac{\sigma_1^2 \sigma_2}{L} - C_{13} \frac{\sigma_1^2 \sigma_3}{L}, \quad (2.6)$$

$$\frac{1}{2} \frac{d\sigma_2^2}{dt} = -C_{21} \frac{\sigma_2^2 \sigma_1}{L} - C_{22} \frac{\sigma_2^3}{L} - C_{23} \frac{\sigma_2^2 \sigma_3}{L}, \quad (2.7)$$

$$\frac{1}{2} \frac{d\sigma_3^2}{dt} = -C_{31} \frac{\sigma_3^2 \sigma_1}{L} - C_{32} \frac{\sigma_3^2 \sigma_2}{L} - C_{33} \frac{\sigma_3^3}{L}, \quad (2.8)$$

where the elements of matrix \mathbf{C} are non dimensional constants similar to ϵ . The set of three equations can be rewritten as

$$\frac{1}{2} \frac{d \ln \sigma_i^2}{dt} = -\frac{C_{ij} \sigma_j}{L}, \quad (2.9)$$

where repeated indices imply summation.

The goal of this paper is to determine whether the presence of anisotropy can decrease turbulent decay in molecular clouds. This is primarily accomplished by measuring the elements of \mathbf{C} for the full range of anisotropy.

2.3 Simulations

To determine the effect of anisotropy on the turbulent decay rate, we performed a series of simulations. We perform these simulations using the parallel adaptive mesh refinement code, ORION, in fixed grid mode. While ORION possesses adaptive refinement abilities, simulating turbulence requires refining most of the simulation domain. In this situation, fixed grid simulations are more computationally efficient than adaptive grids. ORION utilizes a conservative second order Godunov scheme to solve the equations of compressible gas dynamics (Truelove et al. 1998; Klein 1999),

$$\frac{\partial \rho}{\partial t} + \nabla \cdot (\rho \mathbf{v}) = 0, \quad (2.10)$$

$$\frac{\partial \rho \mathbf{v}}{\partial t} + \nabla \cdot (\rho \mathbf{v} \mathbf{v}) = -\nabla P, \quad (2.11)$$

where ρ , P , and \mathbf{v} are the fluid density, pressure, and velocity respectively. In these simulations, the gas is isothermal and the sound speed is a constant, as this is a good approximation in molecular clouds. The boundary conditions are periodic in all variables.

Simulations start with a constant density and are perturbed with a constant solenoidal driving pattern similar to that described in Mac Low (1999). These perturbations correspond to a Gaussian random field with a Burgers power spectrum, $P(k) \propto k^{-2}$ (Frisch & Bec 2001), over some range of driving wavenumbers, k_d , which can vary from simulation to simulation. Most simulations use driving wavelengths $k_d = 1 - 2$ to produce the largest possible inertial range. Simulations at $k_d = 2 - 3$ and $k_d = 3 - 4$ were also used to determine the effect of varying the driving range. When the density field is no longer smooth, the center-of-mass velocity of the driving pattern will not be zero and will vary in time. To avoid accumulation of net momentum in the simulation, we subtract the center-of-mass velocity from the driving pattern at each time step before the driving occurs. Each simulation is driven for two crossing times at Mach 10 and then allowed to decay to Mach 3. Only the data during this decay phase are used for analysis. The initial Mach number needs to be high so that decaying turbulence remains supersonic. Mach 10 was chosen because higher Mach number simulations did not show a converged dissipation rate at our resolution of 256^3 . We performed 21 of these simulations.

The anisotropy was controlled in two ways, by changing the relative amplitudes of the driving pattern in different directions or by changing the wavenumber of the driving pattern. When creating a driving pattern, there are two independent fields, one for each velocity direction minus a constraint from a requirement for the turbulence to be solenoidal. For the anisotropic patterns, the amplitude of each field is chosen randomly from a Gaussian distribution. To achieve simulations that are nearly isotropic, the amplitudes are set to be identical. It is physically impossible to obtain complete isotropy with this method, as any correlations between the independent fields will enhance the velocity dispersion in one direction and suppress it in another. The wavenumber of the driving pattern was also used in setting anisotropy. The most anisotropic simulations were produced using driving patterns with power at $k_d = 1 - 2$ with slope k^{-2} . These include simulations with over 95% of the turbulent power in a single direction. To make more isotropic turbulence, power is moved to smaller scales. This was accomplished by simulations driven at $k_d = 3 - 4$. This had the effective result of averaging over 27 independent $k_d = 1 - 2$ driving patterns, which reduces the relative amount of power any single turbulent mode can contain.

2.4 Results

Turbulent quantities were calculated at intervals of approximately 10% of a crossing time for each simulation where the crossing time is defined as $L / (\sigma_v)$ and is itself a function of time. At each of these intervals the components of the stress tensor τ_{ij} are calculated. The eigenvalues, λ_i , of this tensor are found and the eigenvelocities, σ_i , are calculated from equation (2.5). The total velocity dispersion, σ_v , is also calculated. Given measurements $\sigma_{i,n}$ and $\sigma_{v,n}$ at time t_n and measurements $\sigma_{i,n+1}$ and $\sigma_{v,n+1}$ at time t_{n+1} , there are intermediate

quantities

$$t_{n+\frac{1}{2}} = \frac{1}{2}(t_n + t_{n+1}), \quad (2.12)$$

$$\sigma_{v,n+\frac{1}{2}} = \frac{1}{2}(\sigma_{v,n} + \sigma_{v,n+1}), \quad (2.13)$$

$$\sigma_{i,n+\frac{1}{2}} = \frac{1}{2}(\sigma_{i,n} + \sigma_{i,n+1}), \quad (2.14)$$

$$\epsilon_{n+\frac{1}{2}} = \frac{(\sigma_{v,n} - \sigma_{v,n+1})L}{(t_{n+1} - t_n)\sigma_{v,n+\frac{1}{2}}^2}. \quad (2.15)$$

The decay coefficient ϵ is a function of time differences of measured quantities and is best defined at the half time interval. The intervals themselves are close enough together that $\sigma_{v,n}$ and $\sigma_{v,n+\frac{1}{2}}$ differ by typically 1% to 5%, depending on the decay rate. The half-interval choice does not affect the results in any significant way.

We also introduce two new velocity dispersions useful for analysis

$$\sigma_{\text{iso}} \equiv \sqrt{3}\sigma_3, \quad (2.16)$$

$$\sigma_{\text{ani}} \equiv \sqrt{\sigma_v^2 - \sigma_{\text{iso}}^2}. \quad (2.17)$$

The two velocities represent a cloud with a perfectly isotropic velocity distribution with 3D dispersion σ_{iso} and an additional perfectly anisotropic velocity distribution σ_{ani} that is absent in at least one direction.¹ When normalized by the total 3D turbulent velocity dispersion, $\sigma_{\text{iso}}/\sigma_v$ and $\sigma_{\text{ani}}/\sigma_v$ both can range from 0 to 1. Simulations can be divided into two classes based on these ratios. Turbulence with $\sigma_{\text{iso}}/\sigma_v < 0.7$ will be called anisotropic and turbulence with $\sigma_{\text{iso}}/\sigma_v > 0.7$ will be called quasi-isotropic. The middle velocity dispersion, σ_2 , is not used above, but it is well correlated with and approximately equal to σ_3 . Averaging over the most anisotropic simulations, the median value of σ_2/σ_3 is 1.6. For comparison, the median value of σ_1/σ_2 is those simulations is 5. The median of the ratio σ_2/σ_3 is 1.2 over the quasi-isotropic simulations.

We note that most of the power is on the largest scales, which is a characteristic of both the turbulence in our simulations and the turbulence in Nature. As a consequence, a significant fraction of the energy can be in apparently coherent motions, such as large scale velocity gradients as observed in Perseus (Kirk et al. 2010). In the absence of periodic boundary conditions, the motions can take the form of overall expansion or contraction; just such behavior in molecular clouds has been observed by Brunt et al. (2009). Another consequence of the power being concentrated on the largest scales is that the power in the range of driving wavelengths dominates the total in our simulations (and quite possibly in

¹There are many velocity dispersions in this paper and it may be helpful to summarize them all in one place. The total 3D velocity dispersion is σ_v . It can be represented as the sum of two 3D velocity dispersions σ_{iso} and σ_{ani} . The eigenvalues of the Reynold's stress tensor go into the 1D velocity dispersions σ_1 , σ_2 , and σ_3 with $\sigma_1 \geq \sigma_2 \geq \sigma_3$. The 1D version of σ_v is σ ($\sigma \equiv \sigma_v/\sqrt{3}$). Similarly, the 1D version of σ_{iso} is σ_3 .

molecular clouds as well). The values of the velocity dispersions σ that we analyze here are therefore determined to a significant extent by the power at these wavelengths. Anisotropic hydrodynamic turbulence in the interstellar medium requires anisotropic driving.

The evolution of kinetic energy for a sample of quasi-isotropic and anisotropic simulations is shown in Figure 2.1. The quasi-isotropic simulations all decay faster than the anisotropic simulations. Each anisotropic simulation has a unique decay rate while the quasi-isotropic simulations all follow the same path. The evolution of ϵ , $\sigma_{\text{iso}}/\sigma_v$ and $\sigma_{\text{ani}}/\sigma_v$ for

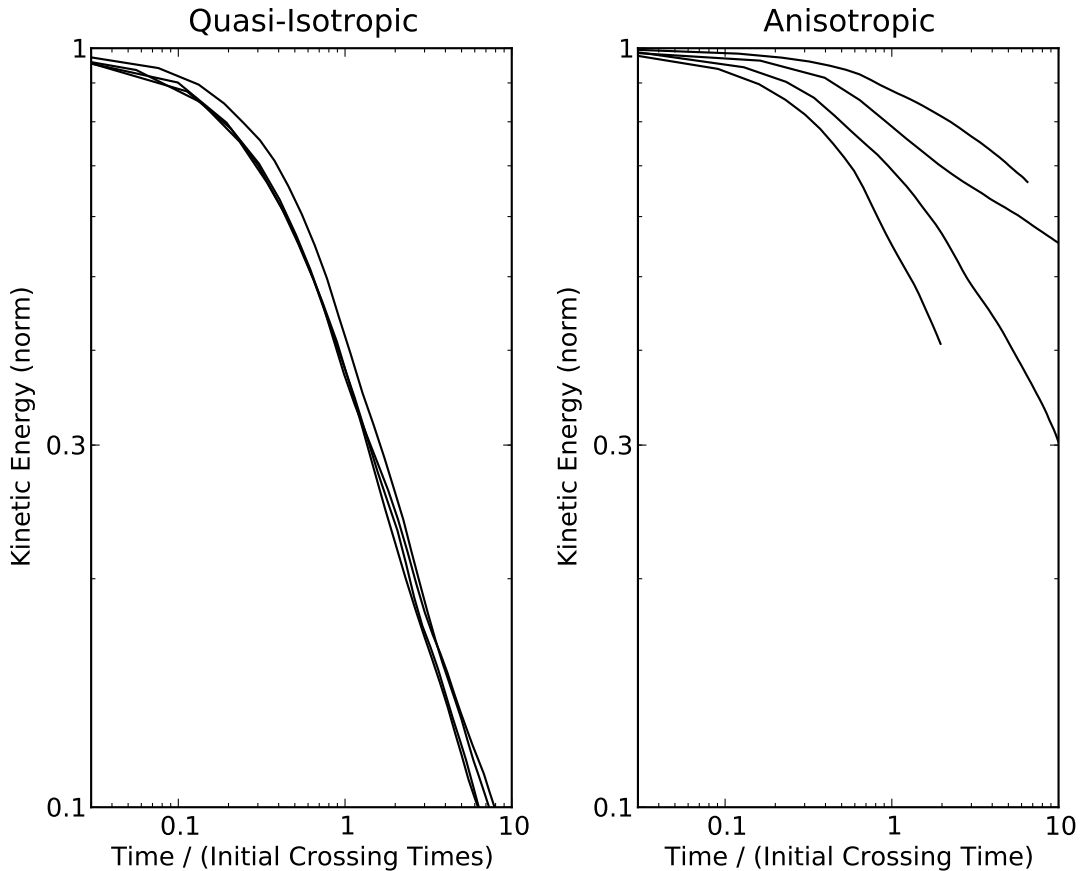


Figure 2.1 The evolution of kinetic energy over time for quasi-isotropic (left panel) and anisotropic (right panel) simulations of decaying turbulence. The kinetic energy is normalized by the kinetic energy at time zero. The quasi-isotropic simulations all demonstrate the same general behavior. Anisotropic simulations each decay at their own pace, though always slower than the quasi-isotropic simulations. The anisotropic simulations have initial $\sigma_{\text{iso}}/\sigma$ values of 0.25, 0.40, 0.50 and 0.55 from top (slower decay) to bottom (faster decay)

a typical strongly anisotropic run are shown in Figure 2.2. Right after driving is turned off, the decay rate fluctuates for half a crossing time for every simulation. After that point,

the decay rate is relatively stable with occasional fluctuations, such as the one that occurs at 3 crossing times in Figure 2.2. This behavior lasts until the total velocity dispersion is about sonic, at which point pressure forces become important. Thermal pressure effectively transmits energy dissipated from a single direction into all three directions. This increases the isotropy of the turbulence and also increases ϵ . The analysis is cut off before this point, but the simulation is allowed to continue in Figure 2.2 to show the effect. In the supersonic regime, isotropy can increase or decrease, depending on the particular realization of the turbulence. In Figure 2.2, the isotropy slowly decreases, and then slowly increases, until it rapidly increases in the sonic regime.

Given that anisotropy decreases for subsonic velocity dispersions, it is possible that anisotropy is a function of scale even for supersonic turbulence. In this situation, anisotropy would be strongest at the driving wavelength, and would slowly decrease until the turbulence is isotropic around the sonic scale. When we compare power spectra for σ_1 and σ_3 , however, anisotropy is equally strong at all scales in the inertial range (the anisotropy does decrease moving from from the driving range to the inertial range). A typical anisotropic power spectrum is shown in Figure 2.3. When the 3D velocity dispersion is supersonic, both σ_1 and σ_3 follow a featureless Burgers power spectrum for the inertial range. The inertial range typically ends at $k \sim 25$, which is well before the sonic scale at $k \sim 100$, when the turbulence should eventually shift to a Kolmogorov power spectrum.

To calculate the coefficients in equation (2.9), we calculate σ_i and $d\sigma_i/dt$ at each point in time, which also yields an ϵ and $\sigma_{\text{iso}}/\sigma_v$. The binned results of these measurements are shown in Figure 2.4. There appears to be a qualitative change in the decay rate above $\sigma_{\text{iso}}/\sigma = 0.7$. For the purposes of fitting equation (2.9), we ignore all points above this cutoff. We then perform a linear regression for each velocity component with the left hand side of equation (2.9) as the dependent variables and σ_i as independent variables.

We find that the three elements C_{i1} are best fit by zero, with error bars of 0.1. This means that the largest velocity, σ_1 , does not contribute to turbulent decay. We find that the elements C_{i2} are also best fit by zero, but with much larger error bars, 0.5. The last three elements, C_{i3} are 1.7, also with error bars around 0.5. The velocity dispersions σ_2 and σ_3 are well correlated with each other, which adds uncertainty into fits of C_{i2} or C_{i3} separately. The summed coefficients $C_{i2} + C_{i3}$ are 1.7 ± 0.3 . For future analysis, we will stick with the best fit coefficients, $C_{i2} = 0$ and $C_{i3} = 1.7$. The final matrix is then in equation (2.18):

$$\mathbf{C} = \begin{pmatrix} 0 \pm 0.1 & 0 \pm 0.5 & 1.7 \mp 0.5 \\ 0 \pm 0.1 & 0 \pm 0.5 & 1.7 \mp 0.5 \\ 0 \pm 0.1 & 0 \pm 0.5 & 1.7 \mp 0.5 \end{pmatrix}. \quad (2.18)$$

Because the errors in C_{i2} and C_{i3} are negatively correlated, they are marked with \pm and \mp respectively.

Putting these coefficients into equations (2.6) to (2.8) yields

$$\frac{1}{2} \frac{d\sigma_1^2}{dt} = -\sigma_1^2 \frac{1.7\sigma_3}{L} = -\sigma_1^2 \frac{\sigma_{\text{iso}}}{L}, \quad (2.19)$$

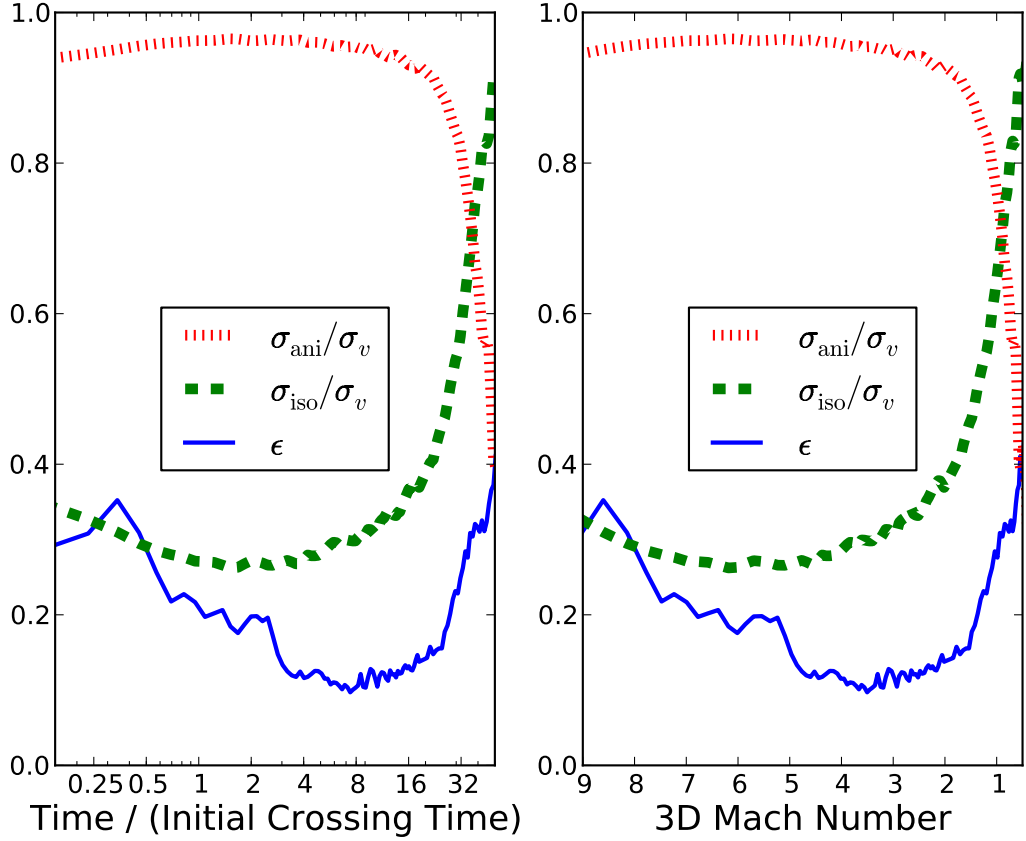


Figure 2.2 The evolution of relative anisotropic velocity dispersion, relative isotropic velocity dispersion, and decay coefficient for a simulation in which $\sigma_{\text{ani}}/\sigma_v$ was initially 0.93. This is a highly anisotropic case. The left plot shows the evolution over decay time and the right plot shows evolution over total velocity dispersion. Note the ratio of the anisotropic component of the velocity dispersion to the isotropic component is relatively constant until the mach number drops below 3. At this point, pressure forces can convert anisotropic kinetic energy into isotropic energy.

$$\frac{1}{2} \frac{d\sigma_2^2}{dt} = -\sigma_2^2 \frac{1.7\sigma_3}{L} = -\sigma_2^2 \frac{\sigma_{\text{iso}}}{L}, \quad (2.20)$$

$$\frac{1}{2} \frac{d\sigma_3^2}{dt} = -\sigma_3^2 \frac{1.7\sigma_3}{L} = -\sigma_3^2 \frac{\sigma_{\text{iso}}}{L}. \quad (2.21)$$

Note that the fact that the coefficients in the rightmost equations are unity is a result of our simulations and not an assumption.

With the decay rates of the individual energy components, we can construct a total

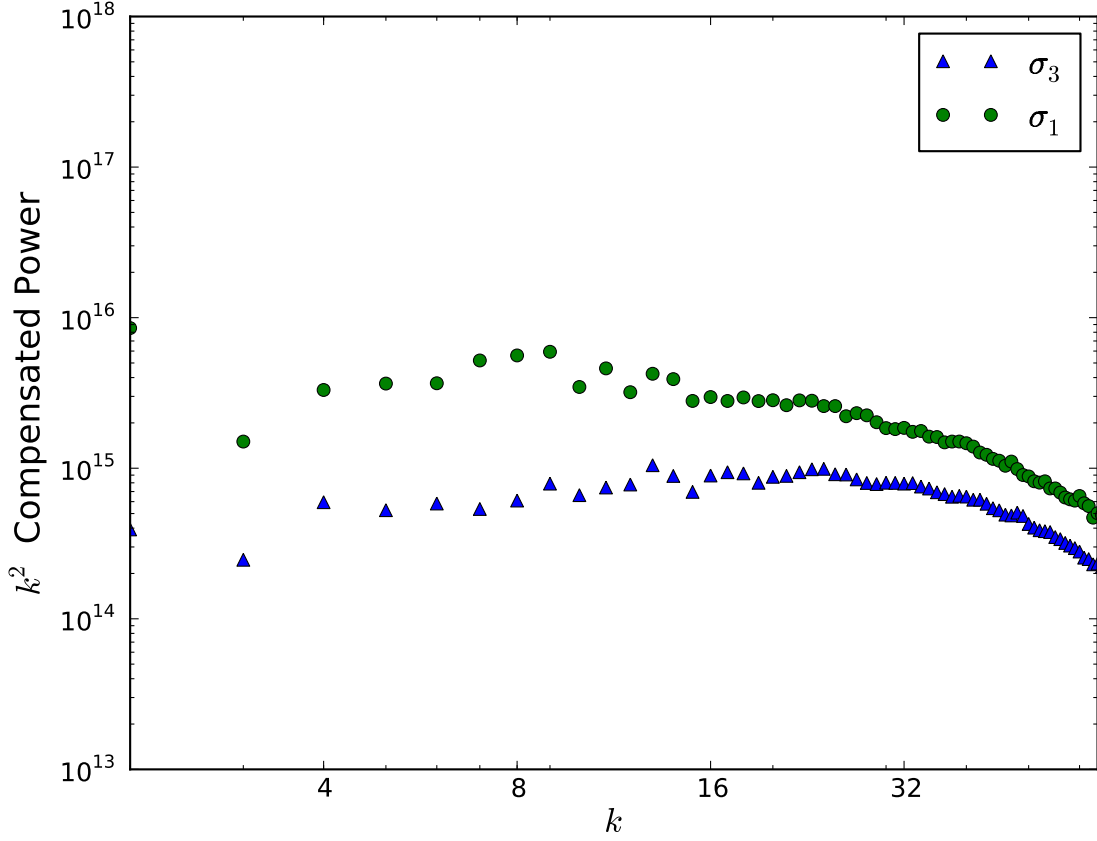


Figure 2.3 Compensated power spectra for σ_1 and σ_3 for strongly anisotropic turbulence after it has been allowed to decay to Mach 6. The normalization of the power is different for the different velocities, but the slopes are the same.

energy decay rate

$$\frac{1}{2} \frac{d\sigma_v^2}{dt} = -\frac{\sigma_v^2 \sigma_{\text{iso}}}{L}. \quad (2.22)$$

To look more like equation (2.1), we use the dimensionless decay coefficient ϵ such that

$$\sigma_v \frac{d\sigma_v}{dt} = -\epsilon \frac{\sigma_v^3}{L}, \quad (2.23)$$

$$\epsilon \equiv -\frac{L}{\sigma_v^2} \frac{d\sigma_v}{dt} = \frac{\sigma_{\text{iso}}}{\sigma_v}. \quad (2.24)$$

This entire derivation of ϵ has been performed while ignoring the quasi-isotropic clouds, which have $\sigma_{\text{iso}}/\sigma_v > 0.7$. These clouds show a relatively constant $\epsilon \sim 0.7$, which agrees with

$\epsilon = 0.6 - 0.8$ from prior isotropic studies. For the full range of $\sigma_{\text{iso}}/\sigma_v$, ϵ is described by the equation

$$\epsilon = \begin{cases} (1.0 \pm 0.2)\sigma_{\text{iso}}/\sigma_v & \text{if } \sigma_{\text{iso}}/\sigma_v \leq 0.7 \\ 0.7 \pm 0.05 & \text{if } \sigma_{\text{iso}}/\sigma_v > 0.7 \end{cases}. \quad (2.25)$$

A cloud with specific kinetic energy, $E = \frac{1}{2}\sigma_v^2$ has a dissipation time t_{diss} ,

$$t_{\text{diss}} \equiv \frac{E}{dE/dt} = \frac{L}{2\epsilon\sigma_v}. \quad (2.26)$$

In the anisotropic case,

$$t_{\text{diss}} = \frac{L}{2\sigma_{\text{iso}}} \quad \left(\frac{\sigma_{\text{iso}}}{\sigma_v} < 0.7 \right). \quad (2.27)$$

The simulated variation of ϵ versus isotropy is shown in Figure 2.4. Note that while quasi-isotropic simulations agree with $\epsilon = 0.6 - 0.8$ from prior studies, ϵ is always lower for anisotropic simulations and even approaches zero for completely anisotropic simulations.

For turbulence with solenoidal driving like ours, the expected ratio of solenoidal energy to compressive energy in isotropic supersonic turbulence is 2 to 1 (Elmegreen & Scalo 2004). This ratio can be less than one for compressive forcing (Federrath et al. 2008, 2010) and up to 10 when magnetic fields are included (Boldyrev et al. 2002; Porter et al. 2002; Vestuto et al. 2003). To investigate the effect of anisotropy on this ratio, we calculate the similar ratio $\langle |\nabla \times v|^2 \rangle / \langle (\nabla \cdot v)^2 \rangle$. This ratio as a function of anisotropy is shown in Figure 2.5. For quasi-isotropic simulations, the ratio stays at 2 during the supersonic regime. The ratio starts to increase in the anisotropic simulations.

To check the effect of resolution on these results, one of the anisotropic simulations has been repeated at 512^3 , shown in Figure 2.6. The decay rate is not converged at a resolution of 256^3 until 1 crossing time has passed. The turbulence at this point is Mach 9. Removing all data points above Mach 9 does not change any results, particularly those shown in Figure 2.4. The anisotropy is already converged to a level below the natural fluctuations even at 128^3 resolution. The general results of decay rate as a function of anisotropy appear converged by 256^3 resolution.

2.5 Observed Anisotropies

Now that we have a relationship between turbulent decay rate and velocity anisotropy, we would like to know the range of anisotropy in molecular clouds. To compare simulations to observations, we created optically thin synthetic observations from the simulations and performed a principal component analysis (PCA) from Heyer & Schloerb (1997) and Brunt & Heyer (2002). The analysis calculates velocity eigenvectors and eigenimages and can be useful in filtering out high frequency noise often present in turbulent data. The first velocity eigenvector is roughly a gaussian in velocity space, centered at the center-of-mass velocity of the cloud, v_{cm} . The second velocity eigenvector is similar to a derivative of the first velocity

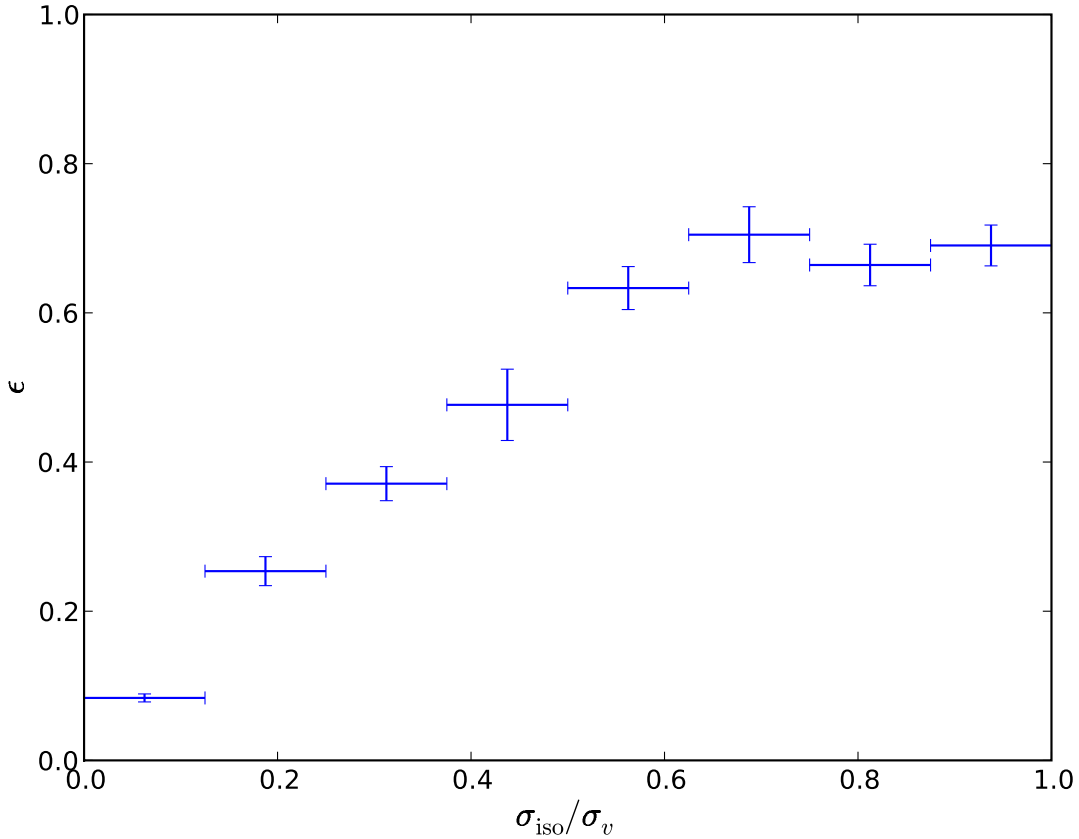


Figure 2.4 Decay coefficient vs isotropy, data from all simulations binned together. Horizontal error bars represent bin width and vertical error bars represent uncertainty of the mean of data within the bin. There is more data at the highest anisotropy, which reduces the error bars compared to the higher isotropy points. The simulations divide into anisotropic and quasi-isotropic, with the dividing line at $\sigma_{\text{iso}}/\sigma_v = 0.7$. For the anisotropic simulations, the decay coefficient is proportional to $\sigma_{\text{iso}}/\sigma_v$. For quasi-isotropic simulations, the decay coefficient is constant.

eigenvector. This produces a positive gaussian below v_{cm} and a negative gaussian above it. Each subsequent velocity eigenvector is like a derivative of the previous one. At each position in the position-position-velocity observation data, one can convolve the data in velocity space with a velocity eigenvector. This produces an eigenimage. The first eigenimage represents the signal from gas at velocities near v_{cm} and is roughly proportional to the signal from the entire cloud. The second eigenimage, which contains both a negative and a positive spike in its eigenvector, shows the signal from gas at velocities greater than v_{cm} subtracted from the signal of gas at velocities less than v_{cm} . The second eigenimage usually has the strongest

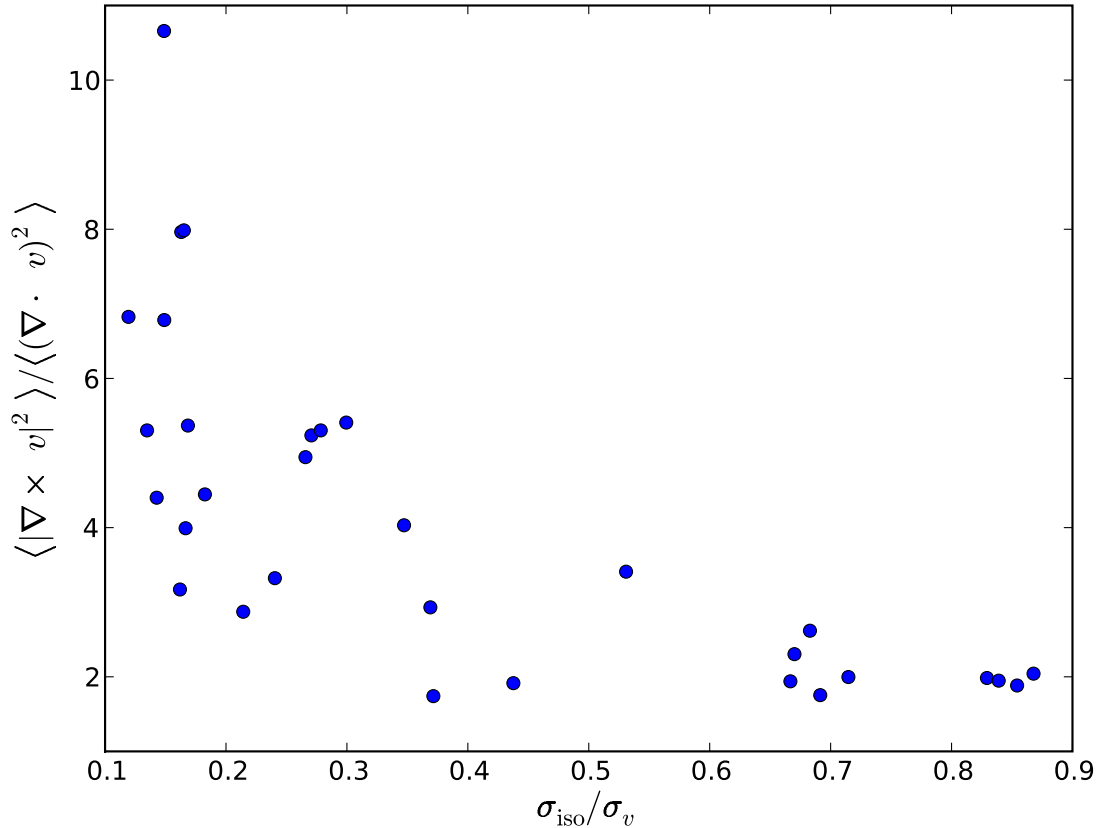


Figure 2.5 Ratio of solenoidal to compressive velocities squared versus velocity dispersion isotropy. The ratio remains near the isotropic value of 2 for quasi-isotropic simulations, but starts to increase when $\sigma_{\text{iso}}/\sigma_v < 0.7$.

signal and is similar to the first velocity moment of column density. The second eigenimages are shown in Figure 2.7 for simulations with $\sigma_{\text{iso}}/\sigma_v$ values of 0.2, 0.5, and 0.8, to represent strong, intermediate and weak anisotropy. All simulations were driven with power in the range $k = 1 - 2$ and have Mach 10 turbulent velocity dispersion. The strong anisotropy case shows a coherent gradient in velocity, which breaks up as the anisotropy becomes weaker. Given the velocity gradients observed with PCA in molecular clouds (Heyer et al. 2006; Brunt et al. 2009), even the intermediate anisotropy case might be too isotropic to match real clouds.

Anisotropic velocity dispersions by themselves do not guarantee the gradients in line-of-sight velocity required to create the left two panels of Figure 2.7. Only the solenoidal component of the turbulent velocity field contains the local velocity shear that can combine into a large scale gradient. As a counter example, a cloud with a large scale expansion or

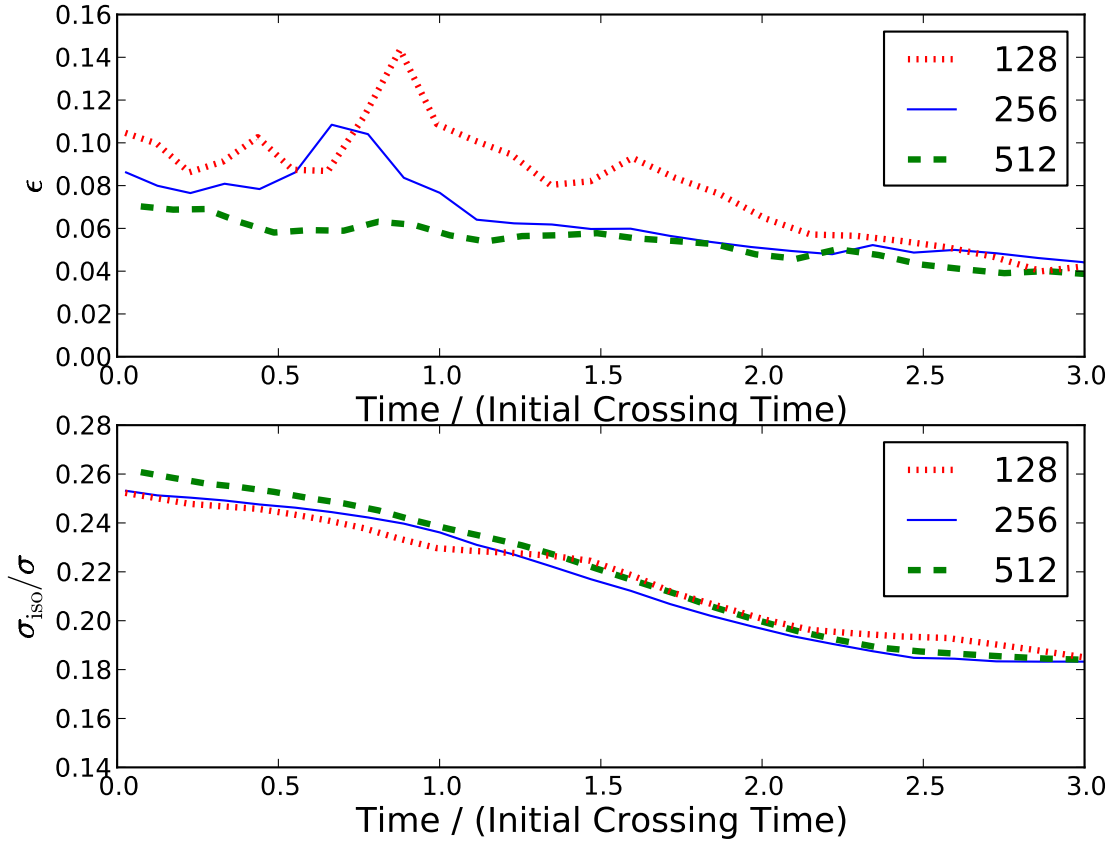


Figure 2.6 Decay Rate and Anisotropy for the same anisotropic driving pattern at different resolutions. The anisotropy is constant across resolutions, but the decay rate is not converged at 256^3 until one crossing time.

contraction mode in one direction would also have anisotropic velocity dispersions, but the turbulence would be mostly compressive and there would be no observed velocity gradient. As demonstrated in Figure 2.5, the turbulence in our anisotropic simulations is mostly solenoidal.

To quantify the coherency of the gradient in Figure 2.7, we perform the axis-constrained PCA from Heyer et al. (2008). This analysis involves performing PCA on many thin strips of data oriented both parallel and perpendicular to some reference direction. The parallel slices return eigenvectors with velocity scale δv_x and eigenimages with length scale ξ_x (note that δv_x is the line of sight velocity in a strip along the x direction, not the x component of the velocity). The perpendicular slices return analogous quantities δv_y and ξ_y . If the data is isotropic, a plot of δv_x versus ξ_x will be identical to δv_y versus ξ_y . If not, the difference between the two plots can show the anisotropy. The reference angle is then rotated until

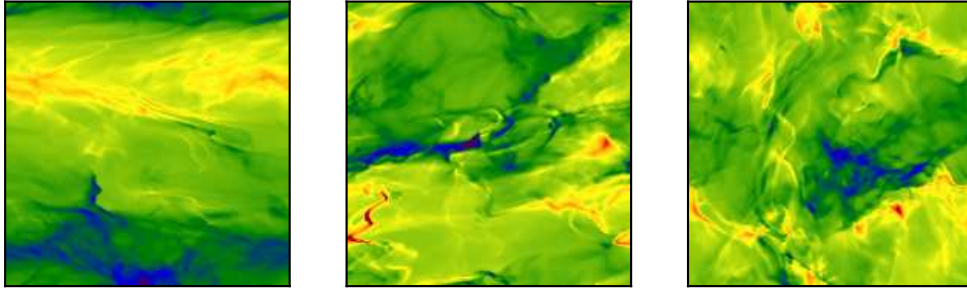


Figure 2.7 Second PCA eigenimages for strong, intermediate, and weak anisotropy from left to right. The turbulent energy and driving scale in all three simulations are the same. The x and y axes are position in the plane of the sky and cover the entire width of the simulation. The units of the image are column density, the actual values of which are not significant.

a maximum difference is found; this angle is perpendicular to the direction of strongest velocity dispersion in the plane of the sky. In Heyer et al. (2008), it was perpendicular to the magnetic field. The length scale ξ in this paper is the same as τ in Heyer et al. (2008), but is changed to prevent confusion with the Reynold's stress tensor, τ . Plots of δv versus ξ are shown in Figure 2.8 for the same simulations shown in Figure 2.7.

In the axis-constrained PCA plots, the anisotropy is strongest on large scales, closest to the energy injection scale. The anisotropy is introduced through energy injection while the energy cascade maintains the injected anisotropy. This is different from Heyer et al. (2008), where the driving is isotropic and the anisotropy is introduced from the energy cascade in a strong magnetic field. In the Heyer et al. (2008) study, the axis-constrained PCA plots show the largest difference at small scales. In principle, a cloud with both anisotropic energy injection and an anisotropic energy cascade will show differences on both large and small scales.

To quantify the anisotropy information from plots such as Figure 2.8, we define an integrated anisotropy.

$$\psi \equiv \int \frac{(|\delta v_x - \delta v_y|)}{(\delta v_x + \delta v_y)} d \ln \xi. \quad (2.28)$$

For our simulations, the lower limit of the integral is twice our resolution and the upper limit is half the driving scale. In an observed cloud, the driving scale should be replaced by the cloud size and the simulation resolution should be replaced by either the telescope resolution or possibly the local Jeans length of the cloud. The goal of ψ is to represent an average relative difference between δv_x and δv_y . In principle, it could reach as high as 1.0, but it ranges between 0.01 and 0.2 in our simulations. For the fit to Taurus from Heyer et al. (2008), $\psi = .11$ when the limits of integration are 5 and 30 pixels. The advantage of ψ is

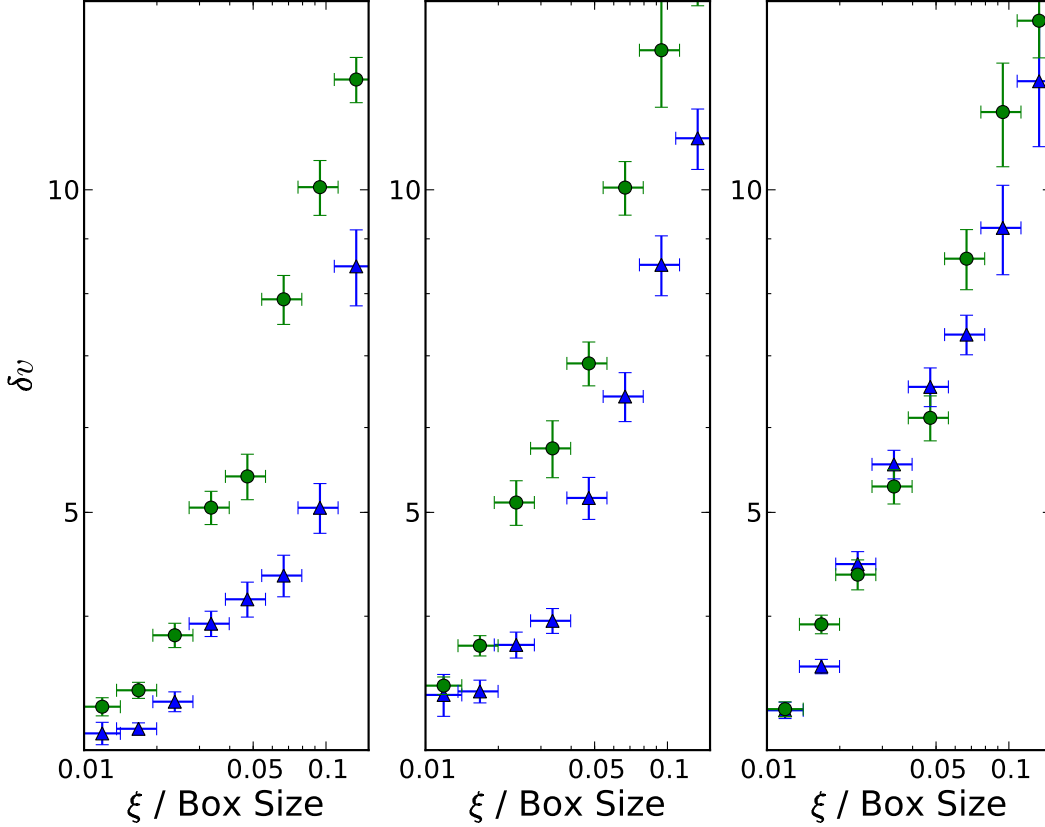


Figure 2.8 δv_x and δv_y vs ξ for strong, intermediate, and weak anisotropy from left to right. The blue triangles represent the direction with the largest velocity dispersion in the plane of the sky and the green circles represent the perpendicular direction. In each case, the direction is chosen to maximize the difference between δv_x and δv_y .

that now we have a single number to represent the anisotropy of a single observation of a cloud.

To quantify the dependence of ψ on anisotropy in our simulations, each simulation is ‘observed’ at an early time (Mach ~ 9) from all three cardinal directions. This produces 3 different values of ψ and 3 different line of sight velocity dispersions, σ_{los} , per simulation. We measured ψ at later times for 3 of the simulations and found that ψ does not depend on Mach number, but can fluctuate by up to 20% over time. Because we are now dealing with observed velocities, it is useful to use the one dimensional velocity dispersion, $\sigma \equiv \sigma_v/\sqrt{3}$. When using σ , the isotropy is measured by σ_3/σ , with

$$\frac{\sigma_3}{\sigma} \equiv \frac{\sigma_{\text{iso}}}{\sigma_v}, \quad (2.29)$$

because σ_3 and σ are equal to $\sigma_{\text{iso}}/\sqrt{3}$ and $\sigma_v/\sqrt{3}$, respectively. Figure 2.9 shows ψ compared to σ_3/σ and $\sigma_3/\sigma_{\text{los}}$ for all measurements of ψ . The plot of ψ vs σ_3/σ shows a general negative

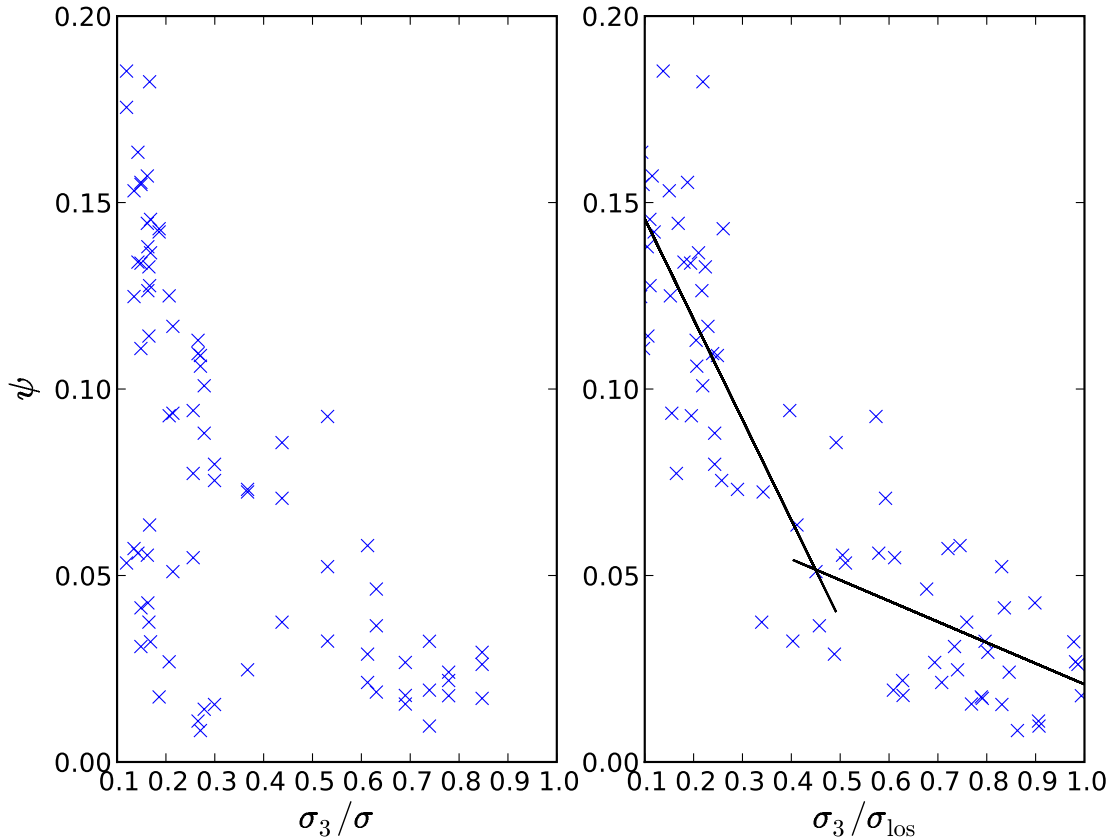


Figure 2.9 Observed anisotropy, ψ vs σ_3/σ and $\sigma_3/\sigma_{\text{los}}$ for a variety of simulations, in three different lines of sight for each simulation. The piecewise linear fit to the data in the right panel is plotted as the solid line.

correlation between, but it contains data where both quantities are near zero. Both high ψ and low σ_3/σ indicate high anisotropy, which causes the negative correlation. The anisotropy is measurable only when it is pointed towards the observer. It is therefore possible for high anisotropy turbulence (low σ_3/σ) to produce a quasi-isotropic signature (low ψ) when the anisotropy is in the plane of the sky. A quasi-isotropic simulation (high σ_3/σ) can never produce a strong anisotropy signature (high ψ). When the anisotropy is in the plane of the sky, $\sigma_{\text{los}}/\sigma$ will be suppressed, leading to a tighter correlation between ψ and $\sigma_3/\sigma_{\text{los}}$ than that between ψ and σ_3/σ . The relation between ψ and $\sigma_3/\sigma_{\text{los}}$ can be expressed in a

piecewise linear fashion (see Figure 2.9)

$$\psi = \begin{cases} (0.17 \pm 0.03) - 0.27 \sigma_3/\sigma_{\text{los}} & \text{if } \sigma_3/\sigma_{\text{los}} \leq 0.45 \\ (0.08 \pm 0.02) - 0.06 \sigma_3/\sigma_{\text{los}} & \text{if } \sigma_3/\sigma_{\text{los}} > 0.45 \end{cases} . \quad (2.30)$$

Given the two observable quantities, ψ and σ_{los} , one can estimate σ_3 , and therefore σ_{iso} , using equation (2.30). If the cloud is anisotropic ($\psi > 0.04$), this can then be used to calculate the dissipation time with the additional observable, L .

$$t_{\text{diss}} = \frac{(0.08 \pm 0.03)L}{(0.17 - \psi)\sigma_{\text{los}}}. \quad (2.31)$$

For comparison, if the cloud is quasi-isotropic, $\sigma_{\text{los}} \sim \sigma = \sigma_v/\sqrt{3}$, and $\epsilon = 0.7$, yielding the equation

$$t_{\text{diss}} = \frac{L}{2\epsilon\sigma_v} \sim \frac{0.4L}{\sigma_{\text{los}}}. \quad (2.32)$$

For reference, t_{diss} from equation (2.31) is triple t_{diss} from equation (2.32) when $\psi = 0.1$

2.6 Conclusions

We have performed a series of hydrodynamic decaying, isothermal turbulence simulations with varying levels of anisotropy. When we break the turbulence into isotropic and anisotropic components, turbulence decays in roughly the crossing time of the isotropic component. This translates into a decay coefficient ϵ that is the isotropic velocity dispersion divided by the total velocity dispersion for most clouds and saturating at 0.7 for quasi-isotropic turbulence. The decay time for these clouds is $t_{\text{diss}} = L/(2\sigma_{\text{iso}})$. A molecular cloud whose size and velocity dispersion would normally indicate a lifetime of 10 Myr using $\epsilon = 0.7$ can maintain its turbulence for the full observed lifetime of 30 Myr if the isotropic velocity dispersion is 1/4 of the total dispersion and if our hydrodynamic results remain valid when magnetic fields are included.

To help investigate whether observed molecular clouds have the level of anisotropy required to maintain the observed level of turbulence over their lifetimes, we performed Principal Component Analysis on our simulated clouds. Line-of-sight effects tend to wash out anisotropic signals, but there can be a measurable difference in axis-constrained PCA performed in directions parallel and perpendicular to the direction of maximum velocity dispersion. When this relative difference, ψ , is 0.1, there is enough anisotropy for the dissipation time to triple the expected isotropic value. We provide a fit for converting ψ into an estimate for the dissipation time, t_{diss} . There are not currently publications with axis-constrained PCA performed on molecular clouds outside of Taurus, but additional clouds should be possible with future observations. This work has ignored the effects of magnetic fields on the turbulence. Magnetic fields would have significantly increased the computational cost of this work. In addition, they could significantly complicate matters as the angle between the magnetic field and the anisotropic velocity vector should be important, as well as the Alfvén Mach number. They will be included in future work.

Chapter 3

Turbulence Under Compression

Abstract

In order to determine the behavior of supersonic turbulence under compression, we derive a simple equation of state for turbulent pressure. This equation of state is equivalent to a $\gamma = 5/3$ monatomic gas under isotropic compression. To verify our derivation, we simulate decaying turbulence undergoing homologous contraction and recreate the derived equation of state. As a consequence of this equation of state, the velocity dispersion of turbulence will naturally asymptote to the velocity of its compression. Additionally, we explored the behavior of turbulence under anisotropic compression. Turbulent velocity dispersion σ_i in direction i follows the rule $\sigma_i \propto 1/a_i$, where a_i is the scale factor in direction i . This means that compression in one direction can impart energy into that direction while leaving the other two directions alone. This is verified with simulations. When this happens, the turbulence becomes extremely anisotropic and the decay rate goes to zero as shown in Hansen et al. (2011).

3.1 Introduction

As explained in the previous chapter, the decay rate and driving mechanism of turbulence in molecular clouds is an outstanding problem in star formation. One unexplored method of driving turbulence is compression of a turbulent cloud. Molecular clouds can be compressed by outside forces such as pressure from warm gas, ram pressure from colliding flows or tidal gravity from spiral arms. Molecular clouds may also collapse under their own self-gravity, causing a global compression. Depending on the effective equation of state of supersonic turbulence, compression may add energy to that turbulence.

In the standard theory for isotropic incompressible turbulence (Kolmogorov 1941), energy from the largest scales cascades into smaller scales in a self-similar fashion until the

energy reaches a viscous scale and dissipates. In this scenario, turbulence should decay at a rate

$$\frac{1}{2} \frac{d\sigma_v^2}{dt} = -\epsilon \frac{\sigma_v^3}{L}, \quad (3.1)$$

where ϵ is a dimensionless constant, L is the injection scale of the turbulent energy and σ_v^2 is the mass-weighted mean-square velocity,

$$\sigma_v^2 \equiv \frac{\langle \rho v^2 \rangle}{\langle \rho \rangle}. \quad (3.2)$$

Brackets indicate spatial averages, ρ is the mass density and v is the fluid velocity. Numerical simulations of incompressible hydrodynamic turbulence find $\epsilon = 0.6$ (Kaneda et al. 2003). Compressible turbulence can also dissipate energy in radiative shocks, but the overall dissipation rate remains approximately unchanged. Numerical simulations (Mac Low et al. 1998; Stone et al. 1998; Mac Low 1999; Ostriker et al. 1999; Padoan & Nordlund 1999; Lemaster & Stone 2009) have found $\epsilon = 0.6 - 0.8$.

Equation (3.1) can be rewritten for the specific kinetic energy $2K \equiv \sigma_v^2$

$$\frac{d(2K)}{dt} = -\epsilon \frac{(2K)^{3/2}}{L}. \quad (3.3)$$

This can be integrated to yield

$$K = K_0 \left(1 + \frac{t}{t_d} \right)^{-2}, \quad (3.4)$$

where t_d is the decay time, defined by $t_d \equiv (\sqrt{2}L)/(\epsilon\sqrt{K_0})$ and K_0 is the kinetic energy when $t = 0$.

The equations so far all assume there is no compression. In particular, $\bar{\rho}$, the average density, is constant. If there is a coherent background flow with background velocity field v_b , some energy should be added to the turbulence. If turbulence can be described by an equation of state such that

$$\frac{\partial \ln \bar{\rho} K}{\partial \ln \bar{\rho}} = \gamma, \quad (3.5)$$

where $\bar{\rho}K$ is the turbulent pressure, equation (3.3) can be extended to

$$\frac{dK}{dt} + (\gamma - 1)K \nabla v_b = -\epsilon \frac{K}{t_d} \left(\frac{K}{K_0} \right)^{\frac{1}{2}} \quad (3.6)$$

This equation is generally not integrable because ∇v_b is an arbitrary function of time and γ is unknown.

3.2 Turbulence Equation of State

If Larson's laws are used to derive an equation of state, one predicts a logatrope, $\bar{\rho}K \propto \log \bar{\rho}$, but Vazquez-Semadeni et al. (1998) and McKee & Tan (2003) showed that this does not describe turbulence. Wu et al. (1985) demonstrated with direct numerical simulations that incompressible turbulence responds as a $\gamma = 5/3$ gas. We will now derive the effective γ for supersonic turbulence.

While direct numerical simulation is a powerful and preferred way of studying turbulence, much can be learned from simpler models. In this section, we derive the simplest model for turbulence, i.e., the one-equation model, taking a very simple means by which turbulence energy is dissipated. We will show that compressible turbulence, modeled as a turbulent pressure, can be represented as a gas with an adiabatic index of 5/3. Canuto (1997) has derived a set of equations that describe compressible turbulence up to fourth order. However, these equations are rather cumbersome and their physical interpretation is unclear (for the inexperienced eye). However, his formalism and notation is excellent, so we will choose to follow that. We will also largely follow his derivation.

3.2.1 Averaging

We begin by defining a mean and fluctuating component to the velocity, \mathbf{u} , pressure, P , and density field, ρ :

$$u_i = \bar{u}_i + u'_i, \quad (3.7)$$

$$\rho = \bar{\rho} + \rho', \quad (3.8)$$

$$p = \bar{P} + P', \quad (3.9)$$

where the mean parts of u_i , p , and ρ are defined as

$$\bar{u}_i \equiv \frac{\langle \rho u_i \rangle}{\bar{\rho}}, \quad (3.10)$$

$$\bar{\rho} \equiv \langle \rho \rangle, \quad (3.11)$$

$$\bar{P} \equiv \langle p \rangle. \quad (3.12)$$

Note that \bar{u} is defined as the mass weighted statistical (time) average, while $\bar{\rho}$ and \bar{P} are simply defined as statistical average.

3.2.2 Derivation

We¹ now begin with the continuity equation

$$\frac{d\rho}{dt} + \rho \frac{\partial u_i}{\partial x_i} = 0, \quad (3.13)$$

¹This section until equation 3.29 written by Philip Chang.

where repeated indices indicate summation, and the momentum equation:

$$\frac{d\rho u_i}{dt} + \rho u_i \frac{\partial u_j}{\partial x_j} = -\frac{\partial p}{\partial x_i} + \frac{\partial}{\partial x_j} \left[\rho \nu \left(\frac{\partial u_j}{\partial x_i} + \frac{\partial u_i}{\partial x_j} \right) - \frac{2}{3} \nu \rho \delta_{ij} \frac{\partial u_k}{\partial x_k} \right], \quad (3.14)$$

where ν is the viscosity. We will define the viscous stress tensor:

$$\sigma_{ij} = \nu \rho \left(\frac{\partial u_j}{\partial x_i} + \frac{\partial u_i}{\partial x_j} \right) - \frac{2}{3} \nu \rho \delta_{ij} \frac{\partial u_k}{\partial x_k} \quad (3.15)$$

Averaging ($\langle \rangle$) equation (3.14), we find

$$\frac{\partial}{\partial t} \bar{\rho} \bar{u} + (\bar{\rho} \bar{u}_i \bar{u}_j + \langle \rho u'_i u'_j \rangle)_{,j} = 0, \quad (3.16)$$

where we have presume that there is no large scale pressure gradient ($\bar{P}_{,i} = 0$) and that the mean flow is unaffected by viscosity, $\sigma_{ij,j} = 0$. Combining this with the averaged continuity equation leaves us with a relatively simple equation for the mean flow

$$\bar{\rho} \frac{D\bar{u}_i}{Dt} + \langle \rho u'_i u'_k \rangle_{,k} = 0. \quad (3.17)$$

where $D/Dt = \partial/\partial t + \bar{u}_i \partial/\partial x_i$.

We now multiply equation (3.17) by \bar{u}_j and symmetrize in i and j to get

$$\bar{\rho} \frac{D}{Dt} \bar{u}_i \bar{u}_j = -(\bar{u}_i \tau_{jk,k} + \bar{u}_j \tau_{ik,k}), \quad (3.18)$$

where we have defined $\tau_{ij} = \langle \rho u'_i u'_j \rangle$. Equation (3.18) defines the evolution equation for the large scale Reynolds stress, $t_{ij} = \bar{u}_i \bar{u}_j$.

We now derive the evolution equation for the turbulent (averaged) Reynolds stress, $\tau_{ij} = \langle \rho u'_i u'_j \rangle$. To do this we start with the momentum equation (eq.[3.14]), multiply by u_j , symmetrize in i and j , and average. This gives

$$\frac{\partial}{\partial t} (\bar{\rho} \bar{u}_i \bar{u}_j + \tau_{ij}) + (\bar{\rho} \bar{u}_i \bar{u}_j \bar{u}_k + \tau_{ij} \bar{u}_k + \tau_{ik} \bar{u}_j + \tau_{jk} \bar{u}_i + \tau_{ijk})_{,k} = \langle F'_i u_j \rangle + \langle F'_j u_i \rangle, \quad (3.19)$$

where $\tau_{ijk} = \langle \rho u'_i u'_j u'_k \rangle$ and

$$F'_i = -p'_i + \sigma'_{ij,j}$$

is the perturbed forces due to pressure and viscosity. To derive the above equation, we use the following identities:

$$\langle \rho u_i u_j \rangle = \bar{\rho} \bar{u}_i \bar{u}_j + \tau_{ij} \quad (3.20)$$

$$\langle \rho u_i u_j u_k \rangle = \bar{\rho} \bar{u}_i \bar{u}_j \bar{u}_k + \tau_{ij} \bar{u}_k + \tau_{ik} \bar{u}_j \tau_{jk} \bar{u}_i + \tau_{ijk} \quad (3.21)$$

We apply equation (3.18) to remove the large scale Reynolds stress from equation (3.19), which gives:

$$\frac{d}{dt}\tau_{ij} + \tau_{ij}\bar{u}_{k,k} + \tau_{ik}\bar{u}_{j,k} + \tau_{jk}\bar{u}_{i,k} + \tau_{ijk,k} = \langle F'_i u_j \rangle + \langle F'_j u_i \rangle. \quad (3.22)$$

We now expand the term:

$$\langle F'_i u_j \rangle + \langle F'_j u_i \rangle = -\langle p'_{,i} u'_j \rangle - \langle p'_{,j} u'_i \rangle + \langle \sigma'_{ik,k} u'_j \rangle + \langle \sigma'_{jk,k} u'_i \rangle. \quad (3.23)$$

The first two terms can be rewritten in terms of a trace and a trace-free component:

$$\langle (p'_{,i} u'_j + p'_{,j} u'_i) \rangle = \pi_{ij} + \frac{2}{3}\delta_{ij}\langle (p' u_k)_{,k} - p' u_{k,k} \rangle, \quad (3.24)$$

where

$$\pi_{ij} = \langle (p'_{,i} u'_j + p'_{,j} u'_i) \rangle - \frac{2}{3}\delta_{ij}\langle p'_{,k} u_k \rangle$$

The last two terms of equation (3.23) can be rewritten as

$$\langle (\sigma'_{ik,k} u'_j + \sigma'_{jk,k} u'_i) \rangle = \langle (\sigma'_{ik} u'_j + \sigma'_{jk} u'_i), k \rangle - \epsilon_{ij}, \quad (3.25)$$

where $\epsilon_{ij} = \langle \sigma'_{ik} u'_{j,k} + \sigma'_{jk} u'_{i,k} \rangle$ is identified with the viscous dissipation.

Taking equations (3.23) and (3.25), we reorganize equation (3.22) to read:

$$\frac{d}{dt}\tau_{ij} = -\langle \tau_{ijk} + \frac{2}{3}p' u_k \delta_{ij} - \sigma'_{ik} u'_j - \sigma'_{jk} u'_i \rangle_{,k} - \epsilon_{ij} - \tau_{ij}\bar{u}_{k,k} - (\tau_{ik}\bar{u}_{j,k} + \tau_{jk}\bar{u}_{i,k}) + \frac{2}{3}\langle p' u'_{k,k} \rangle. \quad (3.26)$$

Before we simplify this equation further, we will highlight the relevance of each term. We now take the trace of the above equation to simplify further. Noting that $\tau_{kk} = 2\bar{\rho}K$, where K is the turbulent kinetic energy, we find

$$2\frac{d\bar{\rho}K}{dt} = -\langle \tau_{iik} + 2p' u_k - 2\sigma'_{ik} u'_{i,k} \rangle - 2\epsilon - 2\bar{\rho}K\bar{u}_{k,k} - 2\tau_{ik}\bar{u}_{i,k} + 2\langle p' u'_{k,k} \rangle, \quad (3.27)$$

where the decay rate, $\epsilon = \epsilon_{ii}/2$. Each term in equation (3.27) has a distinctive physical interpretation. The first term on the RHS presents the diffusion of kinetic energy with the first two terms in $\langle \rangle$ being the turbulent viscosity and the last term the molecular viscosity. The second term is the energy dissipation rate of the turbulent kinetic energy. The third term represents the increase of turbulence kinetic energy due to compression. This term arises from the increase in the density. The fourth term is the coupling of turbulent kinetic energy due to the mean (background) flow. Finally, the fifth term is the dissipation due to pressure dilation.

The solution of equation (3.27) demands knowledge of ϵ , which can be prescribed or solved for by the appropriate use of closure relations at the next order. However, equation (3.27) is sufficient to determine the adiabatic index of compressible supersonic turbulence.

Namely, we will assume pure contraction or dilation (zero shear), where $D/3 = u_{1,1} = u_{2,2} = u_{3,3}$. We then find

$$\frac{d\bar{\rho}K}{dt} = -\left\langle \frac{1}{2}\tau_{iik} + p'u_k - \sigma'_{ik}u'_i \right\rangle_{,k} - \epsilon - \frac{5}{3}\bar{\rho}KD, \quad (3.28)$$

where we have dropped the pressure dilation term. The numerical factor of $5/3$ comes a factor of D from the third term and a factor of $2/3$ from the fourth term (recall that $\tau_{ii} = 2K$). This numerical factor of $5/3$ gives the adiabatic index of compressible turbulence. Finally, in the absence of kinetic energy gradients, the first term goes away and we are left with

$$\frac{d\bar{\rho}K}{dt} = -\epsilon - \frac{5}{3}\bar{\rho}KD. \quad (3.29)$$

Thus, the effective γ for turbulent pressure is $5/3$.

When $\gamma = 5/3$ is put in equation (3.1), we get

$$\frac{dK}{dt} + \frac{2}{3}K\nabla v_b = -\epsilon \frac{K}{t_d} \left(\frac{K}{K_0} \right)^{\frac{1}{2}} \quad (3.30)$$

Equation 3.30 is still not integrable unless we assume ∇v_b is a constant. This constant has units $1/\text{time}$ and we will define a compression time, $t_c = 1/\nabla v_b$. This also introduces a new compression velocity, $v_c = L/(2t_c)$, which is the time for a box of length L to reduce to zero volume. Now equation (3.30) can be integrated to

$$K = \left(1 + \frac{t}{t_d} - \frac{t}{t_c} \right)^{-2} \quad (3.31)$$

3.3 Numerical Methods

To validate the applicability of equation 3.1 to supersonic turbulence, we performed a series of direct numerical simulations. Our simulations are performed using the code Orion, which uses a conservative second order Godunov scheme to solve the equations of compressible gas dynamics (Truelove et al. 1998; Klein 1999). The continuity and momentum equations are

$$\frac{d\rho}{dt} + \nabla \cdot (\vec{v}\rho) = 0 \quad (3.32)$$

$$\frac{d\vec{v}}{dt} + (\vec{v} \cdot \nabla)\vec{v} = -\frac{1}{\rho}\nabla p, \quad (3.33)$$

with fluid variables density, ρ , velocity, \vec{v} and pressure p . In order to simulate a cloud undergoing compression, we have moved to a comoving coordinate system. Given a cube of

length L_0 , undergoing contraction such that at any given time it's physical length, L_i in any direction x_i is $L_i = a_i L_0$, one can define a comoving density $\rho_c = \rho / (a_1 a_2 a_3)$. A contracting cube also has a background velocity gradient, \vec{v}_b , defined by $v_{b,i} = x_i da_i / dt$ which can be removed by defining a peculiar velocity, $\vec{v}_p = \vec{v} - \vec{v}_b$.

In the case of isotropic contraction ($a = a_1 = a_2 = a_3$), the (isothermal) fluid equations are

$$\frac{d\rho_c}{dt} + \frac{1}{a} \nabla \cdot (\vec{v}_p \rho_c) = 0 \quad (3.34)$$

$$\frac{d\vec{v}_p}{dt} + \frac{1}{a} (\vec{v}_p \cdot \nabla) \vec{v}_p = -\frac{\dot{a}}{a} \vec{v}_p - \frac{1}{a\rho_c} \nabla p_c \quad (3.35)$$

$$p_c = c_{iso}^2 \rho_c. \quad (3.36)$$

In the more general case where a_1 , a_2 , and a_3 are independent, the first two fluid equations become

$$\frac{d\rho_c}{dt} + \left(\frac{1}{a_i} \frac{d}{dx_i} \right) (v_{p,i} \rho_c) = 0 \quad (3.37)$$

$$\frac{dv_{p,i}}{dt} + \left(\frac{v_{p,j}}{a_j} \frac{d}{dx_j} \right) v_{p,i} = -\frac{\dot{a}_i}{a_i} v_{p,i} - \frac{1}{\rho_c} \left(\frac{1}{a_j} \frac{d}{dx_j} \right) p_c \quad (3.38)$$

where repeated indices imply summation.

Orion was modified to solve the comoving fluid equations by first modifying the Reimann solver, replacing the quantity dx_i with the quantity $a_i dx_i$. This substitution transforms equation 3.32 into equation 3.37 and it transforms equation 3.33 into equation 3.38 without the $-\frac{\dot{a}_i}{a_i} v_{p,i}$ term on the right side of the equation. The missing term is added explicitly, after the hydro equations are solved with the modified Reimann solver. The operator split equation is then

$$\frac{dv_{p,i}}{dt} = -\frac{\dot{a}_i}{a_i} v_{p,i}. \quad (3.39)$$

Simulations start with a constant density and are perturbed with a constant solenoidal driving pattern similar to that described in Mac Low (1999). These perturbations correspond to a Gaussian random field with a Burgers power spectrum, $P(k) \propto k^{-2}$ (Frisch & Bec 2001), over the range of driving wavenumbers, $k_d = 3 - 4$. When the density field is no longer smooth, the center-of-mass velocity of the driving pattern will not be zero and will vary in time. To avoid accumulation of net momentum in the simulation, we subtract the center-of-mass velocity from the driving pattern at each time step before the driving occurs. After two cloud crossing times, the driving is turned off and the compression begins.

3.4 Results

3.4.1 Isotropic Compression

When the compression begins, a particular speed v_c is chosen in each direction such that one end of the simulation is moving at speed $-v_c$ and the other is moving at v_c (the center of mass velocity is zero). This velocity is kept constant throughout a simulation, making the equation $dL_i/dt = -2v_{c,i}$ always true. Due to numerical time step constraints, the turbulent box can never reach zero length in any direction, but it can be evolved to an arbitrarily small value.

The value of the compression speed can be chosen from three regimes, $t_d \gg t_c$, $t_d \ll t_c$ and $t_d \sim t_c$. All three should be explored to validate equation 3.30. We already performed many simulations in with $t_d \ll t_c$ in Hansen et al. (2011). The results of runs with no compression, t_c is infinity, give the expected decay coefficient $\epsilon = 0.7$.

The regime with $t_d \sim 100t_c$ is shown in figure 3.1. At early times, the decay is minimal and $\rho\sigma^2 \propto \rho^{5/3}$. As σ rises, t_d decreases until the decay time is no longer negligible and we approach the regime where $t_d \sim t_c$. This regime is shown more clearly in a simulation with initial values $t_d = 0.5t_c$. The turbulent velocity decays until $t_d = t_c$ which is around $\sigma = v_c$ for our driving range of $k = 3 - 4$. This is shown in figure 3.2.

3.4.2 Anisotropic Compression

To better predict the effects of compression due to anisotropic astrophysical sources such as tides, we would like to understand the behavior of turbulence under anisotropic compression. The isotropic result $\bar{\rho}K \propto \bar{\rho}^{5/3}$ is equivalent to $\sigma \propto 1/a$, where a is the homologous scale factor. In the case of thermal pressure, the equation of state does not distinguish between directions, but turbulent pressure can be broken into three directional components, $\bar{\rho}\sigma_i^2$. The anisotropic equation of state for turbulent pressure is described by $\sigma_i \propto 1/a_i$. If compression occurs in the x direction, but not y or z , $\bar{\rho}\sigma_x^2 \propto \bar{\rho}^3$ while $\bar{\rho}\sigma_y^2$ and $\bar{\rho}\sigma_z^2$ are independent of $\bar{\rho}$.

To test this, we repeated the simulations while compressing in only one direction. For simplicity, we will always refer to that direction as the x direction. The compression in the x direction is the same as in the isotropic case and is still described by v_c and has an axis specific compression time $t_c = L_x/(2v_c)$. As in the isotropic case, we start with a simulation with $t_d = 100t_c$, shown in figure 3.3 In the rapidly compressing simulation, the compression adds energy to σ_x , but leaves σ_y and σ_z unchanged. The result $\bar{\rho}\sigma_x^2 \propto \bar{\rho}^3$ is recovered.

Next, we consider the case with $t_d = 0.5t_c$ with anisotropic compression, shown in figure 3.4. At early times, σ_x in figure 3.4 behaves in a similar fashion to σ in figure 3.2, although off by $\sqrt{3}$. The difference is that σ_y and σ_z decay freely. The simulation eventually reaches a state where $\sigma_x \gg \sigma_y \sim \sigma_z$. As shown in Hansen et al. (2011), ϵ approaches zero in this case and therefore t_d approaches infinity. With the significantly reduced decay rate, figure 3.4 at late times approaches $\sigma_x \propto 1/L_x$ while σ_y and σ_z continue to decay.

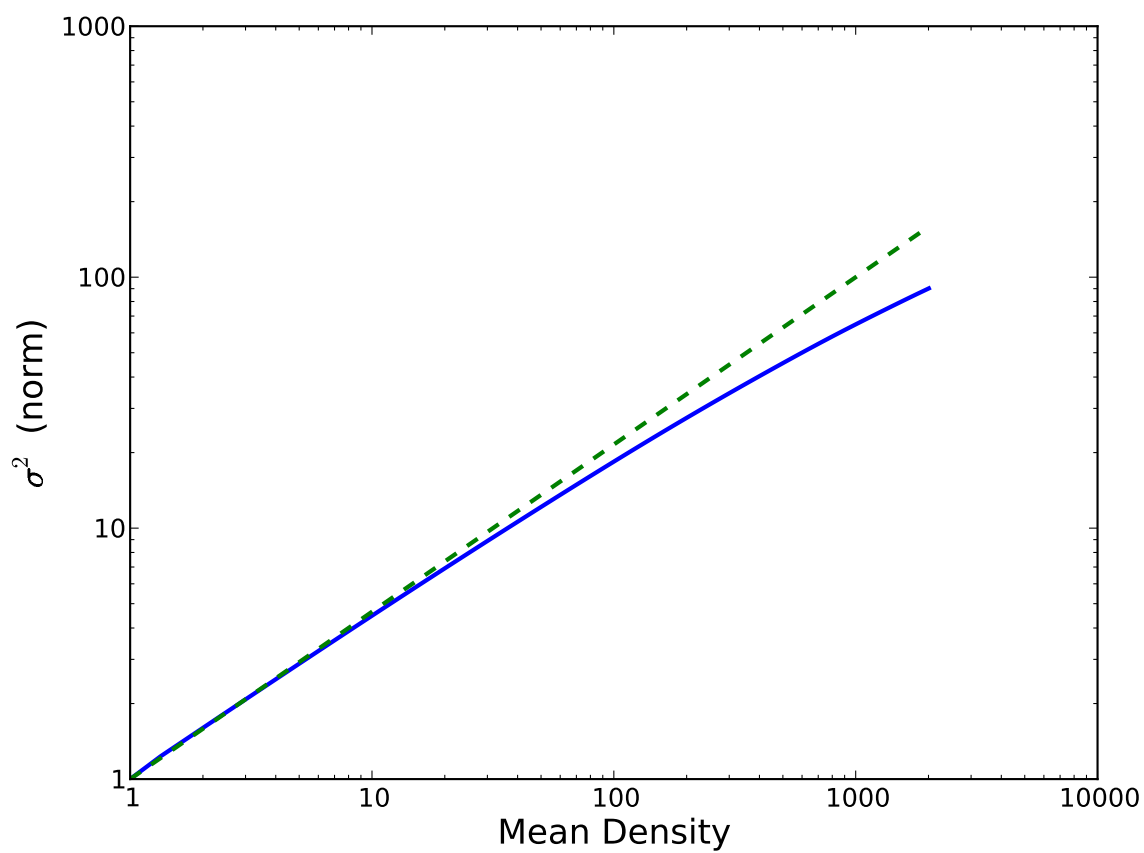


Figure 3.1 Specific turbulent energy vs mean density for rapidly compressed turbulence. The solid line represents the simulation data and the dashed line represents $\rho\sigma^2 \propto \rho^{5/3}$

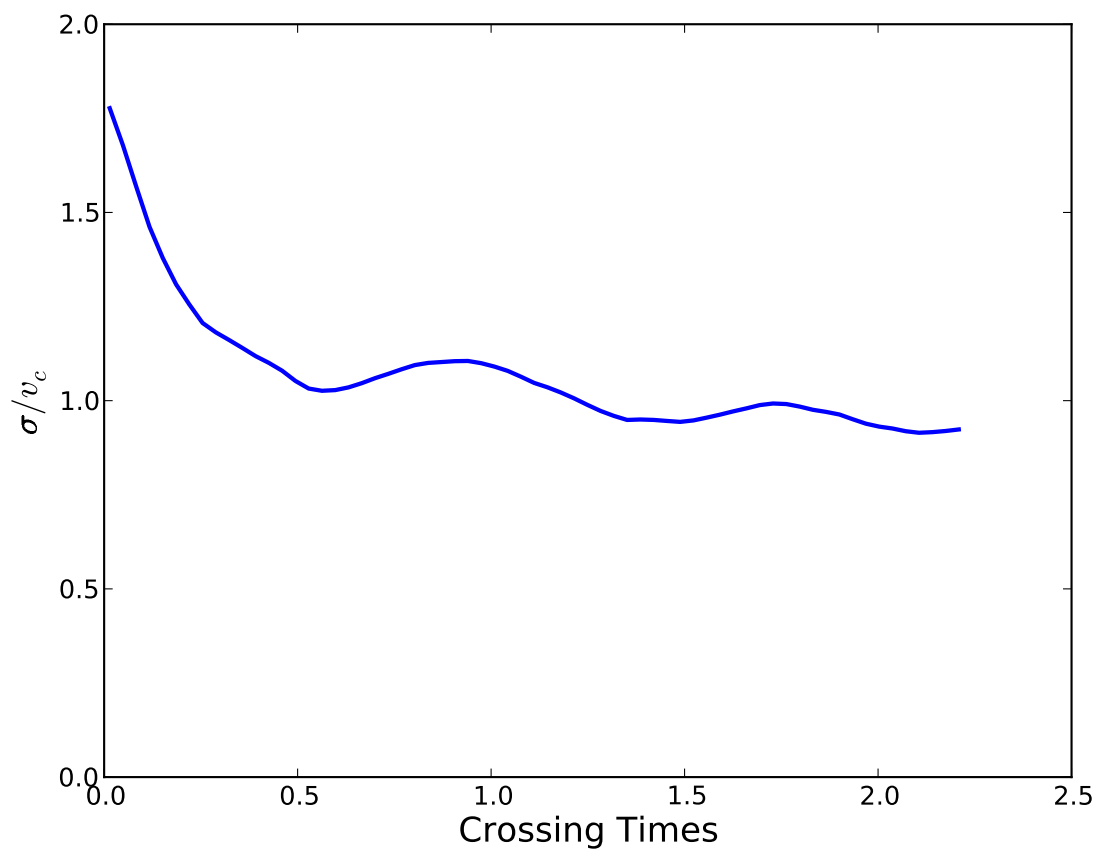


Figure 3.2 Turbulent velocity dispersion vs time for turbulence compressed with a compression time similar to the decay time

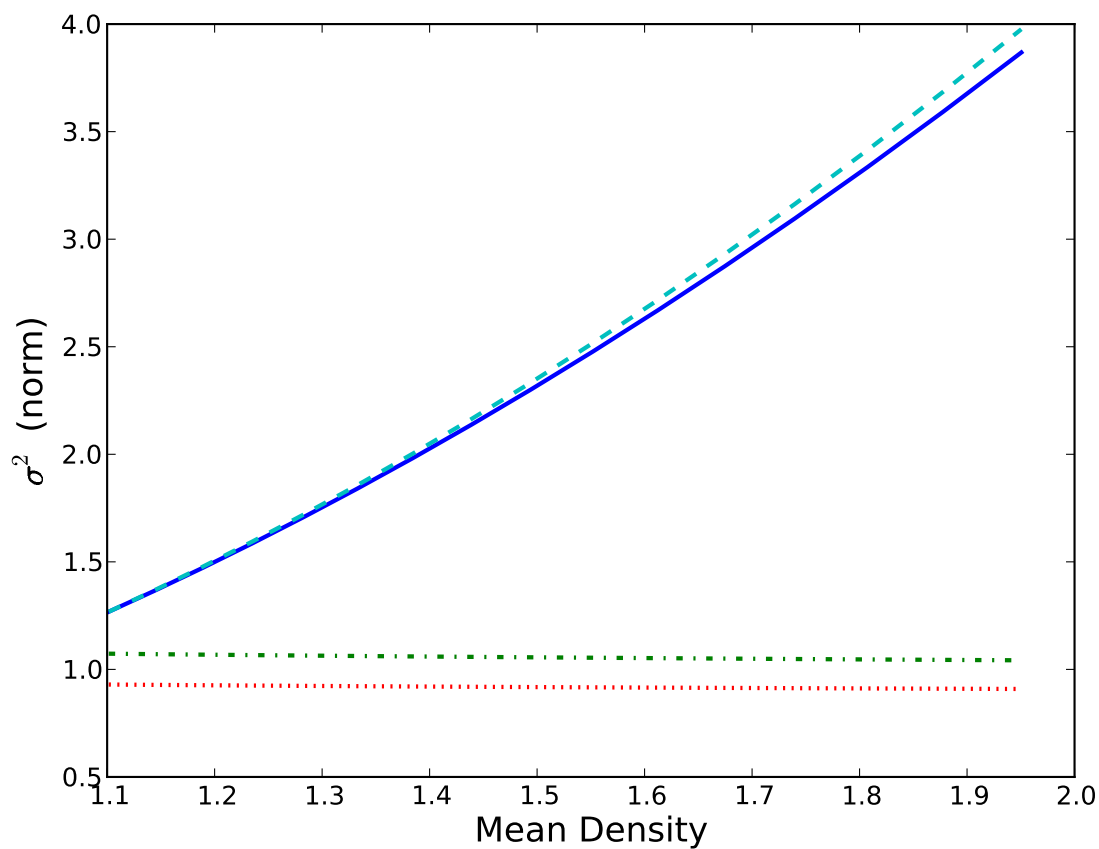


Figure 3.3 Specific turbulent energy vs mean density for turbulence rapidly compressed in the x direction. The solid line is the x energy, and the points represent the energy in the other two directions. The dashed line is $\rho\sigma_x^2 = \rho^3$ [need to run this longer]

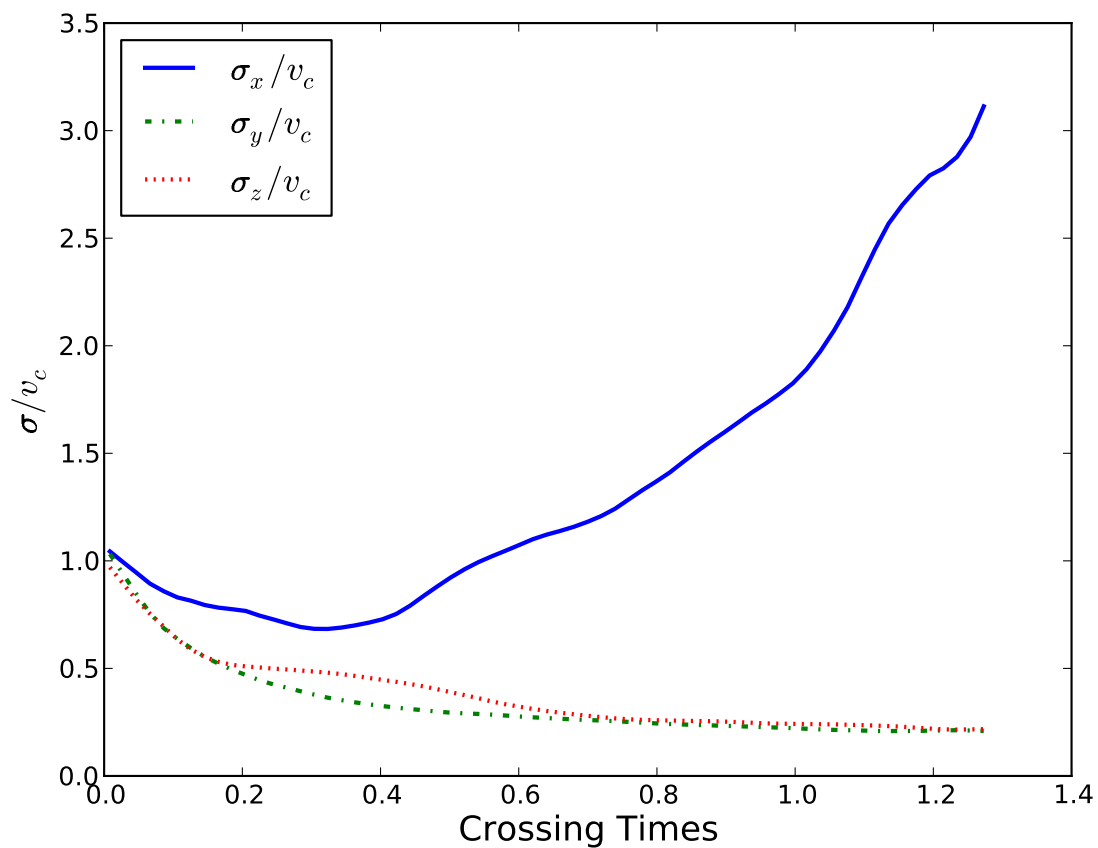


Figure 3.4 Turbulent velocity dispersion vs time for turbulence mildly compressed in the x direction. The solid line is the x energy, and the points represent the energy in the other two directions.

Isotropic compression cannot be solely responsible for regenerating turbulence in molecular clouds because it requires reducing the cloud to zero volume in a time similar to the decay time. Anisotropic compression, however, can offer a solution by compressing for a short amount of time. This will add some energy to the system, but the energy that it adds will all be in a single direction. This energy decays very slowly and can lead to arbitrarily slow turbulent decay rates (Hansen et al. 2011).

3.5 Conclusions

In order to determine the behavior of supersonic turbulence under compression, we derive a simple equation of state for turbulent pressure. This equation of state is equivalent to a $\gamma = 5/3$ monatomic gas under isotropic compression. To verify our derivation, we simulate decaying turbulence undergoing homologous contraction and recreate the derived equation of state. As a consequence of this equation of state, the velocity dispersion of turbulence will naturally asymptote to the velocity of its compression. Additionally, we explored the behavior of turbulence under anisotropic compression. Turbulent velocity dispersion σ_i in direction i follows the rule $\sigma_i \propto 1/a_i$, where a_i is the scale factor in direction i . This means that compression in one direction can impart energy into that direction while leaving the other two directions alone. This is verified with simulations. When this happens, the turbulence becomes extremely anisotropic and the decay rate goes to zero as shown in Hansen et al. (2011).

Chapter 4

Feedback Effects on Low Mass Star Formation

Abstract

Protostellar feedback, both radiation and bipolar outflows, dramatically effects the fragmentation and mass accretion from star-forming cores. We use ORION, an adaptive mesh refinement (AMR) gravito-radiation-hydrodynamics code, to simulate low-mass star formation in a turbulent molecular cloud in the presence of protostellar feedback. We present results for the first simulations of a star-forming cluster that include feedback from both radiative transfer and protostellar outflows. We run four simulations to isolate the individual effects of radiation feedback and outflow feedback as well as the combination of the two. We find that, while radiation suppresses fragmentation by itself, outflows reduce protostellar luminosities by a factor of ten, rendering protostellar radiation largely irrelevant above a mass scale of $0.05 M_{\odot}$. We find initial fragmentation of our cloud at the global Jeans length, around 0.1 pc. With insufficient protostellar radiation to stop it, these 0.1 pc cores fragment repeatedly, forming typically 10 stars each. The accretion rate in these stars scales with mass as predicted from core accretion models for star formation. We find that protostellar outflows do not significantly affect the overall cloud dynamics due to their small opening angles and poor coupling to the dense gas. The outflows do remove 2/3 of the mass from our cores, giving a core to star efficiency, $\epsilon_{\text{core}} = 1/3$. We are also able to reproduce many observation of local star-forming regions. Our simulation with radiation and outflows reproduces the observed protostellar luminosity function. All of our simulations can reproduce observed core mass functions, though we find they are sensitive to telescope resolution. We also reproduce the two-point correlation function of these observed cores. Lastly, we reproduce IMF itself, including the low-mass end, when outflows are included.

4.1 Introduction

The origin of the stellar initial mass function (IMF) is one of the most fundamental problems of star formation. The IMF can be described by single power law for stars above $0.5 M_{\odot}$ (Salpeter 1955), and a broken power law (Kroupa 2002) for stars below this mass. Alternatively, it can be described as a log-normal distribution with characteristic mass $m_c = 0.2 M_{\odot}$ that joins with the Salpeter power law for stars above $1.0 M_{\odot}$ (Chabrier 2005). Any theory of the IMF must explain both the functional form and the characteristic mass. A tantalizing observational clue to the functional form lies in dust observations in star-forming regions (Motte et al. 1998; Testi & Sargent 1998; Johnstone et al. 2000, 2001; Motte et al. 2001; Beuther & Schilke 2004; Stanke et al. 2006; Alves et al. 2007; Enoch et al. 2008; Sadavoy et al. 2010). These dust maps find many high density concentrations that are consistent with prestellar and protostellar cores. When the mass of these cores is calculated, the core mass function (CMF) has the same functional form as the IMF, but with a higher characteristic mass, ranging from $0.2 M_{\odot}$ to $1 M_{\odot}$. If each core is converted to a small number of stars with some efficiency, $0.2 < \epsilon_{\text{core}} < 1.0$, the IMF can be recreated.

The observed CMF provides support to core accretion theories of star formation (Shu 1977; McKee & Tan 2003), which start with a bound core and produce a single stellar system. Simulations of turbulence find the functional form of the core mass function (log-normal plus power law) is the expected outcome of supersonic turbulence (Padoan & Nordlund 2002; Padoan et al. 2007). Analytic predictions of a turbulent density field with self-gravity can also reproduce this functional form (Hennebelle & Chabrier 2008, 2009). The characteristic core mass is then the Jeans mass at some critical density and temperature. However, choosing the correct density and temperature is problematic. In purely isothermal turbulence, there is no characteristic Jeans mass. As objects collapse and the density increases, the Jeans mass decreases. There is no transition where this decrease in Jeans mass will stop without additional physics. This means the core masses are either infinitely small or functions of the global Jeans mass of the host molecular cloud. Observations are consistent with a universal IMF, however, even over a range of cloud Jeans masses (Kroupa 2002; Chabrier 2003; Bastian et al. 2010). This means the characteristic core mass must be set by local physics, which isothermal turbulence cannot provide. Star-forming regions are approximately isothermal because the thermal time scales are much shorter than the dynamical time scales, but there are ways to break this isothermality.

One approach is to focus on the coupling between gas and dust in star-forming environments (Larson 2005; Elmegreen et al. 2008). At low densities, gas-dust coupling is poor and the gas is theoretically slightly sub-isothermal (temperature decreases with increasing density). At higher densities, gas and dust are well coupled and the gas is theoretically slightly super-isothermal. This yields a critical density and temperature at the transition that can be converted into a Jeans mass. This critical density, $\rho \sim 10^{-19} \text{ g cm}^{-3}$, is lower than the densities of large star-forming regions like Orion, however, and unlikely to explain the characteristic core mass in these regions.

One critical mass is the point when dust becomes opaque to its own thermal radiation

(Low & Lynden-Bell 1976). At that density, the gas will heat up and raise the Jeans mass, creating a minimum Jeans mass of fragmentation. A barotropic simplification of this effect sets the mass in many simulations (e.g. Bate & Bonnell (2005); Bonnell et al. (2006); Offner et al. (2008); Hennebelle et al. (2011)). The density of this transition is extremely high ($\sim 10^{-13}$ g/cm³) (Masunaga et al. 1998) and the resulting Jeans mass ($\sim 0.004M_{\odot}$) is much lower than the characteristic core mass (Low & Lynden-Bell 1976; Whitworth et al. 2007). In addition, the barotropic approximation is inaccurate when compared to simulations that include dust radiation (Krumholz et al. 2007a; Offner et al. 2009b; Bate 2009; Price & Bate 2009). The importance of dust radiation can be seen in Bate (2009) and Price & Bate (2009), which include dust radiation, but effectively ignore protostellar luminosity. These studies found that the inclusion of dust radiation significantly suppresses the formation of brown dwarfs, showing dust radiation does raise the effective fragmentation mass compared to a barotropic equation of state.

The most powerful break from isothermality comes from protostellar radiation. Massive protostars are capable of heating an entire cloud (Krumholz et al. 2007a; Cunningham et al. 2011; Myers et al. 2011; Krumholz et al. 2011). Low-mass stars do not have the same thermal influence, but simulations show they can still dramatically reduce fragmentation and recover a $1 M_{\odot}$ characteristic core mass (Offner et al. 2009b; Krumholz et al. 2011). Protostellar radiation does not create a unique critical density, but it does weaken the density dependence of the effective Jeans mass (Bate 2009).

Given a core mass function, there is still the question of CMF to IMF efficiency. The primary mechanism for reducing the core mass is protostellar outflows. Stars of all masses show bipolar outflows during their formation (Richer et al. 2000; Shepherd 2003). These outflows remove mass that would otherwise accrete onto stars, thereby reducing the final mass (Matzner & McKee 2000; Arce & Sargent 2006; Wang et al. 2010). Analytical estimates of mass loss from winds can fully explain the range of mass loss expected from observations $0.2 < \epsilon_{\text{core}} < 1.0$ depending on the details of the cores and the outflows (Matzner & McKee 2000). The outflows travel beyond their stars of origin and deposit energy into parsec-scale turbulent motions. Evidence suggests that molecular cloud turbulence appears on the scale of the entire cloud (Ossenkopf & Mac Low 2002; Brunt et al. 2009), so is most likely driven by sources other than protostellar outflows. Nonetheless, the dynamics on parsec scales can be significantly altered by outflows (Norman & Silk 1980; McKee 1989; Li & Nakamura 2006; Banerjee et al. 2007; Nakamura & Li 2007; Swift & Welch 2008; Carroll et al. 2010; Arce et al. 2010; Wang et al. 2010). Lastly, outflows allow radiation to escape the protostellar core, promoting fragmentation (Cunningham et al. 2011).

In this paper, we will investigate the fragmentation of a parsec-scale molecular cloud into cores and then into stars. This requires refinement down to small scales to capture the fragmentation and radiative transfer to fragment at the correct mass scale, similar to Offner et al. (2009b). This also requires simulation of protostellar outflows, to capture the CMF to IMF efficiency, similar to Cunningham et al. (2011). The goal of this paper is to explain both the observed CMF and the IMF while self-consistently finding ϵ_{core} . In order to do this, we will perform the first simulation of a star-forming cluster to include both radiative

Name	Thermal Physics	Winds?	Finest Resolution [AU]
B	Barotropic	No	32
BW	Barotropic	Yes	32
R	Radiation	No	32
RW	Radiation	Yes	32

Table 4.1 Table of simulations

transfer and protostellar outflows.

We describe our numerical method and simulation setup in §2. In §3, we report the results of our simulations. We discuss the implications of our results on star formation theory and compare to observations in §4. We summarize our conclusions in §5.

4.2 Simulations

We perform four primary simulations with nearly identical initial conditions but different physics. These simulations all include hydrodynamics, gravity and basic sink particle physics, but may also include radiation and/or sink particle outflows. The simulations are shown in table 4.1

4.2.1 Initial Conditions

All simulations have the same initial conditions, also used in Offner et al. (2009b). The initial gas temperature is $T_g = 10$ K, the box length is $L = 0.65$ pc and the average density is $\bar{\rho} = 4.46 \times 10^{-20}$ g cm $^{-3}$, corresponding to $n_H = 1.91 \times 10^4$ cm $^{-3}$. The total box mass is $185 M_\odot$. When appropriate, the radiation temperature, T_r is initialized to 10 K. The radiation energy density is thus $E = aT_r^4 = 7.56 \times 10^{-11}$ erg cm $^{-3}$.

To obtain the turbulent initial conditions, we begin without self-gravity and apply velocity perturbations to an initially constant density field using the method described in Mac Low (1999). These perturbations correspond to a Gaussian random field with flat power spectrum in the range $1 \leq k \leq 2$. These perturbations continue for three cloud crossing times and then stop. At this point the turbulence follows a Burgers power spectrum, $P(k) \propto k^{-2}$, characteristic of supersonic hydrodynamic turbulence. The 3D turbulent Mach number is $\mathcal{M} = 6.6$, which gives a 3D rms velocity dispersion, $\sigma_v = 1.2$ km/s. We choose the Mach number so that the cloud is approximately virialized:

$$\alpha_{\text{vir}} = \frac{5\sigma^2}{GM/R} \simeq 1. \quad (4.1)$$

This is slightly above the linewidth-size relation $\sigma \simeq 0.7(R/1 \text{ pc})^{1/2}$ km s $^{-1}$ (Solomon et al. 1987; Heyer & Brunt 2004), and is equivalent to $\sigma = 1.2(R/1 \text{ pc})^{1/2}$ km s $^{-1}$, which is well within the observed range (e.g. Falgarone et al. 2009)

After driving for three cloud crossing times, we then turn off driving, turn on gravity and follow the subsequent gravitational collapse for approximately one global free fall time:

$$t_{\text{ff}} = \sqrt{\frac{3\pi}{32G\bar{\rho}}} = 0.315 \text{ Myr}, \quad (4.2)$$

where $\bar{\rho}$ is the mean density of the box. The simulations with radiation become prohibitively computationally expensive at late times and are stopped at $t = 0.83 t_{\text{ff}}$ with a total stellar mass of $30 M_{\odot}$ for simulation R. The barotropic simulations are continued to $t = 1.05 t_{\text{ff}}$ before they are stopped. At this time the total stellar mass in simulation B is $50 M_{\odot}$ compared to the total simulation mass of $185 M_{\odot}$. There is still gas bound to protostars when the simulations end, totaling $11 M_{\odot}$. Our stellar mass estimates may therefore be too low by 20%.

Given our temperature of 10 K, the Jeans length at $\bar{\rho}$ is

$$\lambda_J = \left(\frac{\pi c_s^2}{G\bar{\rho}}\right)^{1/2} = 0.20 \text{ pc}, \quad (4.3)$$

and the Jeans mass is

$$M_J = \frac{4\pi}{3} \left(\frac{\lambda_J}{2}\right)^3 \bar{\rho} = 2.7 M_{\odot}. \quad (4.4)$$

The turbulent Jeans mass, at density $\rho = \mathcal{M}^2 \bar{\rho}$, is $0.4 M_{\odot}$.

The calculations have a 256^3 base grid with 4 levels of refinement by factors of 2, giving an effective resolution of 4096^3 . This resolution corresponds to $\Delta x_4 = 32 \text{ AU}$.

4.2.2 Evolution Equations

We use the parallel adaptive mesh refinement code ORION for our simulations. The numerical method is nearly identical to previous papers (Krumholz et al. 2007a; Offner et al. 2009b; Cunningham et al. 2011; Krumholz et al. 2011; Myers et al. 2011). ORION solves the equations of compressible gas dynamics including self-gravity, radiative transfer, and radiating star particles, all on an adaptive grid. Every cell in the grid has four conserved quantities: mass density, ρ , vector momentum density, $\rho \mathbf{v}$, gas energy density, ρe , and radiation energy density, E . These conserved quantities can be used to calculate derived quantities such as velocity, \mathbf{v} , and pressure, P . In addition to the gas quantities, we evolve point-mass star particles, each with a position \mathbf{x}_i , mass M_i , momentum \mathbf{p}_i , angular momentum, \mathbf{j}_i and luminosity L_i . The subscript i refers to the star particle number. The particle method is explained in Krumholz et al. (2004) (hereafter KKM04), with the addition of radiation (Krumholz et al. 2007a) and outflows (Cunningham et al. 2011). The full set of evolution equations for gas and particles is

$$\frac{\partial \rho}{\partial t} + \nabla \cdot (\rho \mathbf{v}) + \sum_i [\dot{M}_{KKM04} W(\mathbf{r}_i) - \dot{M}_{w,i} W_w(\mathbf{r}_i) \xi(\theta_i)] = 0, \quad (4.5)$$

$$\frac{\partial \rho \mathbf{v}}{\partial t} + \nabla \cdot (\rho \mathbf{v} \mathbf{v}) = -\nabla P - \rho \nabla \phi - \sum_i (\dot{\mathbf{p}} W(\mathbf{r}_i) - \dot{M}_{w,i} v_{w,i} W_w(\mathbf{r}_i) \xi(\theta_i) \cdot \hat{\mathbf{r}}_i), \quad (4.6)$$

$$\begin{aligned} \frac{\partial(\rho e)}{\partial t} + \nabla \cdot [(\rho e + P) \mathbf{v}] &= \rho \mathbf{v} \nabla \phi - \kappa_R \rho (4\pi B - cE) - \left(\frac{\rho}{\mu m_H} \right)^2 \Lambda(T_g) - \\ &\sum_i \left[\dot{\epsilon}_{KKM04} W(\mathbf{r}_i) - \dot{M}_{w,i} W_w(\mathbf{r}_i) \xi(\theta_i) \frac{k_B T_w K}{\mu(\gamma - 1)} \right], \end{aligned} \quad (4.7)$$

$$\frac{\partial}{\partial t} E - \nabla \cdot \left(\frac{c\lambda}{\kappa_R \rho} \nabla E \right) = \kappa_P \rho (4\pi B - cE) + \left(\frac{\rho}{\mu m_H} \right)^2 \Lambda(T_g) + \sum_i L_i W(\mathbf{r}_i), \quad (4.8)$$

$$\nabla^2 \phi = -4\pi G [\rho + \sum_i M_i \delta(\mathbf{r}_i)], \quad (4.9)$$

$$\dot{M}_i = \frac{1}{1 + f_w} \dot{M}_{KKM04}, \quad (4.10)$$

$$\dot{M}_{w,i} = f_w \dot{M}_i = \frac{f_w}{1 + f_w} \dot{M}_{KKM04}, \quad (4.11)$$

$$\dot{\mathbf{p}}_i = \dot{\mathbf{p}}_{KKM04}, \quad (4.12)$$

$$\mathbf{r}_i = \mathbf{x} - \mathbf{x}_i, \quad (4.13)$$

$$\theta_i = \arccos(\hat{\mathbf{r}}_i \cdot \hat{\mathbf{j}}_i). \quad (4.14)$$

The quantities entering these equations are defined below. Equations (4.5) and (4.6) are the fluid equations for mass and momentum, modified to include particles. Equations (4.7) and (4.8) are the energy equations for gas and radiation respectively. The Poisson equation for the gravitational potential, ϕ is given by equation (4.9). The particle evolution is given by equations (4.10), (4.11) and (4.12). We use periodic boundary conditions for all gas and particle quantities.

For the radiative runs, we adopt Marshak boundary conditions for the radiation field. This allows radiation to escape from the box as it would from a molecular cloud. The equation of state for the gas is given by

$$P = \frac{\rho k_B T_g}{\mu m_H} = (\gamma - 1) \rho \left(e - \frac{v^2}{2} \right), \quad (4.15)$$

where $\mu = 2.33$ is the mean molecular weight for molecular gas of Solar composition and γ is the ratio of specific heats. We adopt, $\gamma = 5/3$, representing a monatomic ideal gas¹. The term $\kappa_P \rho (4\pi B - cE)$ represents energy exchanged between the radiation field and the dust

¹We choose a monatomic γ because most of the simulation domain is too cold to rotationally excite molecular hydrogen

in our gas, with $B = caT_g^4/4\pi$ representing the Planck emission function. The opacities κ_P and κ_R are given by the dust opacities from the iron normal, composite aggregates dust model of Semenov et al. (2003). We assume that the gas and the dust are thermally coupled. When the gas temperature exceeds the dust destruction temperature, the energy exchange term goes to zero and the gas and radiation unrealistically decouple. To address cooling from gas above the dust destruction temperature, we use the line cooling function $\Lambda(T_g)$ from Cunningham et al. (2006). This removes energy from the gas and adds that energy to the radiation field (see Cunningham et al. (2011) for further details). The radiation flux limiter is given by $\lambda = \frac{1}{R} (\coth R - \frac{1}{R})$, where $R = |\nabla E|/\kappa_R \rho E$ (Levermore & Pomraning 1981). It should be noted that we have excluded the radiation pressure and radiation enthalpy advection terms from equation (4.8) that appear in the analogous equation in Krumholz et al. (2007a). This approximation is justified in the formation of low-mass stars, as shown in Offner et al. (2009b).

For the non-radiative runs, the energy exchange term from equation (4.7) disappears, and we close the system of equations with a barotropic equation of state for the gas pressure:

$$P = \rho c_s^2 + \left(\frac{\rho}{\rho_c}\right)^\gamma \rho_c c_s^2, \quad (4.16)$$

where $c_s = \sqrt{k_B T / \mu m_H}$ is the isothermal sound speed, $\gamma = 5/3$ and ρ_c is the critical density. The critical density determines the transition from isothermal to adiabatic regimes and we adopt $\rho_c = 2 \times 10^{-13} \text{ g cm}^{-3}$ to agree with the collapse solution from Masunaga et al. (1998) prior to H_2 dissociation.

The particle quantities \dot{M}_{KKM04} , $\dot{\mathbf{p}}_{KKM04}$ and $\dot{\epsilon}_{KKM04}$ represent the sink particle accretion rates of mass, momentum and energy from the surrounding gas in the absence of winds as given by KKM04, with the function W representing a window function over the accretion zone of the particle. A fraction, $f_w = 0.3$, of the accreted mass for each particle is injected back into the surrounding gas at velocity $v_{w,i}$ and temperature $T_w = 10^4 \text{ K}$ along the direction of the angular momentum vector of the particle. The wind speed is set by the Keplerian speed at the surface of the star, $v_{k,i} = \sqrt{GM_i/r_{*,i}}$ where $r_{*,i}$ is the protostellar radius, but is capped at 60 km s^{-1} for computational speed. Specifically, $v_{w,i} = \min(v_{k,i}, 60 \text{ km s}^{-1})$. The velocity cap has a similar effect to the choice of Cunningham et al. (2011) to use $v_{w,i} = v_{k,i}/3$ for the most massive stars in the calculation. The wind is injected over a window function W_w that is slightly larger than W for numerical reasons. The exact angular distribution of the wind is described in the function ξ . The functional form is taken from Matzner & McKee (1999) as implemented in Cunningham et al. (2011),

$$\xi(\theta, \theta_0) = \left[\ln \left(\frac{2}{\theta_0} \right) (\sin^2 \theta + \theta_0^2) \right]^{-1}, \quad (4.17)$$

where θ_0 is a flattening parameter that sets the opening angle of the wind. We use the fiducial value of $\theta_0 = 0.01$. We update the luminosity of each star, L_i , using the protostellar evolution model described in the appendices of Offner et al. (2009b).

So far, the evolution equations can be described as the fluid and radiation equations from Offner et al. (2009b) combined with the particle equations and line cooling of Cunningham et al. (2011), but there is one important modification. In the KKM04 sink particle methodology, all particles with overlapping accretion zones are merged together. This gives an effective merger radius of 8 cells, or 256 AU at a grid resolution of 32 AU. To limit this effect, we changed the merger radius to 4 cells, representing the point when a particle is in the accretion zone of another particle. This gives an effective merger radius of 128 AU at our resolution. Even with this improvement, our particle algorithm will unrealistically merge stars that pass within 128 AU. To address this, we have implemented a mass limit of $m_{\text{merge}} = 0.05 M_{\odot}$, above which stars do not merge. This limit is chosen to correspond to the mass at which a protostar's core temperature becomes high enough to dissociate molecular hydrogen and initiate second collapse (Masunaga et al. 1998; Masunaga & Inutsuka 2000). Before second collapse, protostars are extended balls of gas with radii of a few AU and have a much higher collisional cross-section than main sequence stars. After second collapse, stellar mergers should be extremely rare and we do not allow them. This approach is also used in Myers et al. (2011). The effects of this choice are explored in §4.9.

ORION utilizes a second order Godunov scheme to solve the equations of compressible gas dynamics (Truelove et al. 1998; Klein 1999). These are equations (4.5)-(4.7), excluding terms from stars and radiation. The Poisson equation (4.9) is solved using a multi-grid iteration scheme (Truelove et al. 1998; Klein 1999; Fisher 2002). The flux-limited diffusion radiation equation (4.8) and the radiation terms in equation (4.7) are solved using the conservative update scheme from Krumholz et al. (2007b) modified to include the pseudo-transient continuation of Shestakov & Offner (2008).

We use the Truelove criterion (Truelove et al. 1997) to determine the addition of new AMR grids so that the gas density in the calculation always satisfies

$$\rho < \frac{J^2 \pi c_s^2}{G(\Delta x_l)^2}, \quad (4.18)$$

where Δx_l is the cell size on level l . We adopt a Jeans number of 0.125. In the simulations with radiative transfer, it is necessary to resolve the spatial gradients in the radiation field. Areas of high radiation gradients are near accreting stars, which tend to already be refined under the Truelove criterion. This is not always true for more evolved stars, which have higher luminosities and have accreted the dense gas that would trigger refinement. We find that the radiation gradients are adequately resolved by refining whenever $|\nabla E| \Delta x_l / E > 0.25$.

4.3 Results

4.3.1 Large Scale Evolution

The evolution of the barotropic simulations is depicted in Figure 4.1. Figures 4.2 and 4.3 depict the evolution of the radiative simulations without and with winds, respectively.

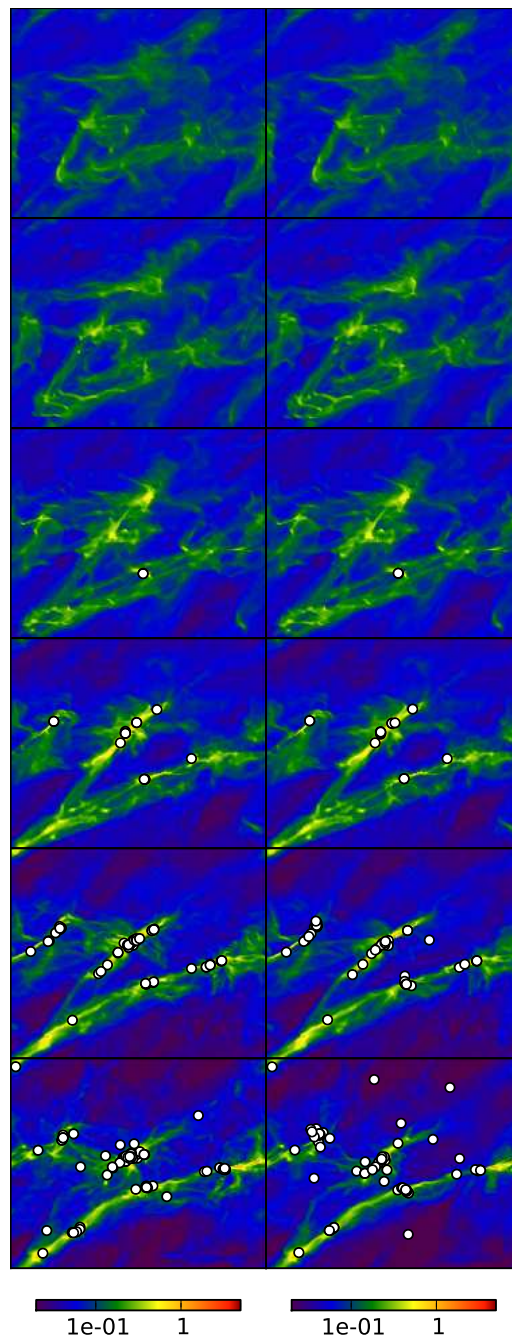


Figure 4.1 Column density of the entire simulation domain for BW (left) and B (right) at times 0, 0.2, 0.4, 0.6, 0.8 and 1.0 t_{ff} from top to bottom. Star particles are marked with white circles. There is very little difference on the domain scale with and without winds for the barotropic simulations.

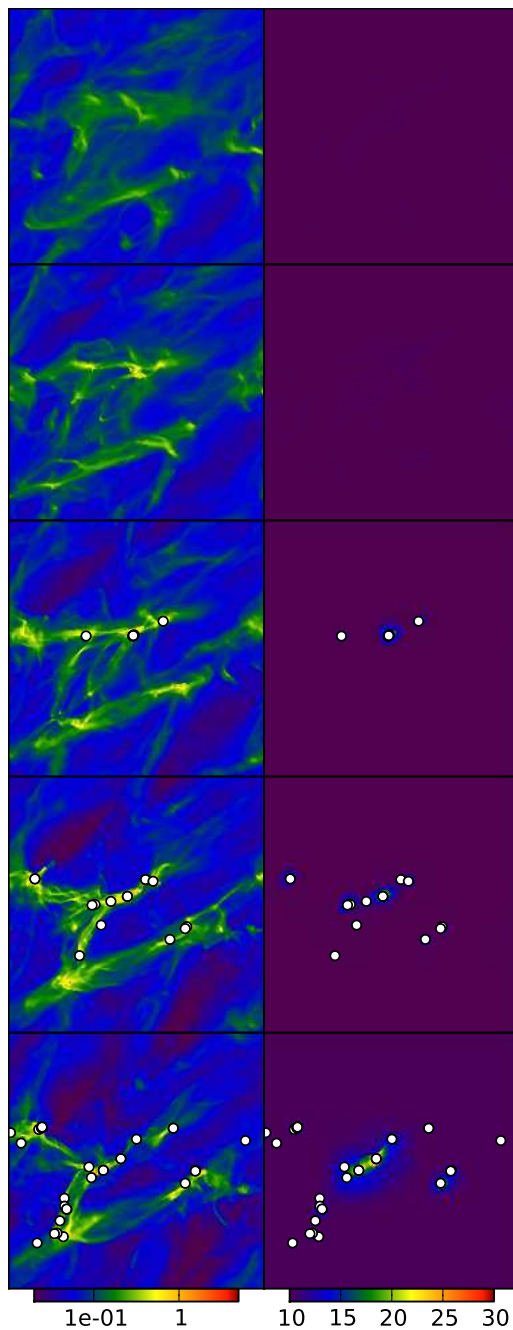


Figure 4.2 Column density (left) and density weighted Temperature (right) for simulation R at times 0, 0.2, 0.4, 0.6, and 0.8 t_{ff} from top to bottom. Particles are marked with white circles.

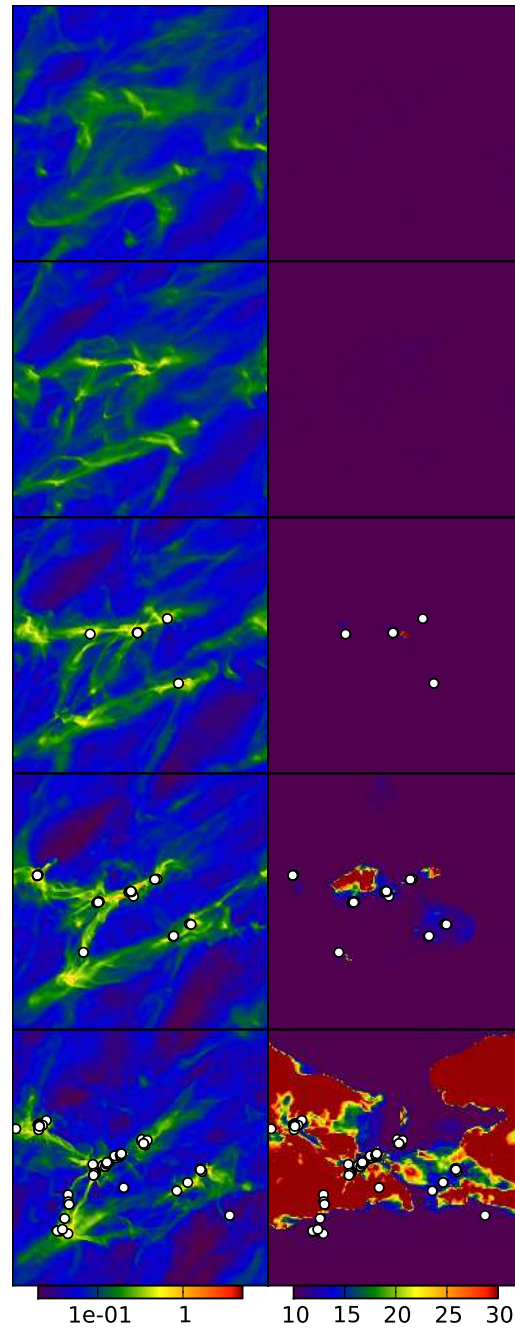


Figure 4.3 Same as Figure 4.2, but for simulation RW. The high temperature regions are the paths of outflows. It only takes a small amount of gas at 10^4 K to move the average temperature above 30 K through that line of sight.

In all simulations, for $t \lesssim 0.4t_{\text{ff}}$, there are cloud-scale filaments that slowly contract, allowing 3 turbulent cores of width $\sim 20,000$ AU to form. This length is half the Jeans length at the average cloud density. At this point, the cores begin to fragment, while new cores form, eventually forming 6 fully developed cores. These cores each have a central stellar system with $\sim 75\%$ of the stellar mass in the core and an additional group of low-mass stars, totalling ~ 10 stars per core. These cores with multiple stars generally resemble observed high-stellar-density cores (Teixeira et al. 2007; Chen & Arce 2010). There are an additional 20 stars in unfinished cores that form near the end of the simulation, giving a global total of 80 stars. Three of the cores coalesce by the end of the simulation to form a single group of 30 stars.

The evolution of the 3D rms velocity dispersion, σ_v , is shown in Figure 4.4. The global turbulence decays until star formation kicks in at $t \sim 0.5t_{\text{ff}}$. There are two main mechanisms for star formation to increase σ_v . First, as stars accrete mass and deepen their gravitational potential, the surrounding gas can convert gravitational energy into kinetic energy as it falls into the stars. This is shown in the gradual increase in Mach number for $t > 0.6t_{\text{ff}}$ in the B simulation. This effect is strong enough to return σ_v to near its original virialized value by itself. In rare cases, a many-body close encounter between stars will eject some gas at high velocities. There is not much momentum injected this way and the energy quickly dissipates, but it causes spikes in σ_v for the barotropic simulations, which have more small-scale fragmentation and therefore more many-body close encounters. The second mechanism occurs when protostellar winds are included. Some mass accreted onto stars is directly injected around the stars at high velocities. This causes the smooth increase in σ_v for simulations BW and RW as well as spikes from events with particularly high accretion rates that lead to bursts in wind momentum.

The total momentum injected by winds for model BW is shown in Figure 4.5. For comparison, a characteristic value of the magnitude of the momentum associated with internal motions in the cloud, $M_{\text{cloud}}\sigma_v$ is also plotted. For $t > 0.8t_{\text{ff}}$, the total momentum that has been injected by the winds is greater than the characteristic cloud momentum. At this point, the total amount of turbulent momentum that has been dissipated (including dissipation of wind momentum) is roughly the total amount of momentum that has been injected by the winds. By the end of the BW and RW simulations, the total wind momentum injected into the cloud is over twice the characteristic cloud momentum. The kinetic energy injected from the winds dissipates over time, suggesting a steady-state solution where the velocity dispersion of the cloud is constant with time as the winds replenish energy as quickly as it can dissipate.

4.3.2 Evolution of the Protostellar Population

The total mass in stars and the total number of stars as functions of time is shown in Figures 4.6 and 4.7. The realization of the initial turbulence is slightly different between the radiative and barotropic simulations, so star formation begins at different times. The first stars form at $t = 0.2t_{\text{ff}}$ for the radiative simulations and $t = 0.35t_{\text{ff}}$ for the barotropic

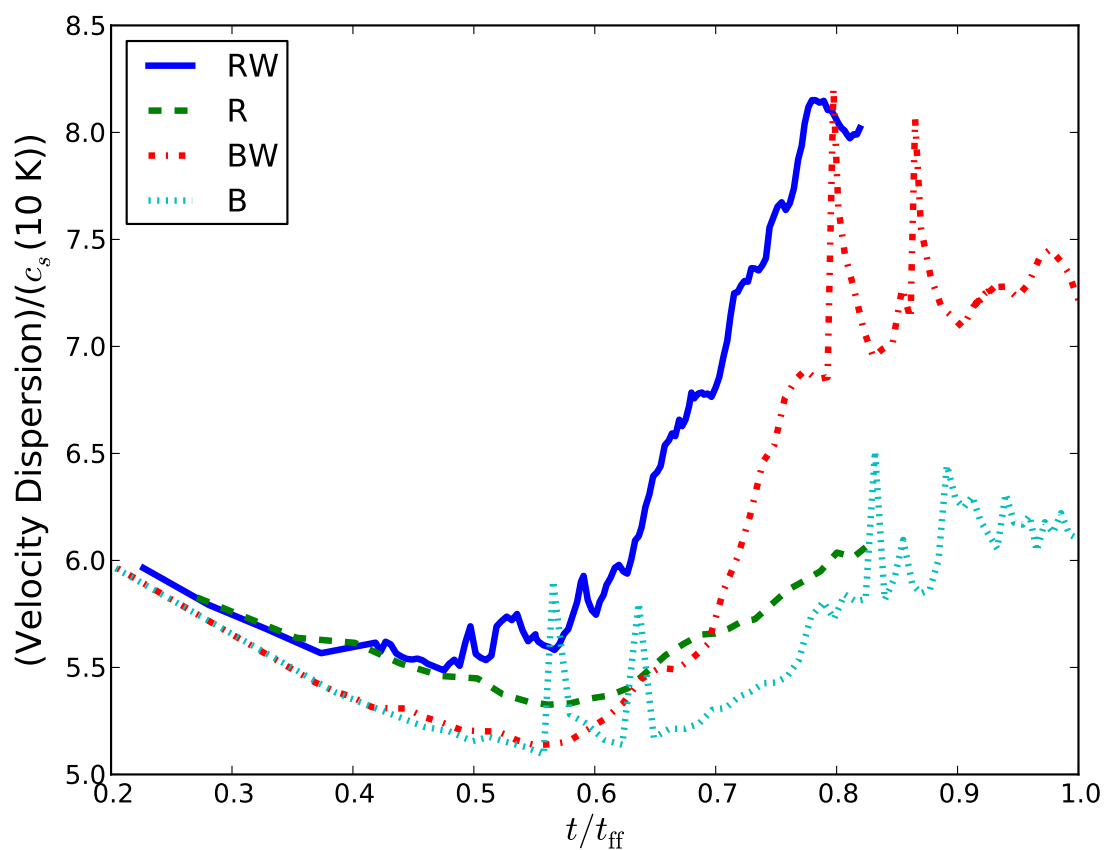


Figure 4.4 Time evolution of global rms Mach number for simulations with and without winds and with and without radiation. The turbulent energy in all simulations decays for half a global free fall time, at which point gravitational potential energy from stars is converted into kinetic energy, which raises the rms velocity. When winds are included, they contribute over twice as much energy as gravity itself.

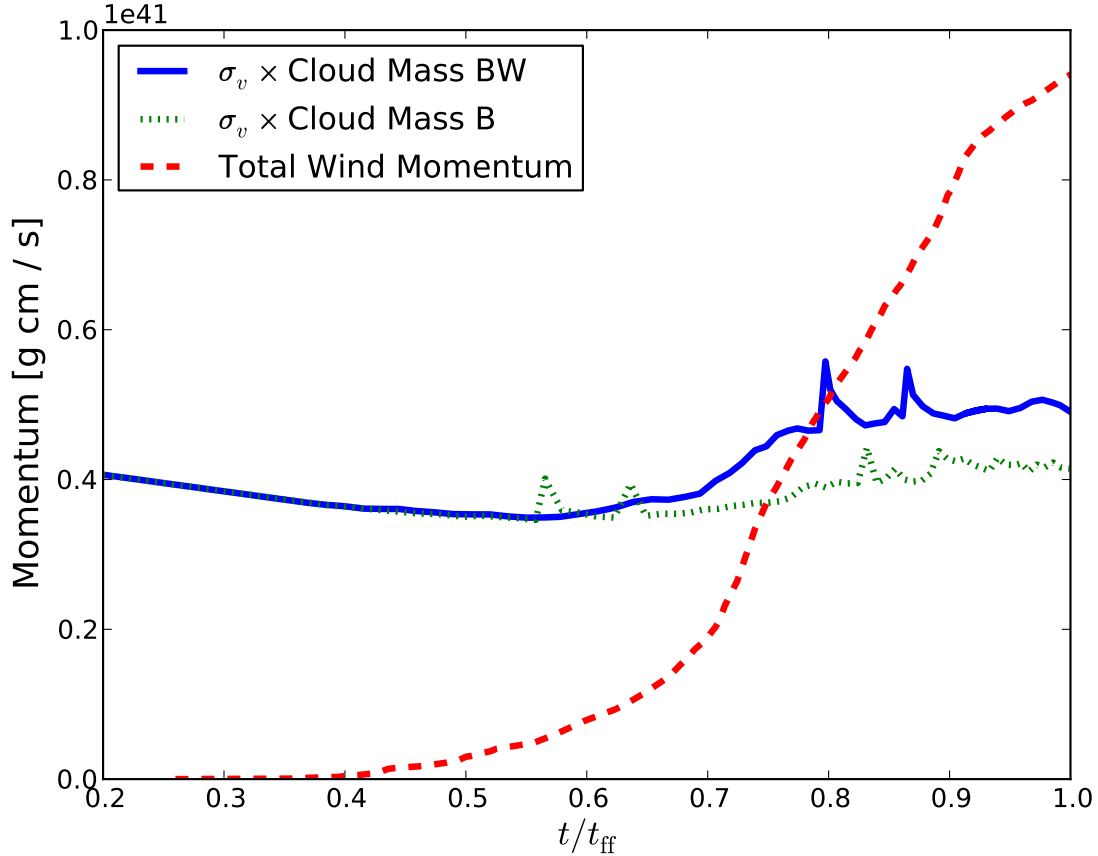


Figure 4.5 Total momentum that has been injected by wind over time for the barotropic simulations. For comparison, the total mass of the simulation multiplied by the velocity dispersion is also plotted. The total wind momentum integrates all injected momentum over time, even from winds that have decayed. This way the amount of injected momentum is eventually higher than the actual momentum of the cloud.

simulations. The turbulence overlaps enough between the two cases, however, that at later times the total mass in stars is similar for the two cases. Winds reduce the mass in stars by about a factor of 3 in both the radiative and barotropic cases. The number of stars does not change between BW and B, implying winds do not cause or suppress fragmentation by themselves. The number of stars in RW is significantly greater than in R, however, because protostellar luminosity inhibits fragmentation and the winds reduce that luminosity. The three simulations other than R show a dramatic increase in the number of stars at $0.6 t_{\text{ff}} < t < 0.8 t_{\text{ff}}$.

The evolution of median stellar mass is shown in Figure 4.8. This is a rough proxy for the characteristic mass of the protostellar mass function. Note that it will always be lower

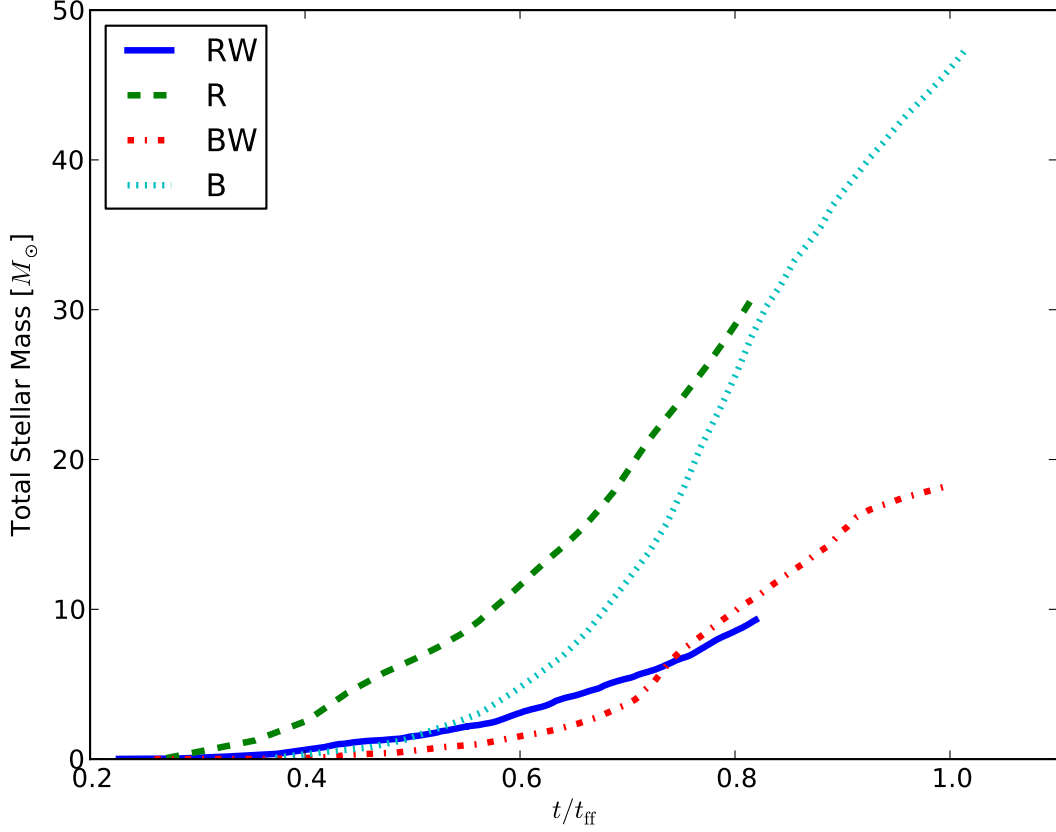


Figure 4.6 Total mass in stars as a function of time for the four main simulations. The mass of the entire simulation domain is $180 M_{\odot}$.

than the median mass of the IMF, because not all of the stars are finished accreting. Both BW and RW maintain a median around $0.05 M_{\odot}$ (similar to that of the protostellar mass functions in McKee & Offner (2010)) throughout the simulation. The median does increase for simulation BW around $t > t_{\text{ff}}$ as the formation rate of new stars decreases. The median of B fluctuates more, but is around $0.2 M_{\odot}$. Lastly, R maintains a median around $0.5 M_{\odot}$. This general behavior should be expected. The median mass is lowest when winds are included and highest when radiation is allowed to suppress fragmentation. The case with both winds and radiation ends up similar to BW because winds reduce protostellar luminosities.

The global luminosity evolution for the radiative simulations is plotted in Figure 4.9. The winds reduce the total luminosity by a factor of up to 10 at any given time. This is expected since the accretion luminosity is

$$L_{\text{acc}} \simeq \frac{GM_{\star}\dot{M}_{\star}}{R_{\star}}; \quad (4.19)$$

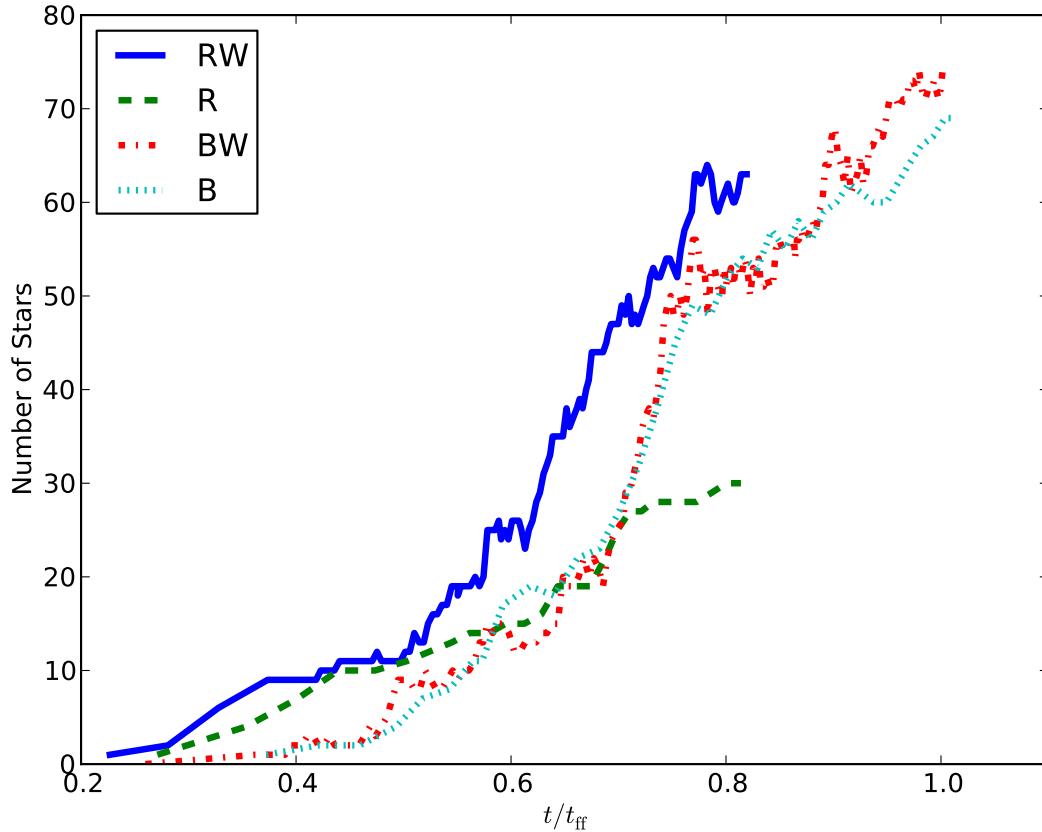


Figure 4.7 Number of stars as a function of time for the four main simulations. In the barotropic case, the number of stars is unaffected by winds. In the radiative case, radiation suppresses the number of stars unless wind is present.

given that the total mass in stars M_\star is reduced by a factor of 3 when winds are included, and the total accretion rate of stars \dot{M}_\star is also reduced by 3, the total luminosity is therefore reduced by a factor of 9 assuming the stellar radii, R_\star , do not change. Main sequence stars typically have a positive correlation between mass and radius, suggesting the factor of 9 is an upper limit. However, at any given point in time, many stars in our simulations are in the degenerate regime where mass and radius are negatively correlated (Chabrier et al. 2009), which counteracts the positive correlation from the higher mass stars and keeps the total luminosity ratio near 9.

The average stellar luminosity is shown in Figure 4.10. As was seen in the plot of total luminosity, the mean and median values of protostellar luminosity are much lower when winds are included. The disparity in average luminosity is even greater than the disparity in total luminosity because there are fewer stars when winds are excluded. The average

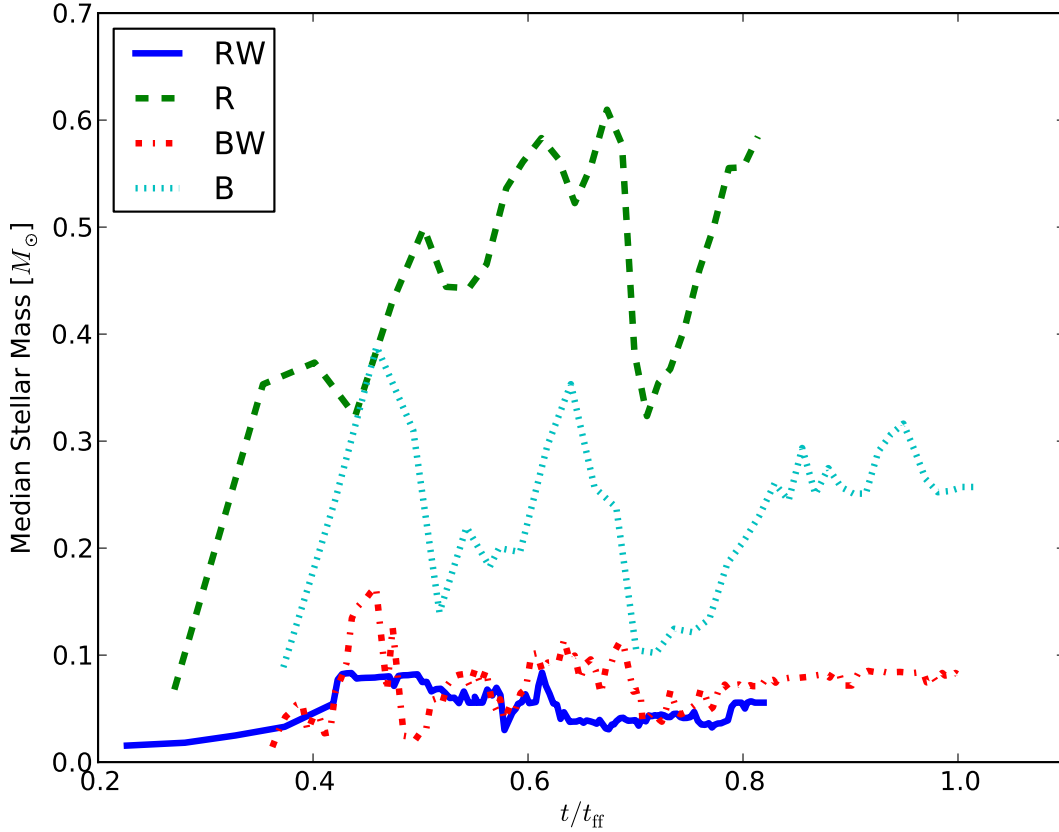


Figure 4.8 Median mass of stars as a function of time for the four main simulations. The two cases with winds maintain low medians throughout the simulations. The case with radiation without winds (case R) is able to suppress fragmentation and star formation largely stops as the original stars accrete mass.

luminosity in simulation R is heavily influenced by a single $6.6 M_{\odot}$ star that accounts for over half the total luminosity in the simulation. Unlike the low-mass stars, most of this luminosity is powered by nuclear fusion rather than accretion. Protostellar luminosities will be discussed further in section 4.4.3

4.3.3 Thermal Evolution

All simulations start at a background temperature of 10 K and are bathed in 10 K radiation. Stellar radiation and mechanical energy from protostellar outflows, can raise this temperature. We have identified gas heated above 12 K as thermally affected by stellar feedback. This represents all gas with energy density, $\propto T^4$ at least twice that of 10 K

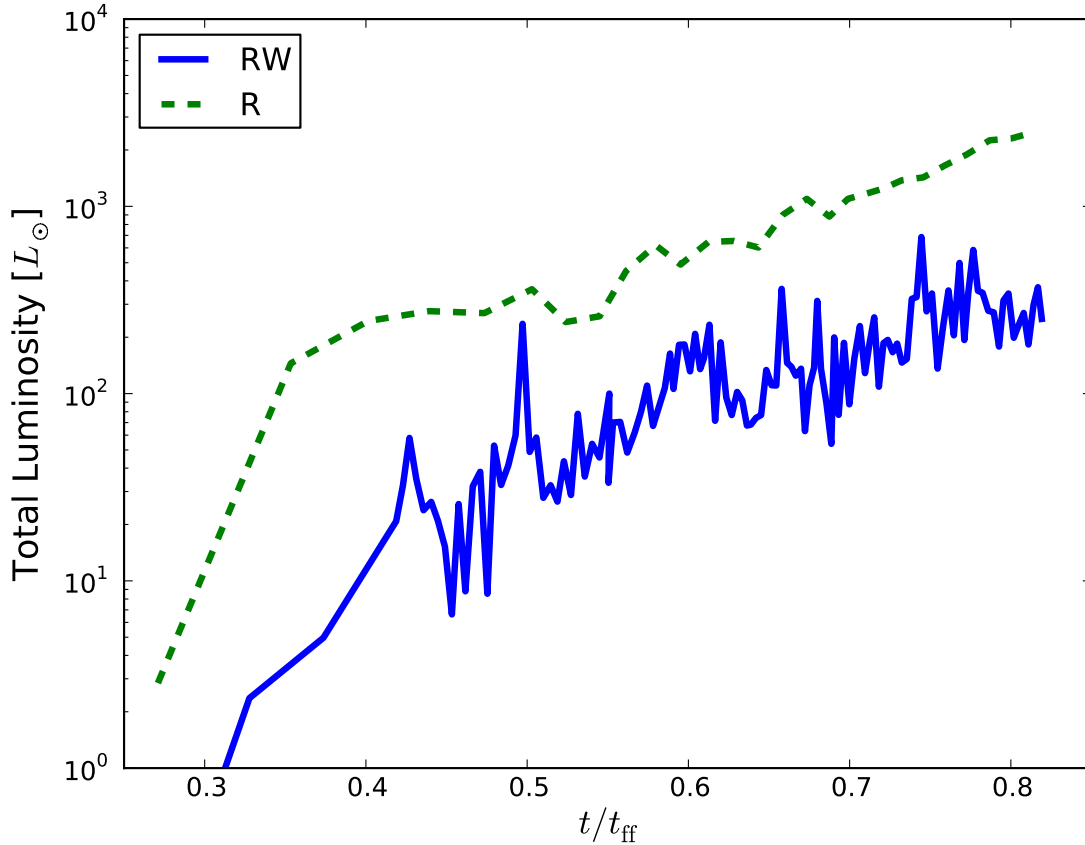


Figure 4.9 Total stellar luminosity versus time for simulations with radiation both with and without winds. Winds dramatically lower the radiation.

gas. The total mass of this gas is shown in Figure 4.11. The simulation with winds has significantly less heated gas than the simulation without winds. This is due to the reduced luminosity caused by the winds shown in Figure 4.9. In each simulation, the mass in heated gas roughly follows the mass in stars. When winds are included, there is a relative bump from wind-heated gas, though this is much smaller than the overall reduction in gas heated from stellar luminosity.

To further explore the heated gas, temperature-density phase plots with and without winds are shown in Figure 4.12. The phase plots with and without winds are notably different in two areas. First, the wind gas fills the high-temperature, low-density domain, while the same domain is empty without winds. Second, high-density gas with $\rho > 10^{-16} \text{ g/cm}^3$ has a higher temperature range without winds than with winds because the extra stellar luminosity heats that gas. When winds are included, that dense gas is less common in addition to being colder; there is more fragmentation, which turns dense gas into stars. In addition, some of

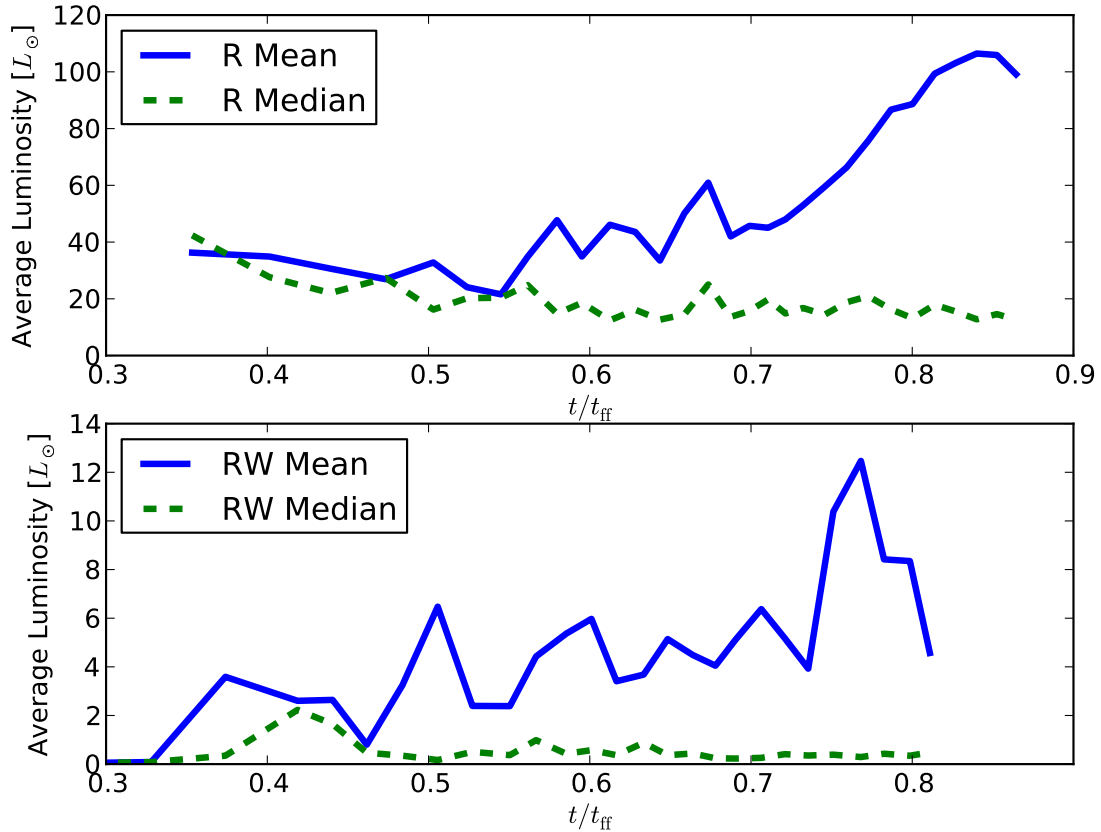


Figure 4.10 Mean and median stellar luminosity versus time for simulations with radiation. The top panel is the simulation without winds and the bottom panel is the simulation with winds.

the gas is also blown away by the winds themselves.

4.4 Discussion

4.4.1 Supporting a Cloud with Outflows

The turbulent evolution shown in Figures 4.4 and 4.5 roughly agrees with previous simulations of molecular clouds with outflows, such as those in Nakamura & Li (2007). Turbulent energy decays initially, only to be replaced by kinetic energy from winds and from gravity. While these sources can increase the total kinetic energy of gas, the new turbulence is fundamentally different from the isotropic, homogeneous hydrodynamic turbulence it replaces. This result is also seen in Nakamura & Li (2007), who find that the late time turbulent

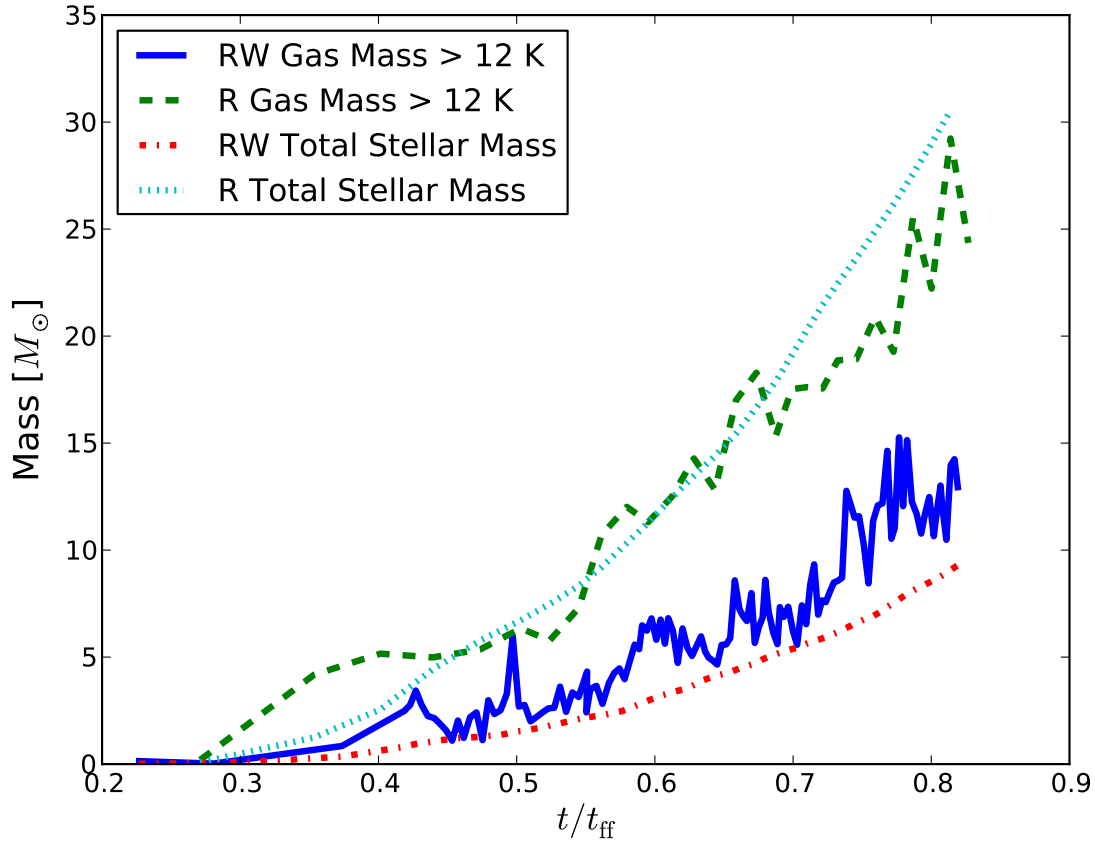


Figure 4.11 Total gas mass heated above 12 K versus time, compared to the background value of 10 K. The total mass in stars is also plotted for reference.

statistics do not match expected isotropic hydrodynamic results. One key difference is the energy from outflows is highly anisotropic. Outflow cavities are marked by long walls with high velocity shear between the fast outflow gas and the slow ambient gas. This shear is detectable as solenoidal energy. There is some compressive energy at the head of the outflow cavity, but most of the surface area is the side walls of the cavity and not the head. The ratio of solenoidal to compressive energy is 2 for isotropic turbulence with the solenoidal driving used here. The evolution of the ratio of solenoidal energy to compressive energy is shown in Figure 4.13. Wind injection greatly increases the solenoidal energy, steadily increasing the solenoidal to compressive ratio over the course of the simulation. This new anisotropic turbulence can behave fundamentally differently from isotropic turbulence (Hansen et al. 2011).

The other major difference between the initial turbulence and wind-driven turbulence is seen in the rms velocity, σ_{dense} , of gas with $\rho > \bar{\rho}$. Even in isotropic, homogenous, hy-

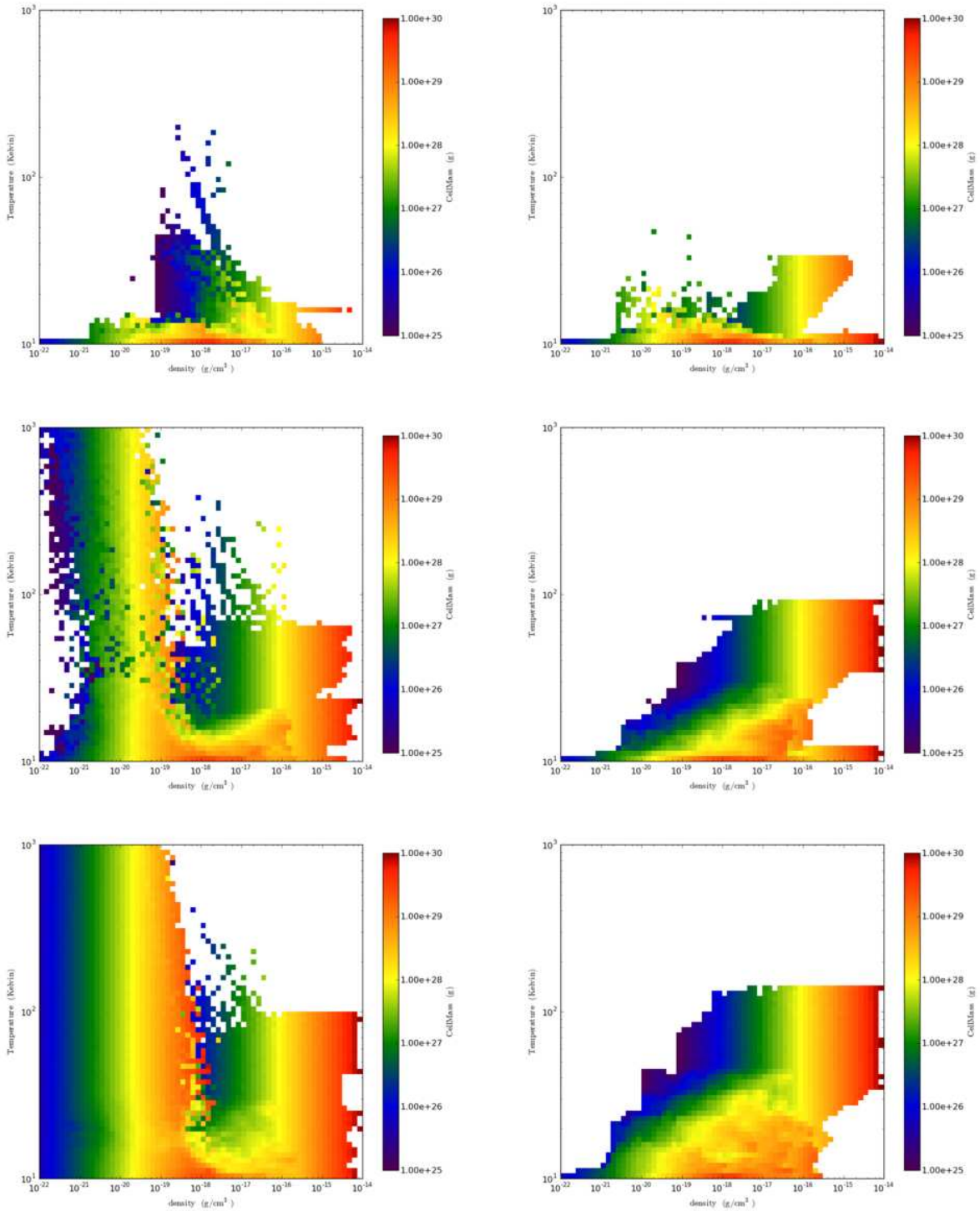


Figure 4.12 Phase plot showing total gas mass as a function of temperature (y-axis) and density (x-axis) for radiative simulations with (left) and without (right) winds. Phase plots are taken at times of 0.25 , 0.5 and $0.75 t_{\text{ff}}$ from top to bottom. The high-temperature low-density gas on the left part of the wind phase plots is outflow gas. Warm, high-density gas is near gas near a luminous star.

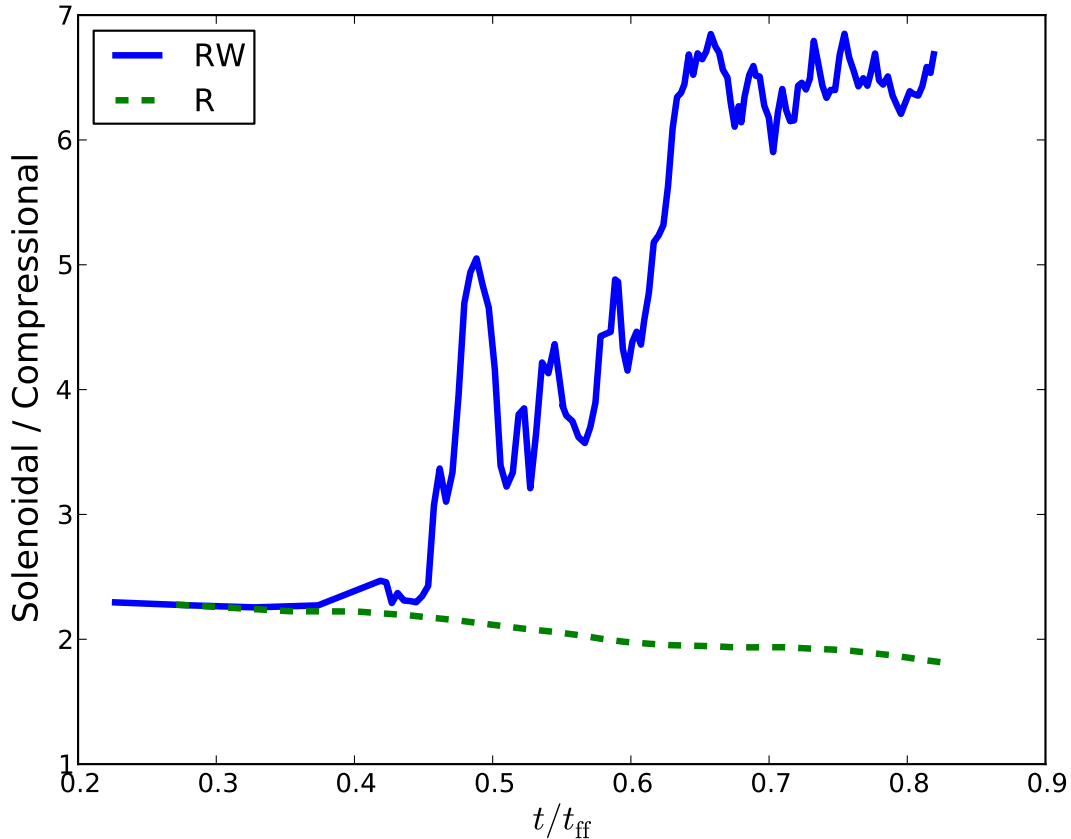


Figure 4.13 Ratio of solenoidal to compressive energy versus time with and without winds for the radiative simulations. For pure hydrodynamic, isotropic turbulence, this ratio should be around 2. This ratio stays near 2 when winds are excluded. When winds are included, the turbulence is much more anisotropic, leading to higher solenoidal fractions.

drodynamic turbulence, there is a negative correlation between density and velocity, causing $\sigma_{\text{dense}} < \sigma_v$ (Offner et al. 2009a). The winds themselves are collimated, very low density gas and have difficulty transmitting energy into high density gas. This means that while σ_v is much greater with winds than without, σ_{dense} does not change much when winds are included. The evolution of σ_{dense} compared to σ_v is shown in Figure 4.14.

Because the dense gas is relatively unaffected by the outflows, if our cloud had been centrally concentrated like that of Nakamura & Li (2007) or Wang et al. (2010), the dense part of the cloud would have most likely collapsed on itself even with the support of protostellar outflows. Magnetic fields may have an effect, as shown by Wang et al. (2010). The magnetic fields help transmit outflow energy to a much larger solid angle, so that even a centrally concentrated cloud can achieve a quasi-static balance between outflows and gravity.

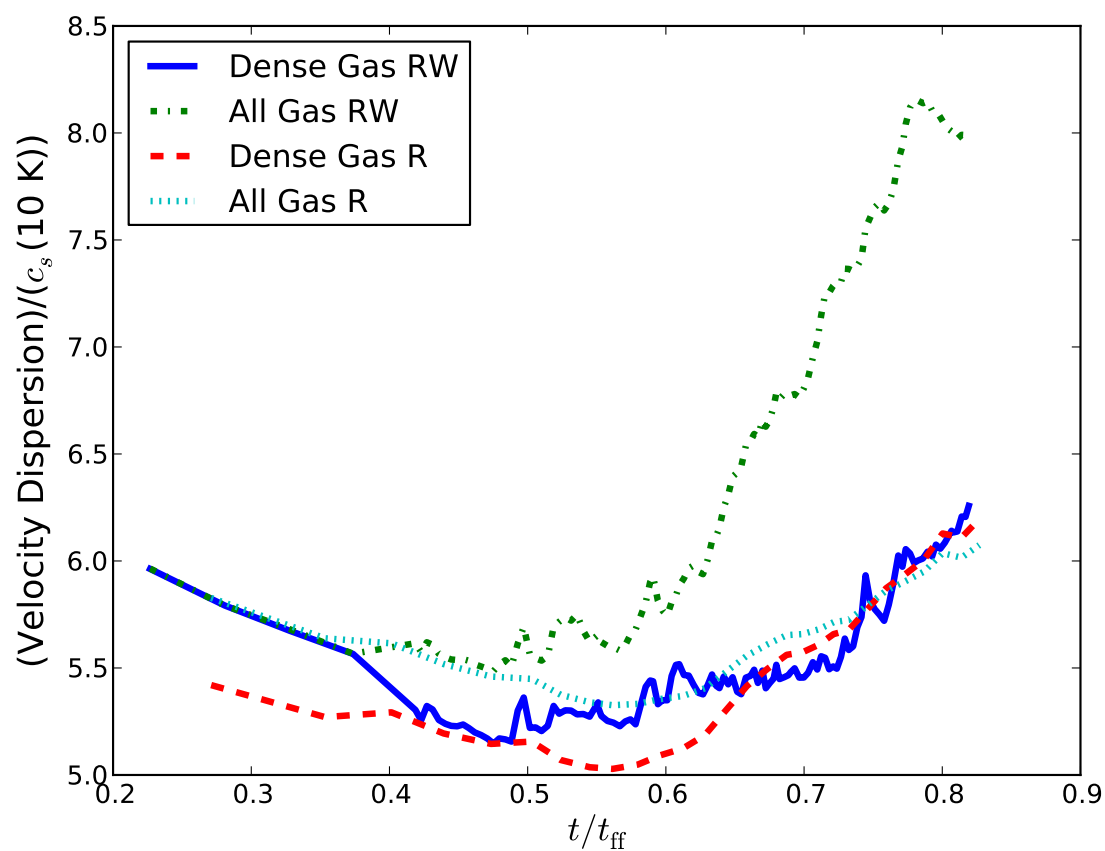


Figure 4.14 Time evolution of rms Mach number of dense gas and all gas with and without winds. Winds significantly raise the Mach number of the light gas, but do not strongly influence the dense gas turbulence.

4.4.2 Comparison to the IMF

Our resolution of 32 AU is marginally good enough to capture binaries, so each star particle should represent a single stellar object instead of a stellar system. At any given time, about 2/3 of our star particles are in stellar multiples. The multiple properties are dynamic due to unstable high-order multiples and we cannot compare to the observed system properties. We can, however, compare to observed stellar properties. The protostellar mass functions of the four main simulations are shown in Figure 4.15 and compared to the stellar IMF in Chabrier (2005). The mass functions in Figure 4.15 are shown at the latest

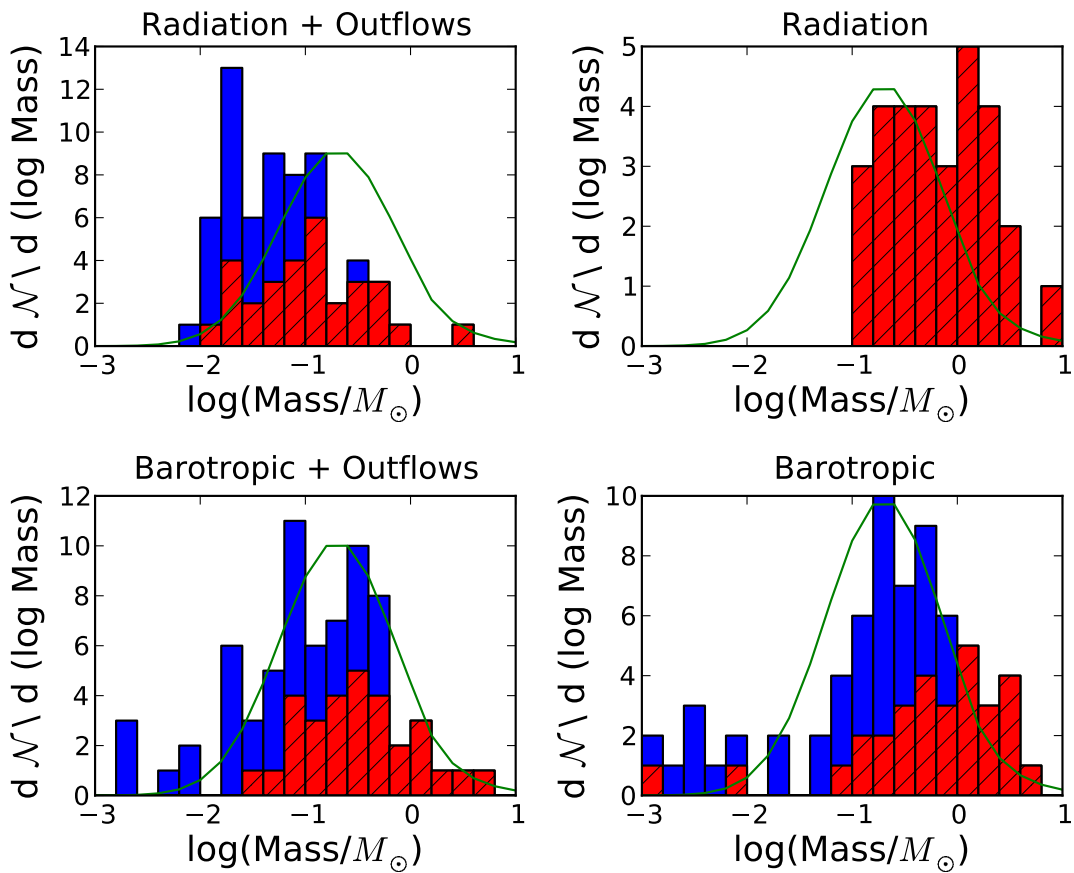


Figure 4.15 The mass function of all stars in each simulation are shown in blue histograms. The mass function of the first 30 stars to form are overplotted in red hatched histograms. The stellar IMF is plotted as the green line. Top left: RW at $t = 0.83t_{\text{ff}}$. Top right: R at $t = 0.83t_{\text{ff}}$. Bottom left: BW at $t = 1.09t_{\text{ff}}$. Bottom right: B at $t = 1.03t_{\text{ff}}$

time available for each simulation. This time is later for the barotropic simulations due to the computational expense of flux-limited diffusion with many stellar sources. The mass

functions in Figure 4.15 are not exactly comparable to an IMF because some of the stars are still accreting. These protostellar mass functions can be compared to those in McKee & Offner (2010), where the turbulent core and competitive accretion models both roughly match RW. To help approximate an IMF, we have also plotted the mass function of the first 30 stars to form, which is the number of stars that form in the R simulation. Roughly speaking, the last stars to form are all due to small-scale fragmentation at later times and are less likely to be at their final mass. Even the first 30 stars are not at their final mass when the radiative simulations stop.

As expected, the simulations without winds have mass functions skewed to higher masses than those with winds. The mass functions of both simulations without winds have too much mass at the high end compared to the IMF. The best fit to the IMF is from the BW simulation. It has a deficit at high mass when all particles are considered and a surplus when the first 30 particles are considered. It should be noted that the normalized mass functions for BW and RW look nearly identical when compared at the same time (explored in the next section). It is a good assumption that RW would also eventually match Chabrier at $t \sim t_{\text{ff}}$. Even at $t = 0.83t_{\text{ff}}$, the first 30 stars have only a small deficit at high mass compared to Chabrier.

4.4.3 Comparison to Protostellar Luminosities

Theoretical predictions of protostellar luminosities are often too high compared to observations of regions of low-mass star formation (Kenyon et al. 1990; Young & Evans 2005; Enoch et al. 2009), so it is important to compare our own simulations with observations. The mean and median luminosities of protostars observed in nearby clusters are $\langle L_{\text{obs}} \rangle = 5.3_{-1.9}^{+2.6} L_{\odot}$ and $L_{\text{obs,med}} = 1.5_{-0.4}^{+0.7} L_{\odot}$, respectively (Enoch et al. 2009; Evans et al. 2009; Offner & McKee 2011). The typical mean and median luminosity in our simulation with winds are $\langle L \rangle = 6.9 L_{\odot}$ and $L_{\text{med}} = 1.4 L_{\odot}$, in agreement with the observations. An additional useful quantity is the standard deviation of the luminosity, $\sigma(L)$. This is sensitive to outliers in the luminosity distribution, but this can be mitigated by using the log of the luminosity. We find $\sigma(\log L) = 0.77$ dex. This matches the observed value $\sigma(\log L_{\text{obs}}) = 0.7_{-0.1}^{+0.2}$. For these comparisons, we have discarded stars with $L < 0.05 L_{\odot}$, below the detection limit of the observations.

One theoretical prediction that also matches the observed protostellar luminosities is the work of McKee & Offner (2010) and Offner & McKee (2011). This prediction differs from the straightforward, constant accretion rate prediction (Fletcher & Stahler 1994a,b) in three important ways. First, Offner & McKee (2011) assumed that 1/4 of the energy of the gas that accreted onto the star was removed non-radiatively. This effect is captured in our simulations. Second, they considered various accretion rates that rise over time, such as predicted in core accretion and competitive accretion. These accretion rates all take the form,

$$\dot{m} = \dot{m}_1 \left(\frac{m}{m_f} \right)^j m_f^{j_f}, \quad (4.20)$$

where m is the instantaneous mass of a protostar, m_f is the final mass of a protostar, and \dot{m}_1 is a constant throughout a cloud. More realistic accretion rates will rise at early times and slowly decline over time, in what McKee & Offner (2010) call ‘tapered accretion’. There are multiple approaches to this; the one taken by McKee & Offner (2010) is to assume a linear decrease in the accretion rate with time, $\dot{m} \propto 1 - t/t_f$, which implies that

$$\dot{m} = \dot{m}_1 \left(\frac{m}{m_f} \right)^j m_f^{j_f} \left[1 - \left(\frac{m}{m_f} \right)^{1-j} \right]^{1/2}. \quad (4.21)$$

The values of j and j_f for several different accretion theories are shown in table 4.2 as well as the values measured in our simulations with winds. Radiative and barotropic simulations produce the same j and j_f . The fits shown are for equation (4.21). Our data do not agree with the functional form for untapered accretion (equation (4.20)), but if this were used, j_f would remain the same while $j \sim -0.1$. Our measured values of $j = 0.3 \pm 0.2$

Accretion Mechanism	j	j_f
Constant Accretion	0	0
Turbulent Core Accretion	0.5	0.75
Competitive Accretion	0.67	1
Simulations with Winds	0.3 ± 0.2	0.6 ± 0.2

Table 4.2 Accretion rate dependencies on instantaneous and final protostellar mass

and $j_f = 0.6 \pm 0.2$ marginally agree with the turbulent core accretion model, but do not match any of the other theories. Our j and j_f actually lie in between constant accretion and turbulent core accretion. This suggests the most appropriate theory may be the two component turbulent core (2CTC) model, which is constant accretion at early times and turbulent core accretion at later times. Our low j does not agree with Bondi-Hoyle accretion, which accelerates with mass.

The last effect considered by McKee & Offner (2010) and Offner & McKee (2011) (as well as Dunham et al. (2010)) is episodic accretion from FU Ori type protostars (e.g. Hartmann & Kenyon 1996). If protostars spend most of their life in a low-accretion, low-luminosity phase and accrete nearly all their mass during short intense accretion bursts, the median stellar luminosity can be greatly reduced. This episodic accretion is thought to arise from disk instabilities (Basu & Vorobyov 2005). We do not resolve disks and therefore do not see episodic accretion in our simulations.

4.4.4 Preventing Fragmentation with Radiative Feedback

Fragmentation in the simulations happens in two distinct phases. First, the cloud as a whole forms cores of size $\sim 20,000$ AU (0.1 pc). This size scale is half the Jeans length at density $\bar{\rho}$. These large scale cores each have a major filament within them that is above the

critical line density for stability (Larson 1985; Inutsuka & Miyama 1992, 1997),

$$\lambda_{\text{crit}} = \frac{2kT}{\mu m_H G}. \quad (4.22)$$

At our temperature, $T = 10$ K, the critical line density is $\lambda_{\text{crit}} = 1.0 \times 10^{16}$ g cm⁻¹. The line densities of the filaments in our cores range from 1.7×10^{16} to 4.0×10^{16} g cm⁻¹, similar to filament line densities seen in Serpens (André et al. 2010). The general morphology is similar to the hub-filament structure in Myers (2009, 2011) with the hub at the center of each core.

The large scale fragmentation is not affected by radiation. There is simply not enough protostellar luminosity to affect the large scales except possibly at late times in the R simulation. The winds do travel through the entire simulation domain and could theoretically affect the fragmentation, but this does not happen in practice since the winds do not couple well to the cores.

The second stage of fragmentation occurs as the filament in each core contracts under self-gravity. The filaments can then fragment into many stars around the central stellar system. Unlike the large-scale core formation, this small scale fragmentation can be significantly suppressed by radiation (Krumholz et al. 2007a; Offner et al. 2009b). This is best demonstrated in Figure 4.7. Simulation R stagnates at 30 stars, while B and BW finish with 80 stars. At the end of R, the total protostellar luminosity is $2500 L_{\odot}$ and this is currently heating $30 M_{\odot}$ of gas. Winds by themselves do not affect small scale fragmentation. The total number of fragments, and therefore the total number of stars, are the same in the barotropic simulations with and without winds, as shown in Figure 4.7. It should be noted that our fragments occur in the core and not in accretion disks. This agrees with higher resolution core evolution simulations (Offner et al. 2010).

When winds and radiation are combined, the winds have a significant indirect effect. The winds lower the mass and accretion rate of the protostars, which lowers the luminosity as seen in Figure 4.9. This means that the fragmentation suppression seen in comparing R to B should be reduced when comparing RW to BW. To investigate this in more detail, we have shown the mass functions of RW and BW, both at $t = 0.83t_{\text{ff}}$, in Figure 4.16. For purposes of comparison, we have excluded stars with mass $M < 0.05M_{\odot}$, since these stars are usually short lived and possibly subject to details of numerical sink particle formation or merging. The two mass functions are nearly the same. A two sample Kolmogorov-Smirnov test gives a 50% chance that both samples are drawn from the same underlying function. The primary difference between the two mass functions lies in the heaviest star in the simulation. The core that forms the heaviest star fragments early in BW, turning a star that is $2.8 M_{\odot}$ in RW into a $2.0 M_{\odot}$ star in BW with two extra $M \sim 0.4M_{\odot}$ stars. The reduced fragmentation in RW for that star might be expected from radiative feedback, since that is the most luminous star in the simulation.

To understand why radiation does not drastically change the picture for most stars, consider the Jeans mass for internally heated gas. The Jeans mass, M_J , and Jeans length, λ_J , are normally functions of density and temperature, but when there are protostars, the

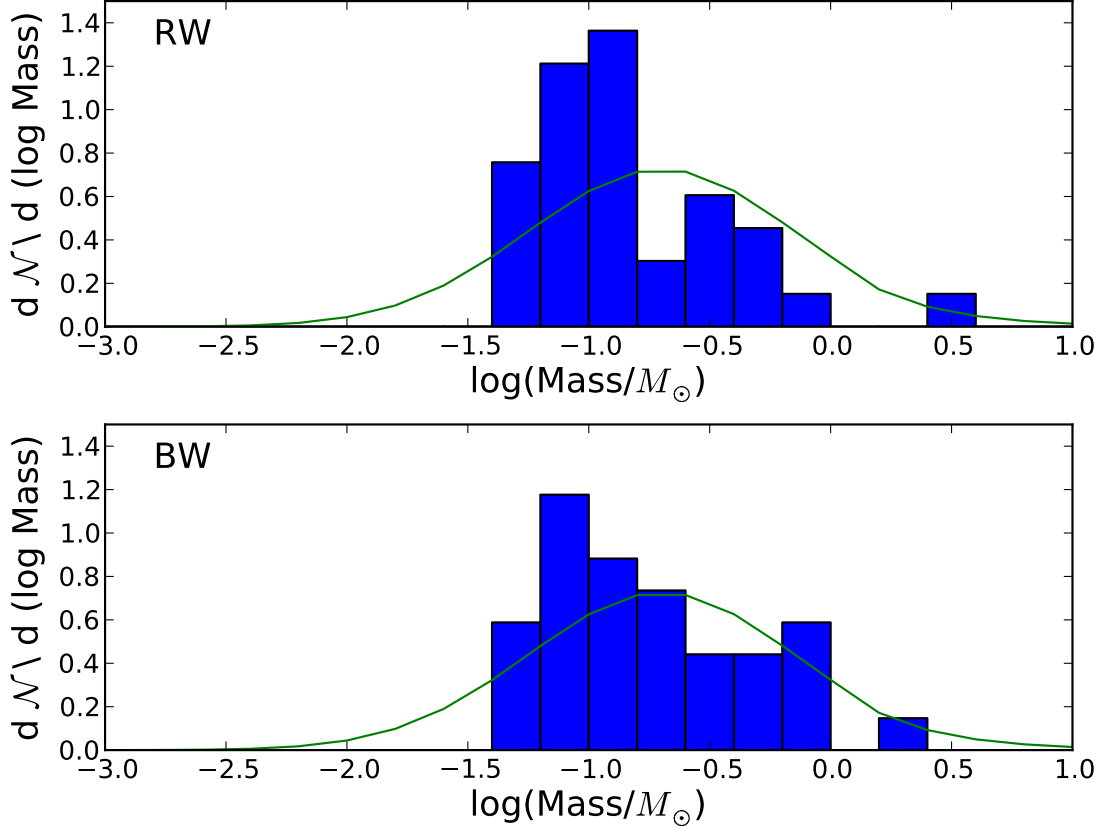


Figure 4.16 Mass function for all stars with mass $> 0.05M_{\odot}$ for simulations RW (top) and BW (bottom) with the Chabrier IMF also plotted. The two mass functions are similar. The main difference comes from the largest star in RW fragmenting more in BW, lowering the largest mass and adding more stars around $0.5M_{\odot}$.

temperature is no longer a constant and is described by $L = 4\pi\sigma r^2 T^4$ where σ is the Stephan-Boltzman constant and r is the distance to a protostar. If the T dependence in λ_J is replaced by

$$T^4 = \frac{L}{4\pi\sigma\lambda_J^2}, \quad (4.23)$$

a new Jeans length and Jeans mass can be found. This new Jeans mass, derived in Bate (2009), is

$$M_{\text{eff}} \approx 0.5 \left(\frac{\rho}{10^{-19} \text{g cm}^{-3}} \right)^{-1/5} \left(\frac{L}{150L_{\odot}} \right)^{3/10} M_{\odot}. \quad (4.24)$$

This M_{eff} has a weak dependence on ρ and L . This weak dependence is appealing because one can pick fiducial values of density and luminosity and the fiducial mass from those

values does not depend strongly on your assumptions. For a density typical of observed cores $\rho = 10^{-19} \text{ g cm}^{-3}$ and a luminosity of $L = 150 L_{\odot}$, the fiducial mass is $0.5 M_{\odot}$. This suggests that radiative feedback prevents fragmentation below $0.5 M_{\odot}$. Bate (2009) used $L = 150 L_{\odot}$, which is very large for regions of low-mass star formation. If we use the median luminosity of $1.5 L_{\odot}$ observed in Enoch et al. (2009), M_{eff} moves to $0.12 M_{\odot}$. When protostellar outflows are allowed to reduce mass by a factor of 3, M_{eff} is now only $0.04 M_{\odot}$. This is well below the characteristic mass of the IMF ($0.2 M_{\odot}$) and even below our criteria for merger suppression due to second collapse ($0.05 M_{\odot}$).

Even though $0.04 M_{\odot}$ is much less than the characteristic mass of the IMF, it is notably higher than the Jeans mass from dust self-opacity, $0.004 M_{\odot}$. This means that the protostellar radiation will raise the smallest expected fragment mass by a factor of ten. Simulations that do not include radiation will continue to fragment down to either $0.004 M_{\odot}$ or the resolution limit, while radiative simulations will fragment at scales more agreeable with observations. In addition, as star formation progresses in a cloud, there will be stars with luminosities comparable to $150 L_{\odot}$, which will effectively reduce fragmentation. At late times in star formation, fragmentation may be suppressed in the entire cloud (Krumholz et al. 2011). Fragmentation suppression by radiation is even more important in the presence of high-mass stars, which do not rely on accretion luminosity (Krumholz et al. 2007a; Cunningham et al. 2011).

4.4.5 Fragmentation in Rho Ophiuchus

Our cloud fragments around the Jeans length (0.2 pc), but then continues to fragment below this point. Fragmentation at the Jeans length is common observationally (Blitz & Williams 1997; Enoch et al. 2008). In instances where observers have the resolution and sensitivity to resolve fragmentation at scales below the Jeans length, however, even more fragmentation is found at those scales (Motte et al. 1998; Johnstone et al. 2000; Teixeira et al. 2007; Chen & Arce 2010; Bontemps et al. 2010). Fragmentation can be quantified as a function of scale, r . Given a set of clump locations in a cloud, one can calculate a set of clump pair separations. Let the differential number of pairs separated by distance r be $dN_{\text{pair}} = H(r) d \ln r$. The number of clump pair separations for randomly distributed clumps is $H_{\text{ran}}(r)$. The two point correlation function, w can be calculated from these quantities (Johnstone et al. 2000),

$$w(r) = \frac{H(r)}{H_{\text{ran}}(r)} - 1. \quad (4.25)$$

The two-point correlation function has been measured for the central parsec of ρ Ophiuchus by Johnstone et al. (2000). In this measurement, excess fragmentation ($w > 0$) is found below $r \sim 3 \times 10^4 \text{ AU}$, similar to the Jeans length of the cloud. There is a power law fit, $w(r) \propto r^{-0.75}$, in this regime. Larson (1995) also measured clustering of stars in Taurus and found a power law fit with a break at 8000 AU . The separation between stars has had time to evolve since the initial fragmentation, so we narrow our focus to comparisons with Johnstone et al. (2000).

To compare our simulations to the observed w , we first created optically thin column density maps of our simulations and convolved them with a Gaussian with a FWHM of 1600 AU. The resolution was chosen to be similar to that from Johnstone et al. (2000). We used the Clumpfind algorithm from Williams et al. (1994) on the convolved column density map to obtain a list of clumps and their positions. To investigate the possibility of time evolution of w , this is performed at an early time in the simulation and then again at a late time, $t \sim 0.4t_{\text{ff}}$ and $t \sim 0.75t_{\text{ff}}$, respectively. The results are shown in figure 4.17. As expected,

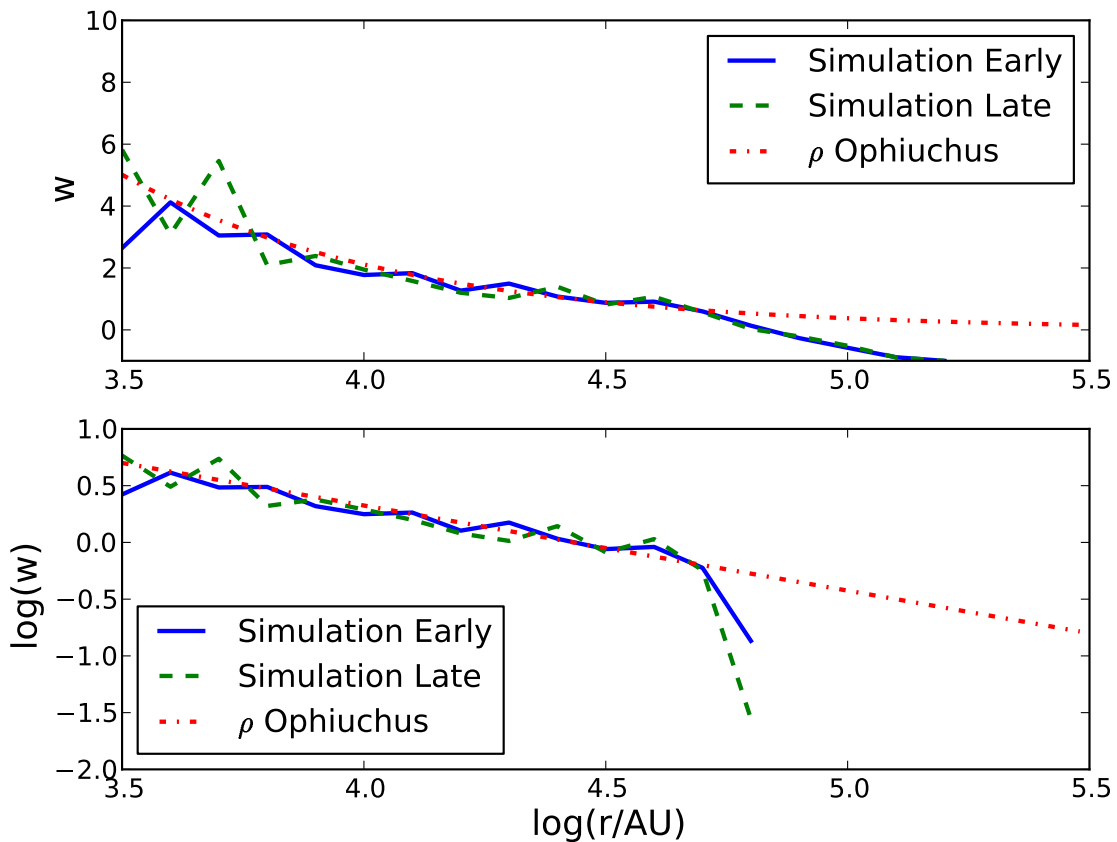


Figure 4.17 Two point correlation function, w , for clumps in simulation RW convolved with a 1600 AU Gaussian beam. The correlation function is calculated at an early time, $t \sim 0.4t_{\text{ff}}$ and a late time, $t \sim 0.75t_{\text{ff}}$. The correlation is similar at early and late times, except for the smallest scales, where fragmentation increases over time. For comparison, the fit to $r < 3 \times 10^4$ AU measurements from ρ Ophiuchus is also included.

the correlation function drops off above $r \sim 4 \times 10^4$ AU, about 2/3 the Jeans length at $\bar{\rho}$ for our simulation. More remarkably, the correlation function in our simulation matches that measured in ρ Ophiuchus quite well at all scales below this drop off. The early and late time

simulations also generally agree with each other, suggesting there is not much time evolution in w . There is a discrepancy between the two times at $r \sim 5 \times 10^3$ AU. At these small scales, fragmentation does increase in time, as high density regions have more time to form and fragment. This is a possible explanation for the non-detection of small scale structure in Perseus (Schnee et al. 2010).

It should be noted that at $t \sim 0.4t_{\text{ff}}$, our stars have not provided very much feedback, and the simulation can be considered solely gravito-hydrodynamic. Simulations with just hydrodynamics and gravity are scale-free. The exact match with ρ Ophiuchus is partially due to our choice of cloud parameters to mimic ρ Ophiuchus. The scale free results are the break in $w(r)$ at the Jeans length the $w(r) \propto r^{-0.75}$ functional form.

4.4.6 Observed Core Mass Functions

There is a wealth of observations cataloguing masses of cores in star-forming regions (Motte et al. 1998; Testi & Sargent 1998; Johnstone et al. 2000, 2001; Motte et al. 2001; Beuther & Schilke 2004; Stanke et al. 2006; Alves et al. 2007; Enoch et al. 2008; Sadavoy et al. 2010). Most of these observations are unable to resolve the small scale fragmentation seen in ρ Ophiuchus, but still provide valuable information. Any simulation of fragmentation leading to star formation must be able to recreate these observations. To recreate the observations, we produced optically thin column density maps of our simulations in all three directions and convolved them with Gaussian beams chosen to match the observations. We then applied Clumpfind to the convolved column density, similar to our comparison to ρ Ophiuchus.

The observations have a wide range of beam sizes due to the range in distances to star-forming regions, so we also used a range of beam sizes for comparison. We find that the CMF derived from our simulated observations is highly sensitive to the beam size used. As the beam size increases, the smallest cores are no longer detectable and drop out of the CMF. In addition, tight clusters of cores become unresolved and look like new, much larger cores. Both effects increase the median clump mass. The effect of overlapping cores is explored further in Kainulainen et al. (2009b). This sensitivity of the CMF to resolution is seen also in the observations, and shown in Figure 4.18. To gather the median mass of a range of CMFs, we used the data tabulated in Reid & Wilson (2006). All cores from Reid & Wilson (2006) are detected using Clumpfind. To supplement that data, we also used the three clouds (Serpens, Perseus and ρ Ophiuchus) from Enoch et al. (2008). Enoch et al. (2008) do not rely solely on Clumpfind, but use a method that returns similar results for them. Clumpfind has many limitations (Pineda et al. 2009; Goodman et al. 2009), but is still useful for the purposes of comparison. When compared to these observational data, our simulated CMFs match quite well. The simulated CMF with 3200 AU and 6400 AU beams are interesting in particular, as this is the usual range of telescope beams for nearby clouds. The extent of our simulation domain (130,000 AU) prevents useful comparisons to more distant observations. In addition, our base grid resolution, 512 AU, limits observations of cores at small beam sizes. Physically meaningful cores will trigger adaptive refinement and can go to smaller scales, but smaller, ephemeral, observed cores are lost. This means the simulated median

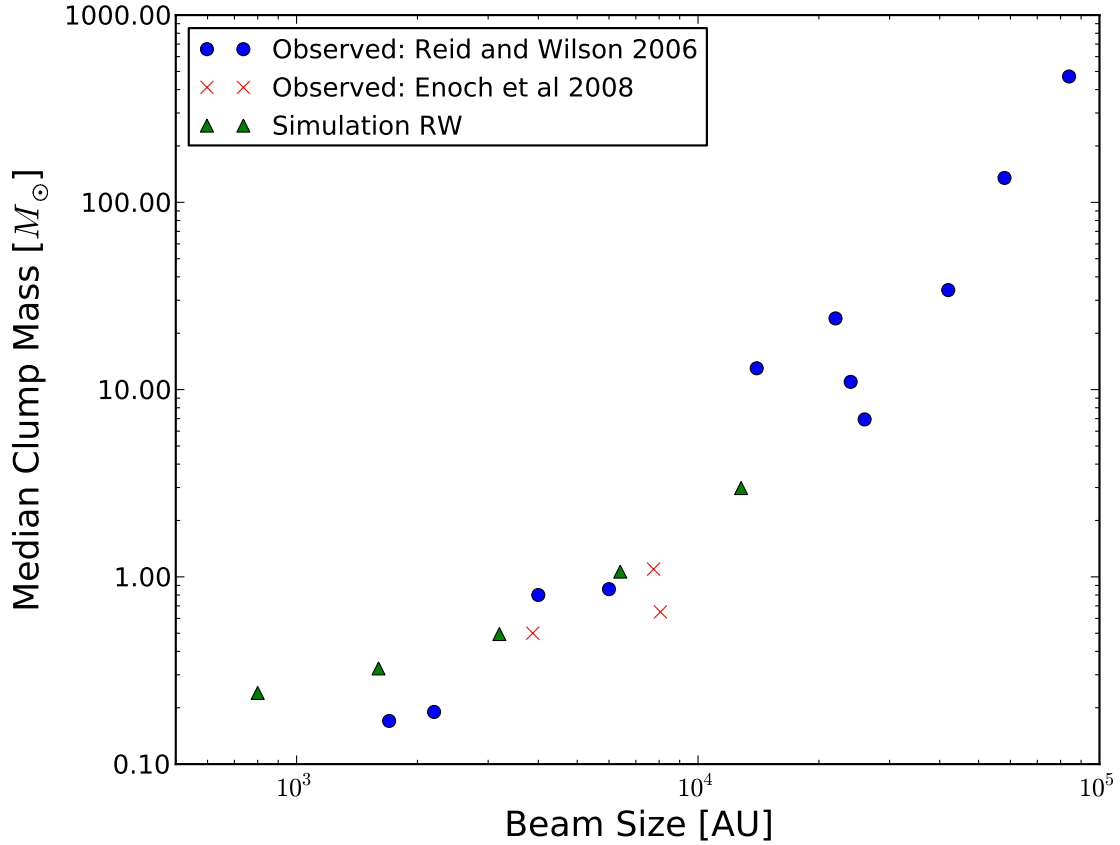


Figure 4.18 Median mass of the CMF found in a cloud as a function of resolution of the observation. The CMFs from synthetic observations of RW are green triangles. For comparison, CMFs tabulated in Reid & Wilson (2006) are included as well as 3 CMFs from Enoch et al. (2008). The two lowest points from Reid & Wilson (2006) are ρ Ophiuchus at different wavelengths.

masses at 800 AU and 1600 AU are too high. This is most apparent when comparing to the observations of ρ Ophiuchus with beam sizes 1600 AU.

Figure 4.18 does not include the CMF from the Pipe Nebula (Alves et al. 2007). The resolution is comparable to the best observations of ρ Ophiuchus, but the median mass is near $1 M_{\odot}$. This makes it stand apart from the other observations. This region is low density and not actively forming stars. In addition, the observed cores are largely unbound (Lada et al. 2008). The Pipe Nebula should perhaps be considered a pre-star-forming region, closer in nature to the Polaris Flare than to Serpens or ρ Ophiuchus. These pre-star-forming regions have much higher Jeans lengths and masses and have fundamentally different column density distribution functions (Kainulainen et al. 2009a).

4.4.7 CMF to IMF relation

Given that we have identified clumps at the beginning of star formation and have stars at the end of the simulation, a natural question is how the initial clumps relate to the final stars. For this question, it is best to use stars from B. This excludes winds, which remove mass from clumps. This also excludes radiation, which suppresses fragmentation and can effectively merge smaller clumps onto large clumps with luminous stars. The initial CMF and the final IMF for B are shown in Figure 4.19. For proper comparison, the mass functions are not normalized, and total counts at each mass are shown. To avoid triple counting cores in CMF, the synthetic observations are taken in only one line-of-sight direction instead of all three. Otherwise these CMFs are the same as those in previous sections. When focusing

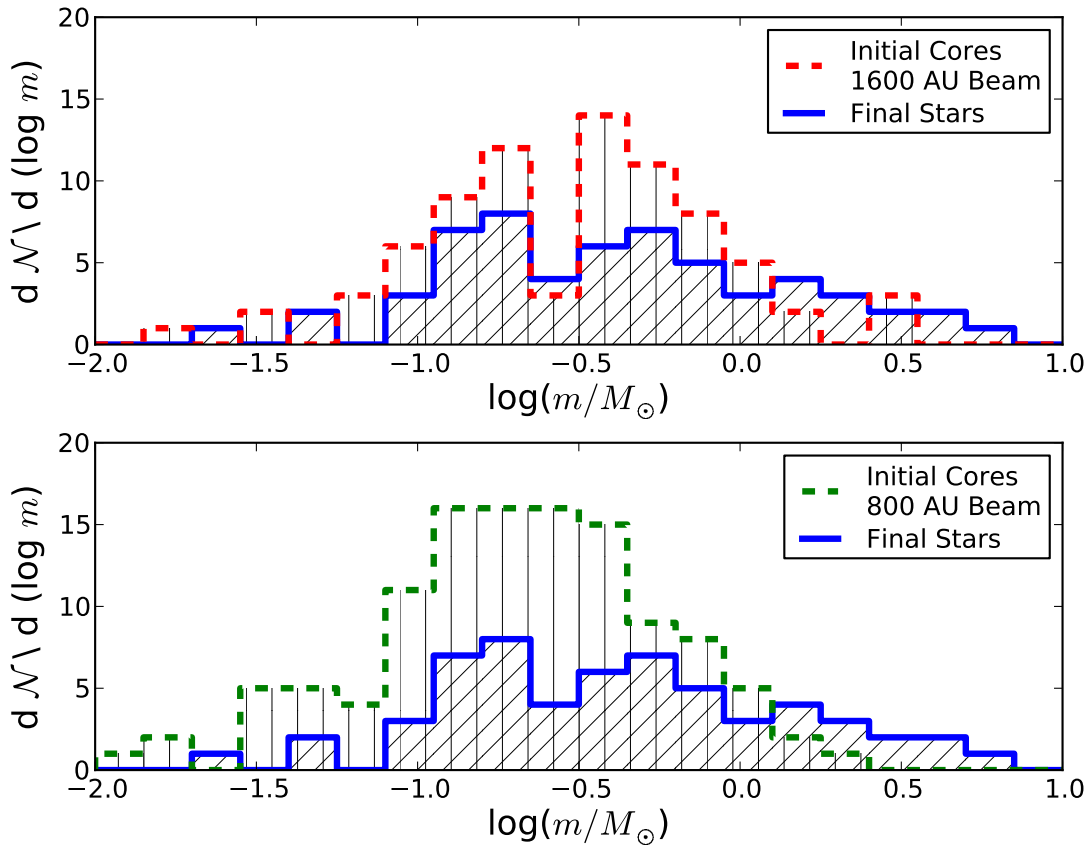


Figure 4.19 Mass functions for both the initial cores found using clumpfind and the final masses in stars. The y axis represents total counts and is not normalized. Top panel: cores found using a 1600 AU beam size. Bottom panel: cores found using an 800 AU beam size.

on the CMF found with the 1600 AU beam size, the initial CMF and final IMF are well

correlated. The typical mass and total number of objects match well between cores and stars. There are more stars with masses above $1 M_{\odot}$ than cores, but this can be explained by merging cores. There are too many lower mass cores, so merging cores would also address this. Unfortunately, this comparison only holds for the 1600 AU beam size. The CMF is highly sensitive to beam size, as shown in Figure 4.18. When a slightly smaller, 800 AU, beam size is used, the clumps are too small and too numerous to all correlate with stars.

All of this demonstrates that cores observed in star-forming regions may not predict the stellar outcome of that region. We do not need to limit ourselves to synthetic observations of our simulations and can identify cores from the full 6 dimensional phase space. This is done using the ‘find_clumps’ routine in the yt analysis toolkit (Turk et al. 2011). The algorithm is described in more detail in Smith et al. (2009). It uses density contours to return a hierarchy of clumps, where each clump can contain smaller child clumps. Our simulations have hundreds of local maxima in density large enough to be considered clumps. At $t = 0.3t_{\text{ff}}$, only 40 of these are bound, defined as $|\text{potential energy}| > (\text{thermal energy} + \text{kinetic energy})$. We will only consider the bound clumps in this analysis. The bound clumps cover a large range of sizes with the largest clump filling almost the entire box ($181 M_{\odot}$). This clump contains five child clumps. Each of these clumps contain children and grandchildren down to masses of $10^{-4} M_{\odot}$. When comparing to the IMF, one should ignore clumps with multiple child clumps, and count the children instead. Throwing out clumps with masses less than $0.05 M_{\odot}$, there are only 5 bound childless clumps at $t = 0.3t_{\text{ff}}$, for a total mass of $2.5 M_{\odot}$. At $t = 0.4t_{\text{ff}}$, some of the parent clumps split into more children, resulting in 16 bound childless clumps, though the total mass is largely unchanged, at $2.6 M_{\odot}$. These clumps are notably smaller than the primary turbulent cores described in §3.1 and will be called ‘sub-cores’. These sub-cores lead to the burst of star formation at $t = 0.5t_{\text{ff}}$ and their mass function is shown in Figure 4.20. The median mass of these sub-cores is $0.13 M_{\odot}$. Even if each sub-core forms exactly 1 star, they do not explain the stellar mass function of the simulation, which eventually has a median mass of $0.3 M_{\odot}$ when winds and radiation are not included. This discrepancy can be explained by the 20,000 AU turbulent cores. These objects are bound, but they cannot be detected with density contours due to their supersonic turbulence. Each core has multiple pockets of high density gas. When using density contours, you see many smaller unrelated, unbound clumps instead of a few larger bound clumps that correspond to the physical cores. The cores are visible by eye and should be identifiable with a more advanced density search. We identify them by stellar clustering. The central stellar systems (usually binary systems) in these cores are all much more massive than the sub-cores. If these central stellar systems are ignored, the median mass of stars moves from $0.3 M_{\odot}$ to $0.16 M_{\odot}$, much closer to the median sub-core mass. The median mass of non-central stars for the case with winds is $0.07 M_{\odot}$. The turbulent core and central star properties are summarized in table 4.3. The cores are bound at late times even when only the stars are considered, with the kinetic energy in stars approximately half the potential energy of stars in each core. In addition, the core-to-core velocity dispersion is typically 0.4-0.5 km/s. This is notably lower than the cloud velocity dispersion, which starts at 1.2 km/s. There is a strong anti-correlation between velocity and density, as the densest gas occurs at stagnation

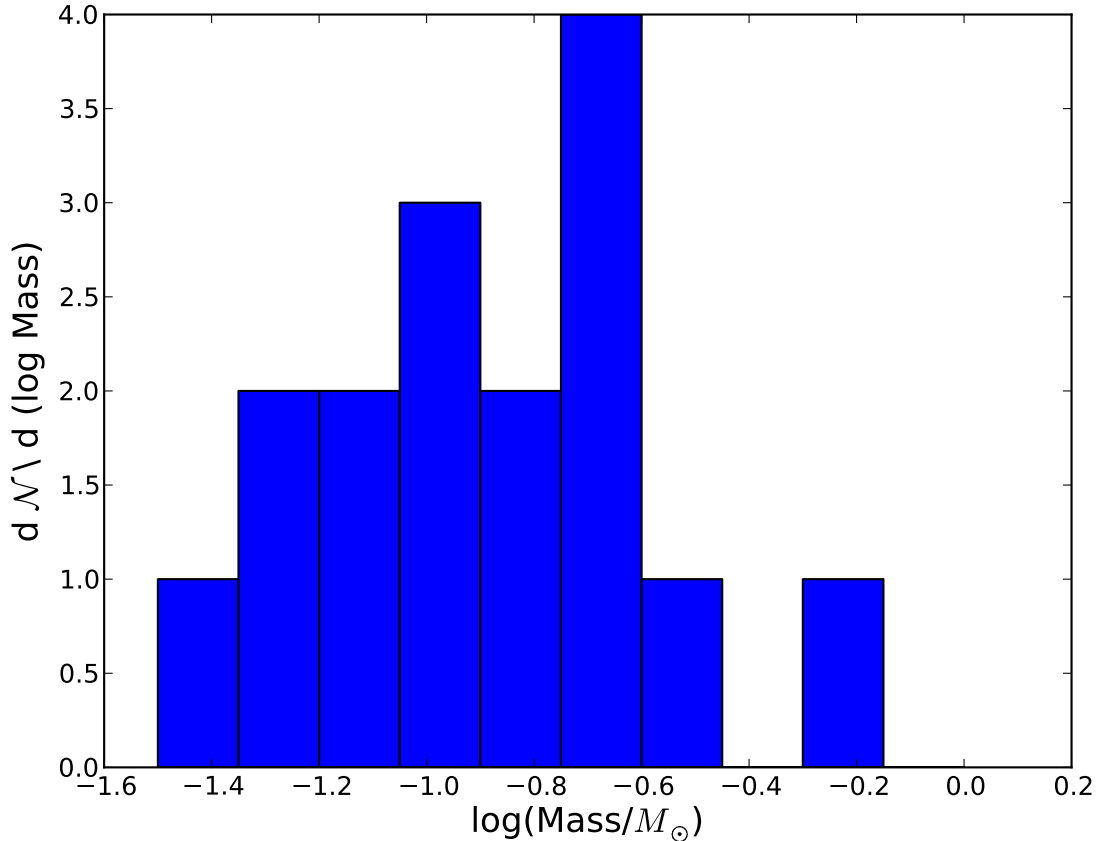


Figure 4.20 Histogram of masses of bound childless sub-cores at $t = 0.4t_{\text{ff}}$.

points in a turbulent flow. This means that the core-to-core velocity dispersion will naturally be much lower than the gas (Offner et al. 2009a).

Once the cores have formed, each core is carved out by the outflows of its own protostellar system. This yields the core to star efficiency factor, $0.2 < \epsilon_{\text{core}} < 1.0$. The amount of mass lost from a spheroidal core can be calculated from the total momentum output and opening angle of the winds (Matzner & McKee 2000), but the cores in our simulations are more complicated.

The best way to calculate ϵ_{core} is to compare the mass of stars in simulations with and without winds. In the simulations with the barotropic equation of state (B and BW), the total, the mean, and the median mass of stars are all approximately 3:1 comparing the non-wind simulation to the wind simulation at any point in time. This means $\epsilon_{\text{core}} = 1/3$. In the radiative simulations (R and RW), the total mass of stars is also 3:1 comparing the two simulations. The mean and median masses are closer to 10:1, but this is due to fragmentation suppression in simulation R.

	Without Winds			With Winds		
M_{gas} Initial	M_{gas} Final	$M_{*,\text{total}}$	$M_{*,\text{central}}$	M_{gas} Final	$M_{*,\text{total}}$	$M_{*,\text{central}}$
3.4	3.6	5.6	4.7	2.3	1.9	1.3
7.0	3.1	16.8	9.4	2.0	9.6	5.9
3.8	2.5	5.0	3.4	1.2	1.5	1.4
5.0	2.7	5.1	3.9	1.6	2.9	2.2
2.9	-	-	1.0	-	-	0.04
3.3	-	-	2.7	-	-	0.3

Table 4.3 Turbulent Core Properties. The last two cores eventually merge with the largest core, making it impossible to measure the final gas and total stellar properties. The final properties of the largest core are necessarily a sum over the last two cores in addition to the largest core.

4.4.8 Turbulent Core and Competitive Accretion

It is useful to place the stellar accretion in our simulations in the context of existing star formation models. Two popular models currently are turbulent core and competitive accretion. In the turbulent core model, (Padoan & Nordlund 2002; McKee & Tan 2003; Padoan et al. 2007; Hennebelle & Chabrier 2008, 2009), supersonic turbulence in molecular clouds creates many cores. Each bound core then collapses into a single stellar system. In this scenario, the mass from each star is accreted almost entirely from its natal core. In the competitive accretion model (Zinnecker 1982; Bonnell et al. 1997, 2001; Bate & Bonnell 2005; Bonnell et al. 2006), the bound cores are $\sim 0.1 M_{\odot}$. The molecular cloud undergoes a global collapse and all stars accrete from the entire cloud. Protostars exhaust their cores at low-masses and then grow by Bondi-Hoyle accretion. The protostars compete with each other for mass from the host cloud and the dynamics of this competition lead to the IMF. Roughly speaking, the virial parameter of the cloud decides which model is correct (Krumholz et al. 2005; Bonnell & Bate 2006; Offner et al. 2008). In clouds with sufficiently sub-virial turbulence, global collapse is possible and competitive accretion prevails. In virial clouds, core accretion dominates. Most simulations of star formation start with virialized clouds, but turbulence quickly dissipates and simulations that do not regenerate turbulence become sub-virial and demonstrate competitive accretion. Turbulence can be regenerated by protostellar outflows, HII regions, or a cascade from larger scales; in simulations, the cascade can be generated by large scale driving.

Our simulations largely agree with turbulent core models, while introducing a hierarchical aspect of sub-cores within turbulent cores. We form turbulent cores on the cloud Jeans length and each of those cores forms a central binary or single star with mass roughly equal to the core mass. Even the smaller stars are formed in their own sub-cores and do not accrete from the cloud at large. Our turbulent cores do accrete from the larger cloud (increasing their initial mass by $\sim 75\%$ over the course of the simulations), which was not originally part of the core accretion theory, but recent turbulence simulations suggest turbulent cores

do accrete from their host cloud (Falceta-Gonçalves & Lazarian 2011).

The accretion from the larger cloud onto our cores is possibly caused by the fact that there is no turbulent driving from large scales. Turbulence is regenerated to some extent by protostellar outflows, but this is relatively ineffective in denser gas. Our simulations are then similar to the undriven simulations in Offner et al. (2008), which also show accretion onto cores. The simulations in Offner et al. (2008) with external driving produce cores that do not accrete much from the cloud. If magnetic fields were included in our simulations, the outflows would couple to much more of the gas (Wang et al. 2010), which would move our simulations closer to those with large-scale driving.

4.4.9 The Role of Stellar Mergers

The stellar mass functions in our simulations are influenced by the details of our sink particle merger process. Mergers are necessary because all codes will introduce numerical fragmentation once they can no longer resolve the Jeans length on the finest scale (Truelove et al. 1997). More stringent sink particle conditions can reduce the number of unwanted sink particles (Federrath et al. 2010), but numerical fragmentation is unavoidable. These methods allow the density to build up where sink particles would be, which leads to even more numerical fragmentation. If sink particles are not allowed to merge, these numerical fragments will steal mass from real fragments and masquerade as real stars, artificially lowering the IMF. On the other hand, allowing sink particles to merge has a similar effect on the IMF as suppressing gas fragmentation. If all sink particles that pass near each other are merged together, the particles will consolidate over time. Eventually, all IMFs look similar to the heavy IMF from R, where radiation suppressed most fragmentation. Our decision to only merge pre-second-collapse stars is a physically motivated compromise between the two extremes of no mergers and all mergers.

This fragmentation suppression of mergers is seen comparing the IMFs of RW and BW. The radiative simulation should suppress some fragmentation while the barotropic simulation fragments all the way down to the Jeans mass at the self-opacity limit, $m \sim 0.004M_{\odot}$. Nevertheless, they have the same IMF. The barotropic simulation does fragment much more than the radiative simulation near the resolution limit. This is seen in the total number of sink particles created, where the barotropic simulation creates 7 times more particles than the radiative simulation. These particles are nearly all very small in mass and immediately merged. The net effect of the extra mergers is to suppress fragmentation by combining fragments below the merger radius (128 AU). The two simulations are nearly identical above this scale and therefore produce the same IMF.

Our choice of merger mass ($m_{\text{merge}} = 0.05 M_{\odot}$) is based on calculations of first collapse (Masunaga et al. 1998; Masunaga & Inutsuka 2000), but the correct mass is not certain. In addition, the mass of second collapse should depend on the accretion history of each protostar. To investigate the effect of our mass choice, we repeated RW with a merger mass of $0.01 M_{\odot}$ out to $t = 0.55 t_{\text{ff}}$. At this point in the simulations, the total mass in stars is $2 M_{\odot}$. In the simulation with $m_{\text{merge}} = 0.05 M_{\odot}$, there are 17 total sink particles; whereas

in the simulation with $m_{\text{merge}} = 0.01 M_{\odot}$, there are 30 total sink particles, even though the total mass in particles is the same. Given that the final IMF for $m_{\text{merge}} = 0.05 M_{\odot}$ is at slightly lower masses than the observed IMF, nearly doubling the number of sink particles with $m_{\text{merge}} = 0.01 M_{\odot}$ would skew to masses much lower than observed. This suggests the particles with masses $0.01 M_{\odot} < m < 0.05 M_{\odot}$ should be merged. It is unclear whether these particles are purely numerical (implying they would never have fragmented in the first place with infinite resolution) or whether real star formation involves many mergers of pre-second-collapse cores. If this type of merger is common, it is possible this significantly affects the low-mass part of the IMF and warrant further investigation.

As an additional effect, our stellar merger mass provides a distinct mass scale to the simulations. For most isothermal simulations, there is no mass scale and one is free to arbitrarily scale the mass, M , density, ρ , or temperature T , while maintaining all of the same dimensionless parameters α , \mathcal{M} , and M_J/M . The only restriction is that $MR^{-1}T^{-1} \propto M^{2/3}\rho^{1/3}T^{-1}$ remain constant. Our barotropic simulations are isothermal except for small deviations at the very highest resolved densities. This means we could not scale the to densities more than an order of magnitude higher, but we are free to scale to lower densities and higher masses. When the merger mass is included, m_{merge} also scales with M . Now if we scale the simulation to a higher mass, we are also increasing m_{merge} . There is some uncertainty in m_{merge} , but it would be difficult to justify increasing it much more than our current level. Even increasing m_{merge} by a factor of 2 would bring it to uncomfortably close to the characteristic IMF mass of $0.2 M_{\odot}$. This means the mass scales of our simulation are relatively stationary. When protostellar winds are included, they introduce a new fixed dimensionless number, the Mach number of the winds $\mathcal{M}_{\text{wind}}$. Since the speed of the winds is proportional to the escape velocity from the stellar surface (i.e., $\propto M^{1/2}$ (McKee & Ostriker 2007)), $\mathcal{M}_{\text{wind}}$ sets the quantity M/T . In practice, this is not a very tight constraint because the wind speed itself is quite uncertain (Downes & Cabrit 2007). When radiation is important, the luminosity of each star is set by complicated stellar models that depend on M as well as the accretion history. The time scale, which goes into the accretion rate, is set by t_{ff} and therefore ρ . In addition, the resulting radiation-hydrodynamics depends on the temperature. This uniquely sets M , T , ρ . Even when radiation is not dynamically important, we do match the observed protostellar luminosities and cannot change our masses without jeopardizing the agreement. Using the approximation $L \propto M^2$, our cloud mass is constrained to $165 M_{\odot} < M < 198 M_{\odot}$ before it no longer falls in the error bars of the observed luminosities. Looser constraints are also applied by our general match to the IMF, which sets M and our match to observed fragmentation in ρ Ophiuchus, which sets M/ρ .

4.5 Conclusions

We report the results of several simulations of the formation of a low-mass star-forming cluster, comparable to ρ Ophiuchus. Our simulations achieve 32 AU resolution using adaptive mesh refinement. We also include radiation-hydrodynamics and stellar feedback. The

stellar feedback represents both protostellar radiation and bipolar outflows. To isolate the individual effects of radiation and outflow feedback, we perform a suite of 4 simulations: a base simulation with no feedback, a radiative simulation with no outflows, an outflow simulation with no radiation and a simulation with both outflows and radiation. This is the first simulation of a star-forming cluster with both radiation and protostellar outflows.

The simulation with radiation and outflows matches the observed protostellar luminosities of nearby star-forming regions. Outflows reduce the stellar mass and accretion rate, thereby lowering accretion luminosities. The protostellar luminosity function also depends on the adopted accretion rate and the fraction of FU Ori type high accretion rate events. We find the accretion rate scales with mass as predicted from turbulent core accretion models. We also find only 0.3% of our stars are in high accretion rate events at any given time. These results generally agree with predictions from Offner & McKee (2011).

The simulation with radiation and without outflows confirms the finding of Offner et al. (2009b) and Krumholz et al. (2011) that protostars can heat their host cloud enough to suppress fragmentation. When outflows are included, however, the total luminosity of stars drops by a factor of 10, and radiation is far less effective at suppressing fragmentation. The simulation with radiation and winds has over twice as many stars as the simulation with radiation without winds. When fragmentation is additionally suppressed by merging low-mass stars at 128 AU, radiation has almost no effect on the resulting mass function. Thus, radiation is necessary to capture fragmentation on the order of hundreds of AU, but it does not significantly effect the gas dynamics above those scales. The situation might change at late times, when most of the gas has been converted into stars (Krumholz et al. 2011) or in the presence of high-mass stars, in which nuclear luminosity dominates accretion luminosity.

To investigate the conversion of the observed core mass function (CMF) to the stellar IMF, we create simulated dust maps and find cores using Clumpfind. We are able to recreate the observed core mass functions, though we find that they depend sensitively on telescope resolution. At resolutions typical of observations of nearby star-forming regions, the CMF and the IMF overlap when outflows are not included (outflows lower the IMF). We are additionally able to recreate the clustering properties of the cores found in ρ Ophiuchus. This implies our simulation of fragmentation is accurate down to at least 2,000 AU, set by the resolution of the observations. When we search the simulation data for bound cores, as opposed to using Clumpfind on 2D datasets, we find two types of bound objects. There are turbulent, bound cores on 20,000 AU scales that each contain a central star or binary with most of the mass. Each of the turbulent cores also contains ~ 10 sub-cores on 1,000 AU scales with a median mass of $0.13 M_{\odot}$. These sub-cores explain the low end of the IMF while the large cores explain the upper end.

Additionally, we find the primary effect of protostellar outflows is to remove 2/3 of the mass that would go into stars. The final mass in stars without outflows is three times the mass in stars with outflows. This creates a core efficiency parameter $\epsilon_{\text{core}} = 1/3$ similar to predictions from Matzner (2002). This should be a warning for simulations that produce the ‘correct’ IMF when outflows are not included (e.g. Bate (2009); Price & Bate (2009)). The outflows do not significantly affect the overall cloud dynamics, as they have small opening

angles and do not couple well to the dense gas in the cores. It is likely magnetic fields would change that conclusion (Wang et al. 2010).

Bibliography

- Agertz, O., Moore, B., Stadel, J., Potter, D., Miniati, F., Read, J., Mayer, L., Gawryszczak, A., Kravtsov, A., Nordlund, Å., Pearce, F., Quilis, V., Rudd, D., Springel, V., Stone, J., Tasker, E., Teyssier, R., Wadsley, J., & Walder, R. 2007, *MNRAS*, 380, 963
- Alves, J., Lombardi, M., & Lada, C. J. 2007, *A&A*, 462, L17
- André, P., Men'shchikov, A., Bontemps, S., Könyves, V., Motte, F., Schneider, N., Didelon, P., Minier, V., Saraceno, P., Ward-Thompson, D., di Francesco, J., White, G., Molinari, S., Testi, L., Abergel, A., Griffin, M., Henning, T., Royer, P., Merín, B., Vavrek, R., Attard, M., Arzoumanian, D., Wilson, C. D., Ade, P., Aussel, H., Baluteau, J.-P., Benedettini, M., Bernard, J.-P., Blommaert, J. A. D. L., Cambrésy, L., Cox, P., di Giorgio, A., Hargrave, P., Hennemann, M., Huang, M., Kirk, J., Krause, O., Launhardt, R., Leeks, S., Le Penneç, J., Li, J. Z., Martin, P. G., Maury, A., Olofsson, G., Omont, A., Peretto, N., Pezzuto, S., Prusti, T., Roussel, H., Russeil, D., Sauvage, M., Sibthorpe, B., Sicilia-Aguilar, A., Spinoglio, L., Waelkens, C., Woodcraft, A., & Zavagno, A. 2010, *A&A*, 518, L102+
- Arce, H. G., Borkin, M. A., Goodman, A. A., Pineda, J. E., & Halle, M. W. 2010, *ApJ*, 715, 1170
- Arce, H. G. & Sargent, A. I. 2006, *ApJ*, 646, 1070
- Arons, J. & Max, C. 1975, *ApJ*, 77
- Ballesteros-Paredes, J., Hartmann, L., & Vázquez-Semadeni, E. 1999, *ApJ*, 527, 285
- Banerjee, R., Klessen, R. S., & Fendt, C. 2007, *ApJ*, 668, 1028
- Banerjee, R., Vázquez-Semadeni, E., Hennebelle, P., & Klessen, R. S. 2009, *MNRAS*, 398, 1082
- Bastian, N., Covey, K. R., & Meyer, M. R. 2010, *ARA&A*, 48, 339
- Basu, S. & Vorobyov, E. I. 2005, in *Protostars and Planets V*, 8116+
- Bate, M. R. 2009, *MNRAS*, 392, 1363
- Bate, M. R. & Bonnell, I. A. 2005, *MNRAS*, 356, 1201
- Beuther, H. & Schilke, P. 2004, *Science*, 303, 1167
- Blitz, L., Fukui, Y., Kawamura, A., Leroy, A., Mizuno, N., & Rosolowsky, E. 2007, *Protostars and Planets V*, 81
- Blitz, L. & Shu, F. H. 1980, *ApJ*, 238, 148
- Blitz, L. & Williams, J. P. 1997, *ApJ*, 488, L145+
- Boldyrev, S., Nordlund, Å., & Padoan, P. 2002, *Physical Review Letters*, 89, 031102
- Bonnell, I. A. & Bate, M. R. 2006, *MNRAS*, 370, 488

- Bonnell, I. A., Bate, M. R., Clarke, C. J., & Pringle, J. E. 1997, *MNRAS*, 285, 201
— . 2001, *MNRAS*, 323, 785
- Bonnell, I. A., Clarke, C. J., & Bate, M. R. 2006, *MNRAS*, 368, 1296
- Bontemps, S., Motte, F., Csengeri, T., & Schneider, N. 2010, *A&A*, 524, A18+
- Brunt, C. M. & Heyer, M. H. 2002, *ApJ*, 566, 276
- Brunt, C. M., Heyer, M. H., & Mac Low, M. 2009, *A&A*, 504, 883
- Canuto, V. M. 1997, *ApJ*, 482, 827
- Carroll, J. J., Frank, A., & Blackman, E. G. 2010, *ApJ*, 722, 145
- Chabrier, G. 2003, *ApJ*, 586, L133
- Chabrier, G. 2005, in *Astrophysics and Space Science Library*, Vol. 327, *The Initial Mass Function 50 Years Later*, ed. E. Corbelli, F. Palla, & H. Zinnecker, 41–+
- Chabrier, G., Baraffe, I., Leconte, J., Gallardo, J., & Barman, T. 2009, in *American Institute of Physics Conference Series*, Vol. 1094, *American Institute of Physics Conference Series*, ed. E. Stempels, 102–111
- Chen, X. & Arce, H. G. 2010, *ApJ*, 720, L169
- Cho, J., Lazarian, A., & Vishniac, E. T. 2002, *ApJ*, 564, 291
- Cunningham, A. J., Frank, A., Quillen, A. C., & Blackman, E. G. 2006, *ApJ*, 653, 416
- Cunningham, A. J., Klein, R. I., F., M. C., & Krumholz, M. R. 2011, submitted
- Downes, T. P. & Cabrit, S. 2007, *A&A*, 471, 873
- Dunham, M. M., Evans, II, N. J., Terebey, S., Dullemond, C. P., & Young, C. H. 2010, *ApJ*, 710, 470
- Elmegreen, B. G., Klessen, R. S., & Wilson, C. D. 2008, *ApJ*, 681, 365
- Elmegreen, B. G. & Scalo, J. 2004, *ARA&A*, 42, 211
- Enoch, M. L., Evans, II, N. J., Sargent, A. I., & Glenn, J. 2009, *ApJ*, 692, 973
- Enoch, M. L., Evans, II, N. J., Sargent, A. I., Glenn, J., Rosolowsky, E., & Myers, P. 2008, *ApJ*, 684, 1240
- Evans, II, N. J., Dunham, M. M., Jørgensen, J. K., Enoch, M. L., Merín, B., van Dishoeck, E. F., Alcalá, J. M., Myers, P. C., Stapelfeldt, K. R., Huard, T. L., Allen, L. E., Harvey, P. M., van Kempen, T., Blake, G. A., Koerner, D. W., Mundy, L. G., Padgett, D. L., & Sargent, A. I. 2009, *ApJS*, 181, 321
- Falceta-Gonçalves, D. & Lazarian, A. 2011, *ApJ*, 735, 99
- Falgarone, E., Pety, J., & Hily-Blant, P. 2009, *A&A*, 507, 355
- Falgarone, E., Pineau Des Forêts, G., Hily-Blant, P., & Schilke, P. 2006, *A&A*, 452, 511
- Falgarone, E., Pineau des Forets, G., & Roueff, E. 1995, *A&A*, 300, 870
- Federrath, C., Klessen, R. S., & Schmidt, W. 2008, *ApJ*, 688, L79
- Federrath, C., Roman-Duval, J., Klessen, R. S., Schmidt, W., & Mac Low, M. 2010, *A&A*, 512, A81+
- Fisher, R. T. 2002, PhD thesis, UNIVERSITY OF CALIFORNIA, BERKELEY
- Fleck, Jr., R. C. 1996, *ApJ*, 458, 739
- Fletcher, A. B. & Stahler, S. W. 1994a, *ApJ*, 435, 313
— . 1994b, *ApJ*, 435, 329
- Frisch, U. & Bec, J. 2001, *New Trends in Turbulence*, 341

- Fukui, Y., Kawamura, A., Wong, T., Murai, M., Iritani, H., Mizuno, N., Mizuno, Y., Onishi, T., Hughes, A., Ott, J., Muller, E., Staveley-Smith, L., & Kim, S. 2009, *ApJ*, 705, 144
- Godard, B., Falgarone, E., & Pineau Des Forêts, G. 2009, *A&A*, 495, 847
- Goldbaum, N. J., Krumholz, M. R., D., M. C., & F., M. C. 2011, submitted
- Goodman, A. A., Rosolowsky, E. W., Borkin, M. A., Foster, J. B., Halle, M., Kauffmann, J., & Pineda, J. E. 2009, *Nature*, 457, 63
- Hansen, C. E., McKee, C. F., & Klein, R. I. 2011, In Press
- Hartmann, L. & Kenyon, S. J. 1996, *ARA&A*, 34, 207
- Hennabelle, P. & Chabrier, G. 2008, *ApJ*, 684, 395
- . 2009, *ApJ*, 702, 1428
- Hennabelle, P., Commerçon, B., Joos, M., Klessen, R. S., Krumholz, M., Tan, J. C., & Teyssier, R. 2011, *A&A*, 528, A72+
- Heyer, M., Gong, H., Ostriker, E., & Brunt, C. 2008, *ApJ*, 680, 420
- Heyer, M. H. & Brunt, C. M. 2004, *ApJ*, 615, L45
- Heyer, M. H. & Schloerb, F. P. 1997, *ApJ*, 475, 173
- Heyer, M. H., Williams, J. P., & Brunt, C. M. 2006, *ApJ*, 643, 956
- Inutsuka, S.-I. & Miyama, S. M. 1992, *ApJ*, 388, 392
- . 1997, *ApJ*, 480, 681
- Johnstone, D., Fich, M., Mitchell, G. F., & Moriarty-Schieven, G. 2001, *ApJ*, 559, 307
- Johnstone, D., Wilson, C. D., Moriarty-Schieven, G., Joncas, G., Smith, G., Gregersen, E., & Fich, M. 2000, *ApJ*, 545, 327
- Kainulainen, J., Beuther, H., Henning, T., & Plume, R. 2009a, *A&A*, 508, L35
- Kainulainen, J., Lada, C. J., Rathborne, J. M., & Alves, J. F. 2009b, *A&A*, 497, 399
- Kaneda, Y., Ishihara, T., Yokokawa, M., Ken'ichi, I., & Atsuya, U. 2003, *Physics of Fluids*, 15, 21
- Kawamura, A., Mizuno, Y., Minamidani, T., Filipović, M. D., Staveley-Smith, L., Kim, S., Mizuno, N., Onishi, T., Mizuno, A., & Fukui, Y. 2009, *ApJS*, 184, 1
- Kenyon, S. J., Hartmann, L. W., Strom, K. M., & Strom, S. E. 1990, *AJ*, 99, 869
- Kirk, H., Pineda, J. E., Johnstone, D., & Goodman, A. 2010, *ApJ*, 723, 457
- Klein, R. I. 1999, *Comput. Appl. Math.*, Vol. 109, No. 1 - 2, p. 123 - 152
- Klein, R. I., Inutsuka, S.-I., Padoan, P., & Tomisaka, K. 2007, *Protostars and Planets V*, 99
- Klessen, R. S. & Hennabelle, P. 2010, *A&A*, 520, A17+
- Kolmogorov, A. 1941, *Akademiia Nauk SSSR Doklady*, 30, 301
- Kritsuk, A. G., Norman, M. L., Padoan, P., & Wagner, R. 2007, *ApJ*, 665, 416
- Kroupa, P. 2002, *Science*, 295, 82
- Krumholz, M., Klein, R. I., & F., M. C. 2011, submitted
- Krumholz, M. R., Klein, R. I., & McKee, C. F. 2007a, *ApJ*, 656, 959
- Krumholz, M. R., Klein, R. I., McKee, C. F., & Bolstad, J. 2007b, *ApJ*, 667, 626
- Krumholz, M. R. & Matzner, C. D. 2009, *ApJ*, 703, 1352
- Krumholz, M. R. & McKee, C. F. 2005, *ApJ*, 630, 250
- Krumholz, M. R., McKee, C. F., & Klein, R. I. 2004, *ApJ*, 611, 399
- . 2005, *Nature*, 438, 332

- Krumholz, M. R., McKee, C. F., & Tumlinson, J. 2009, *ApJ*, 699, 850
- Krumholz, M. R. & Tan, J. C. 2007, *ApJ*, 654, 304
- Lada, C. J., Muench, A. A., Rathborne, J., Alves, J. F., & Lombardi, M. 2008, *ApJ*, 672, 410
- Larson, R. B. 1981, *MNRAS*, 194, 809
- . 1985, *MNRAS*, 214, 379
- . 1995, *MNRAS*, 272, 213
- . 2005, *MNRAS*, 359, 211
- Lemaster, M. N. & Stone, J. M. 2009, *ApJ*, 691, 1092
- Levermore, C. D. & Pomraning, G. C. 1981, *ApJ*, 248, 321
- Li, Z. & Nakamura, F. 2006, *ApJ*, 640, L187
- Lighthill, M. J. 1955, in *IAU Symposium, Vol. 2, Gas Dynamics of Cosmic Clouds*, 121–+
- Low, C. & Lynden-Bell, D. 1976, *MNRAS*, 176, 367
- Mac Low, M. & Klessen, R. S. 2004, *Reviews of Modern Physics*, 76, 125
- Mac Low, M.-M. 1999, *ApJ*, 524, 169
- Mac Low, M.-M., Klessen, R. S., Burkert, A., & Smith, M. D. 1998, *Physical Review Letters*, 80, 2754
- Maron, J. & Goldreich, P. 2001, *ApJ*, 554, 1175
- Masunaga, H. & Inutsuka, S.-i. 2000, *ApJ*, 531, 350
- Masunaga, H., Miyama, S. M., & Inutsuka, S.-I. 1998, *ApJ*, 495, 346
- Matzner, C. D. 2002, *ApJ*, 566, 302
- Matzner, C. D. & McKee, C. F. 1999, *ApJ*, 526, L109
- . 2000, *ApJ*, 545, 364
- McKee, C. F. 1989, *ApJ*, 345, 782
- McKee, C. F. & Offner, S. S. R. 2010, *ApJ*, 716, 167
- McKee, C. F. & Ostriker, E. C. 2007, *ARA&A*, 45, 565
- McKee, C. F. & Tan, J. C. 2003, *ApJ*, 585, 850
- Motte, F., Andre, P., & Neri, R. 1998, *A&A*, 336, 150
- Motte, F., André, P., Ward-Thompson, D., & Bontemps, S. 2001, *A&A*, 372, L41
- Myers, A., Krumholz, M., Klein, R. I., & F., M. C. 2011, in press
- Myers, P. C. 2009, *ApJ*, 700, 1609
- . 2011, ArXiv e-prints
- Nakamura, F. & Li, Z. 2007, *ApJ*, 662, 395
- Norman, C. & Silk, J. 1980, *ApJ*, 238, 158
- Offner, S. S. R., Hansen, C. E., & Krumholz, M. R. 2009a, *ApJ*, 704, L124
- Offner, S. S. R., Klein, R. I., McKee, C. F., & Krumholz, M. R. 2009b, *ApJ*, 703, 131
- Offner, S. S. R., Kratter, K. M., Matzner, C. D., Krumholz, M. R., & Klein, R. I. 2010, *ApJ*, 725, 1485
- Offner, S. S. R., Krumholz, M. R., Klein, R. I., & McKee, C. F. 2008, *AJ*, 136, 404
- Offner, S. S. R. & McKee, C. F. 2011, ArXiv e-prints
- Ossenkopf, V. & Mac Low, M. 2002, *A&A*, 390, 307
- Ostriker, E. C., Gammie, C. F., & Stone, J. M. 1999, *ApJ*, 513, 259

- Padoan, P. & Nordlund, Å. 1999, *ApJ*, 526, 279
— . 2002, *ApJ*, 576, 870
- Padoan, P., Nordlund, Å., Kritsuk, A. G., Norman, M. L., & Li, P. S. 2007, *ApJ*, 661, 972
- Pineda, J. E., Rosolowsky, E. W., & Goodman, A. A. 2009, *ApJ*, 699, L134
- Porter, D., Pouquet, A., & Woodward, P. 2002, *Phys. Rev. E*, 66
- Price, D. J. & Bate, M. R. 2009, *MNRAS*, 398, 33
- Reid, M. A. & Wilson, C. D. 2006, *ApJ*, 650, 970
- Richer, J. S., Shepherd, D. S., Cabrit, S., Bachiller, R., & Churchwell, E. 2000, *Protostars and Planets IV*, 867
- Sadavoy, S. I., Di Francesco, J., Bontemps, S., Megeath, S. T., Rebull, L. M., Allgaier, E., Carey, S., Gutermuth, R., Hora, J., Huard, T., McCabe, C.-E., Muzerolle, J., Noriega-Crespo, A., Padgett, D., & Terebey, S. 2010, *ApJ*, 710, 1247
- Salpeter, E. E. 1955, *ApJ*, 121, 161
- Schnee, S., Enoch, M., Johnstone, D., Culverhouse, T., Leitch, E., Marrone, D. P., & Sargent, A. 2010, *ApJ*, 718, 306
- Semenov, D., Henning, T., Helling, C., Ilgner, M., & Sedlmayr, E. 2003, *A&A*, 410, 611
- Shepherd, D. 2003, in *Astronomical Society of the Pacific Conference Series*, Vol. 287, *Galactic Star Formation Across the Stellar Mass Spectrum*, ed. J. M. De Buizer & N. S. van der Blik, 333–344
- Shestakov, A. I. & Offner, S. S. R. 2008, *J. Chem. Phys.*, 227, 2154
- Shu, F. H. 1977, *ApJ*, 214, 488
- Smith, B. D., Turk, M. J., Sigurdsson, S., O’Shea, B. W., & Norman, M. L. 2009, *ApJ*, 691, 441
- Solomon, P. M., Rivolo, A. R., Barrett, J., & Yahil, A. 1987, *ApJ*, 319, 730
- Stanke, T., Smith, M. D., Gredel, R., & Khanzadyan, T. 2006, *A&A*, 447, 609
- Stone, J. M., Ostriker, E. C., & Gammie, C. F. 1998, *ApJ*, 508, L99
- Swift, J. J. & Welch, W. J. 2008, *ApJS*, 174, 202
- Teixeira, P. S., Zapata, L. A., & Lada, C. J. 2007, *ApJ*, 667, L179
- Testi, L. & Sargent, A. I. 1998, *ApJ*, 508, L91
- Truelove, J. K., Klein, R. I., McKee, C. F., Holliman, II, J. H., Howell, L. H., & Greenough, J. A. 1997, *ApJ*, 489, L179+
- Truelove, J. K., Klein, R. I., McKee, C. F., Holliman, II, J. H., Howell, L. H., Greenough, J. A., & Woods, D. T. 1998, *ApJ*, 495, 821
- Turk, M. J., Smith, B. D., Oishi, J. S., Skory, S., Skillman, S. W., Abel, T., & Norman, M. L. 2011, *ApJS*, 192, 9
- Vazquez-Semadeni, E., Canto, J., & Lizano, S. 1998, *ApJ*, 492, 596
- Vázquez-Semadeni, E., Colín, P., Gómez, G. C., Ballesteros-Paredes, J., & Watson, A. W. 2010, *ApJ*, 715, 1302
- Vázquez-Semadeni, E., Gómez, G. C., Jappsen, A. K., Ballesteros-Paredes, J., González, R. F., & Klessen, R. S. 2007, *ApJ*, 657, 870
- Vestuto, J. G., Ostriker, E. C., & Stone, J. M. 2003, *ApJ*, 590, 858
- Wang, P., Li, Z., Abel, T., & Nakamura, F. 2010, *ApJ*, 709, 27

-
- Whitworth, A., Bate, M. R., Nordlund, Å., Reipurth, B., & Zinnecker, H. 2007, *Protostars and Planets V*, 459
- Williams, J. P., de Geus, E. J., & Blitz, L. 1994, *ApJ*, 428, 693
- Williams, J. P. & McKee, C. F. 1997, *ApJ*, 476, 166
- Wu, C. T., Ferziger, J. H., & Chapman, D. R. 1985, NASA STI/Recon Technical Report N, 86, 30958
- Young, C. H. & Evans, II, N. J. 2005, *ApJ*, 627, 293
- Zinnecker, H. 1982, *Annals of the New York Academy of Sciences*, 395, 226